

Synthesis of zinc oxide nanoparticles by a green process and the investigation of their physical properties

Takalani Nethavhanani



A thesis submitted in partial fulfilment of the requirements for the degree of Magister Scientiae in the Department of Physics, University of the Western Cape

Supervisor: Prof M Maaza, iThemba LABS

Co-supervisor: Prof R Madjoe, University of the Western Cape

June 2017

Keywords

Nanoparticles

Zinc oxide

Synthesis methods

Green chemistry

Natural extract

Aspalathus Linearis

Chelating agent

Bioreduction

Zinc acetate dihydrate

Nano powder

Characterization

Growth mechanism

Thermal properties



Abstract

Synthesis of zinc oxide nanoparticles by a green process and the investigation of their physical properties

T Nethavhanani

Magister Scientiae, Department of Physics, University of the Western Cape.

Zinc oxide (ZnO) is a wide and direct semiconductor with a wurtzite crystal structure. Its multifunctionality as the ideal candidate in applications such as blue-UV light emitting diodes, transparent conducting oxide, selective gas sensor and efficient catalyst support among others, has attracted a significant interest worldwide. Nano-scaled ZnO has been synthesized in a plethora of shapes. A rich variety of physical and chemical methodologies have been used in the synthesis of undoped or doped ZnO. However, such methods either necessitate relatively high vacuum infrastructures, elevated temperatures, or the use of toxic reagents. The “green chemistry” synthesis of metal oxide nanoparticles which is based on using natural plant extract as an effective ‘reducing agent’ of metal precursor, has been reported to be a cleaner and environment-friendly alternative to the physical and chemical methods. The thesis is based on the synthesis and the main physical properties of pure ZnO nanoparticles synthesized by a completely green chemistry process using the natural extract of *Aspalathus Linearis* to bio-reduce the zinc acetate precursor. The obtained ZnO nanopowdered samples were annealed at different temperatures from 300 °C to 600 °C. The samples were characterized using Scanning Electron Microscopy, Energy Dispersive Spectroscopy, Transmission Electron Microscopy, X-ray Diffraction, Differential Scanning Calorimetry, Thermogravimetric Analysis and Fourier Transform Infrared. Highly pure quasi-spherical ZnO nanoparticles with an average crystallite size of 24.6 nm (at 300 °C), 27.2 nm (at 400 °C), 27.6 nm (at 500 °C), and 28.5 nm (at 600 °C) were found. The results also showed that the average crystallite size increased with an increase in annealing temperature. It was successfully demonstrated that the natural plant extract of *Aspalathus Linearis* can be used in the bio-reduction of zinc acetate dihydrate to prepare highly pure ZnO nanoparticles.

February 2017

iii

<http://etd.uwc.ac.za/>

Dedication

I would like to dedicate this work to my lovely parents:

My late father, **Musiiwa Amos Nethavhanani**, my mother **Ntshavheni Esther Nethavhanani** and my aunt **Munzhedzi Elizabeth Negota**.

Thank you for nurturing, supporting, encouraging and constantly praying for me. I sincerely appreciate the countless sacrifices you made to make sure I succeed in life.



Declaration

I declare that “*Synthesis of zinc oxide nanoparticles by a green process and the investigation of their physical properties*” is my own work, that it has not been submitted for any degree or examination in any other university, and that all the sources I have used or quoted have been indicated and acknowledged by complete references.

Takalani Nethavhanani

February 2017

Signature



Acknowledgements

Firstly, I would like to thank my creator, the Almighty God, who has ceaselessly showered me with his divine favour, grace and mercy every day of my life.

This work would not have been possible without the following people and organisations:

I would like to extend my utmost gratitude to my supervisor, Prof Malik Maaza (Materials Research Department, iThemba LABS) for his patience, support and guidance throughout the entire project. I would also like to thank Prof Reginaldt Madjoe (Department of Physics, University of the Western Cape) my co-supervisor, for the assistance and his tireless effort especially with the thesis corrections.

Special thanks to Dr Ntevheleni Thovhogi (Materials Research Department, iThemba LABS) for her assistance with the thesis corrections from the beginning till the end. Thanks to Dr Xolile G. Fuku (Materials Research Department, iThemba LABS) for his assistance with the FTIR measurements and his critical inputs thesis wise. Not forgetting my fellow students, nano-group postdocs and staff of Material Research Department at iThemba LABS for their emotional support and encouragement during the course of this study.

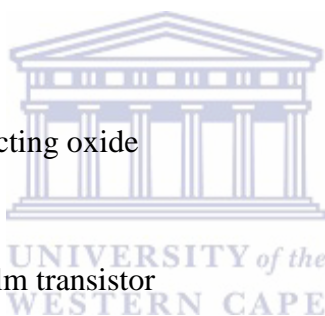
Deep gratitude to the National Research Foundation for the financial assistance throughout the project. My sincere thanks to Mr Paradza Masimba (Physics Department, University of the Western Cape) the Manus/Mastci coordinator for his motivation and always making sure that our needs are met. Mrs Angela Adams (Physics Department, University of the Western Cape) for her amazing administrative help.

I would like to appreciate Dr Remy Bucher and Mr Zakhele Khumalo (Material Research Department, iThemba LABS) assisting me with the XRD measurements, Mr Adrian Josephs and Dr Franscious Cummings (EMU, University of the Western Cape) for their assistance with the SEM and TEM measurements. Not forgetting Prof Salaam Titinchi (Chemical Sciences building, University of the Western Cape) for his provision and assistance with the DSC/TGA instrumentation.

Lastly but by no means least, my amazing siblings: Dr Mpho Magidi (sister), and her husband Musiiwa Peter Magidi, Hulisani Nethavhanani “mam vha Science” (sister), Phumudzo Nethavhanani (brother) and his wife, Thapelo Nethavhanani for the shared tears and laughter, constant support, encouraging words and prayers. And also, my beautiful nieces and nephew: Phathutshedzo, Mukonazwothe, Lufuno, Arehone and Wamashudu for their genuine love and smiles. Thank you all very much.

Abbreviations

ZnO	:	Zinc oxide
Zn(C ₄ H ₆ O ₄)·2H ₂ O	:	Zinc acetate dihydrate
Zn(NO ₃) ₂ ·6H ₂ O	:	Zinc nitrate hexahydrate
HCP	:	Hexagonal close packed
Al ₂ O ₃	:	Aluminium oxide
MgO	:	Magnesium oxide
CeO ₂	:	Cerium oxide
TiO ₂	:	Titanium dioxide
Fe ₂ O ₃	:	Iron oxide
SnO	:	Tin oxide
TCO	:	Transparent conducting oxide
GaN	:	Gallium nitride
TTFT	:	Transparent thin film transistor
SEM	:	Scanning Electron Diffraction
EDS	:	Energy Dispersive Spectroscopy
TEM	:	Transmission Electron Microscopy
XRD	:	X-ray Diffraction
FTIR	:	Fourier Transform Infrared
DSC	:	Differential Scanning Calorimetry
TGA	:	Thermogravimetric Analysis
LEDs	:	Light emitting diodes
Al	:	Aluminium
Ga	:	Gallium
In	:	Indium
Cl	:	Chlorine



I	:	Iodine
Li	:	Lithium
Na	:	Sodium
K	:	Potassium
Cu	:	Copper
Ag	:	Silver
N	:	Nitrogen
P	:	Phosphorus
As	:	Arsenic
PL	:	Photoluminescence
UV	:	Ultraviolet
FE	:	Free exciton
DLE	:	Deep level emission
DMSs	:	Diluted magnetic semiconductors
TM	:	Transition metal
Sc	:	Scandium
V	:	Vanadium
Mn	:	Manganese
Eu	:	Europium
Gd	:	Gadolinium
Er	:	Erbium
O	:	Oxygen
H	:	Hydrogen
PVD	:	Physical vapor deposition
CVD	:	Chemical vapor deposition
RHEED	:	Reflected high energy electron diffraction



Symbols

a / a_0 lattice constant

c / c_0 lattice constant

\AA Angstrom

h Planck constant

ν frequency

E_g bandgap Energy

v_o Oxygen vacancy

v_{zn} Zinc vacancy

O_i Oxygen interstitial

Zn_i Zinc interstitial

α_a in plane thermal coefficient

α_c out of plane thermal coefficient

K Kelvin

$^{\circ}C$ degree Celsius

κ Thermal conductivity

v_s velocity of sound

$c_{lattice}$ lattice specific heat

T_{CH} Characteristic temperature

nm nanometre

μm micrometre

λ wavelength

d spacing between planes

$\frac{dH}{dt}$ Heat flow



T_g	Glass transition
T_c	Crystallization temperature
T_m	Melting temperature
$F(\omega)$	Fourier transform
ω	angular frequency
r	path difference
$f(r)$	interferogram



List of figures

- Figure 2.1** Models showing (i) the rocksalt, (ii) zinc blende, and (iii) wurtzite structures of ZnO.
- Figure 2.2:** Representation of (i) ZnO wurtzite crystal structure, (ii) atomic structure of wurtzite-closed circle, open circle, and thick solid line represent cation, anion, and projection of two bonds, respectively.
- Figure 2.3:** Schematic diagram showing the electronic band structure of a semiconductor.
- Figure 2.4:** A schematic representation of the valence and conduction band curves of energy vs. crystal momentum for a direct and indirect semiconductor. The minimum energy of the indirect band gap has an offset crystal momentum from the valence curve.
- Figure 2.5:** Ball and stick model of the relaxed atomic positions of interstitial hydrogen: (a) at the bond-centre site parallel to the c axis; (b) at the antibonding site perpendicular to the c axis; (c) at the substitutional oxygen site.
- Figure 2.6:** Band diagram illustrating different processes that make up the photoluminescence spectra, excitation relaxation and recombination in k-space.
- Figure 2.7:** A typical PL spectrum of ZnO nanorods with the excitation wavelength of 350 nm.
- Figure 2.8:** Thermal expansion of ZnO in the c-plane and along the c-axis as a function of temperature, also shown is the thermal expansion coefficient of polycrystalline ZnO.
- Figure 2.9:** Thermal conductivity of fully sintered ZnO heated from room temperature to 1000 °C.
- Figure 3.1:** The different synthesis methods for the growing nanoparticles.
- Figure 3.2:** Schematic view of the motion of the ball and the powder mixture.

- Figure 3.3:** Schematic diagram of the thermal evaporation system.
- Figure 3.4:** Schematic diagram of the Sputtering process. Argon is ionized by a strong potential difference. After impact the target atoms are released and travel to the substrate where they form layers of atoms in the thin film.
- Figure 3.5:** Schematic diagram of molecular beam epitaxy showing the evaporation of atoms or molecules from two different sources onto a heated substrate.
- Figure 3.6:** Laser ablation schematic diagram.
- Figure 3.7:** Schematic diagram of a sol-gel process for nanopowders.
- Figure 3.8:** Schematic illustration of the autoclave used in the hydrothermal synthesis.
- Figure 3.9:** Schematic diagram illustrating (i) the setup, (ii) acoustic cavitation effect in the sonochemical synthesis.
- Figure 3.10:** The rotation of a molecule under the influence of the electric field component in an electromagnetic wave.
- Figure 3.11:** Schematic diagram showing the basic concept of the chemical vapor deposition (CVD) method.
- Figure 3.12:** Possible biological entities in the plant extract responsible for the bioreduction of metal ions.
- Figure 3.13:** Mechanism of the nanoparticle formation using the plant extracts.
- Figure 4.1:** The *Aspalathus Linearis* needle-like leaves that were used in the green synthesis of ZnO nanoparticles.
- Figure 4.2:** The (a) dye extracted from the *Aspalathus Linearis*'s leaves, (b) zinc acetate solution, and (c) mixture of the *Aspalathus Linearis* leaves and the zinc acetate solution.
- Figure 4.3:** ZnO powder (a) as-prepared and annealed at (b) 300 °C, (c) 400 °C, (d) 500°C & (e) 600 °C.

- Figure 4.4:** Illustration of the different signals produced during the electron beam-specimen interaction in the SEM microscope and the regions from which the signals can be detected.
- Figure 4.5:** Characteristic x-ray emission by an atom.
- Figure 4.6:** Schematic representation of the components comprising the SEM column.
- Figure 4.7:** General layout of a TEM describing the path of electron beam in a TEM.
- Figure 4.8:** A typical TEM image of spherical ZnO nanoparticles calcined at 700 °C.
- Figure 4.9:** Illustration of a point lattice.
- Figure 4.10:** A primitive cell and the angles between the translational vectors.
- Figure 4.11:** Schematic representation of diffraction of x-rays by a crystal.
- Figure 4.12:** Schematic illustration of (a) an x-ray diffractometer, (b) the arrangement of slits in a diffractometer.
- Figure 4.13:** X-ray diffraction spectrum of ZnO.
- Figure 4.14:** Schematic principle of DSC measurement.
- Figure 4.15:** Typical DSC thermogram labelling four critical points; the glass transition temperature (T_g), the crystallization temperature (T_c), the melting temperature (T_m), and the curing temperature.
- Figure 4.16:** Schematic diagram of TGA.
- Figure 4.17:** Classification of TG curves.
- Figure 4.18:** Schematic representation of an FTIR spectrometer.
- Figure 4.19:** An optical diagram of a Michelson interferometer.
- Figure 4.20:** Representative spectrum in the mid-IR region. The region below 1500 cm^{-1} is defined as the fingerprint region. The region above 1500 cm^{-1} is the functional group region.
- Figure 5.1:** (a) SEM image and (b) the size distribution of the ‘as-prepared’ powder.

Figure 5.2: (a) SEM image and (b) the size distribution of the powder annealed at 300 °C.

Figure 5.3: (a) SEM image and (b) the size distribution of the powder annealed at 400 °C.

Figure 5.4: (a) SEM image and (b) the size distribution of the powder annealed at 500 °C.

Figure 5.5: (a) SEM image and (b) the size distribution of the powder annealed at 600 °C.

Figure 5.6: Variation of the average size of the ZnO nanoparticles with annealing temperature. The line is the corresponding simulation curve.

Figure 5.7: EDX spectra of the ZnO nanoparticles at different temperatures.

Figure 5.8: Variation of the atomic percent of Potassium (K) versus the annealing temperature. The line is the corresponding simulation curve.

Figure 5.9: (a) TEM and (b) SAED of the as-prepared powder.

Figure 5.10: (a) TEM and (b) SAED of the powder annealed at 300 °C.

Figure 5.11: (a) TEM and (b) SAED of the powder annealed at 400 °C.

Figure 5.12: (a) TEM and (b) SAED of the powder annealed at 500 °C.

Figure 5.13: (a) TEM and (b) SAED of the powder annealed at 600 °C.

Figure 5.14: X-ray diffraction spectra of ZnO nanoparticles for different temperatures.

Figure 5.15: TGA-DSC plot of the as-prepared powder sample

Figure 5.16: TGA/DSC plot of the ZnO nanoparticles annealed at 300 °C.

Figure 5.17: TGA/DSC of the ZnO nanoparticles annealed at 400 °C.

Figure 5.18: TGA/DSC plot of the ZnO nanoparticles annealed at 500 °C.

Figure 5.19: TGA/DSC of the ZnO nanoparticles annealed at 600 °C.

Figure 5.20: FTIR spectra of ZnO nanoparticles.

List of tables

- Table 3.1:** Thermal evaporation synthesis conditions and morphology characteristics of ZnO.
- Table 3.2:** Various types of sputtering magnetrons power sources.
- Table 3.3:** The twelve principles of green chemistry which were formulated as guidelines in effort to reduce and/or eliminate environmental pollution.
- Table 3.4:** A selection of biological entities used in the synthesis of nanoparticles.
- Table 3.5:** List of different plants used for synthesis of ZnO nanoparticles.
- Table 4.1:** An overview of the experimental techniques needed for the study of ZnO nanoparticles morphology, structure and properties.
- Table 4.2:** Description of the Bravais lattices and crystal systems.
- Table 5.1:** Description of the powdered samples at different temperature conditions.
- Table 5.2:** Major parameters of the ZnO nanoparticles derived from the XRD analysis.
- Table 5.3:** Enthalpy change calculated for the ZnO powdered samples.

Table of contents

Title	i
Keywords	ii
Abstract	iii
Dedication	iv
Declaration	v
Acknowledgements	vi
Abbreviations	vii
Symbols	ix
List of figures	xi
List of tables'	xv
1. Chapter 1: Introduction	1
1.1 Background	1
1.2 Problem statement	3
1.3 Aims and objective	4
1.4 Thesis layout	5
1.5 References	6
2. Chapter 2: ZnO properties and applications	12
2.1 Crystal structure	12
2.2 Electronic band structure	14
2.3 Electrical properties	16
2.3.1 Defects and doping in ZnO	16
2.3.1.1 n-type dopants	17
2.3.1.2 p-type dopants	17
2.4 Optical properties	18
2.5 Magnetic properties	20



2.6 Thermal properties	20
2.6.1 Thermal expansion coefficients	20
2.6.2 Thermal conductivity	21
2.7 ZnO applications	22
2.8 References	24
3. Chapter 3: Synthesis methods	29
3.1 Physical methods	30
3.1.1 High energy ball milling (HEBM)	31
3.1.2 Physical vapor deposition	32
3.1.2.1 Thermal expansion	32
3.1.2.2 Sputtering	33
3.1.3 Molecular beam epitaxy (MBE)	35
3.1.4 Laser ablation	36
3.2 Chemical methods	38
3.2.1 Sol-gel	38
3.2.2 Hydrothermal/Solvothermal synthesis	39
3.2.3 Sonochemical synthesis	40
3.2.4 Microwave synthesis	42
3.2.5 Chemical vapour deposition	43
3.3 Green chemistry	45
3.4 References	54
4. Chapter 4: Material and characterization techniques	72
4.1 Material preparation	72
4.2 Material characterization	74
4.2.1 Scanning electron microscopy (SEM) and Energy dispersive Spectroscopy (EDS)	75
4.2.1.1 Introduction	75
4.2.1.2 Theory	75
4.2.1.3 Characteristic x-ray emission by an atom and EDS	76
4.2.1.4 Description of technique	77
4.2.1.5 Specimen preparation	78
4.2.2 Transmission electron microscopy (TEM)	79

4.2.2.1 Introduction	79
4.2.2.2 Description of technique	79
4.2.2.3 Sample preparation	80
4.2.3 X-ray diffraction (XRD)	81
4.2.3.1 Introduction	81
4.2.3.2 Geometry of crystals	81
4.2.3.2.1 Miller indices	84
4.2.3.3 Bragg's law for diffraction	84
4.2.3.4 Practical aspect of x-ray diffraction	85
4.2.3.5 Data analysis	87
4.2.4 Differential scanning Calorimetry (DSC)	87
4.2.4.1 Introduction	87
4.2.4.2 Description of technique	88
4.2.4.3 Data analysis	89
4.2.5 Thermogravimetric analysis	90
4.2.5.1 Introduction	90
4.2.5.2 Description of technique	90
4.2.5.3 Data analysis	91
4.2.6 Fourier transform infrared (FTIR)	91
4.2.6.1 Introduction	91
4.2.6.2 Description of technique	92
4.2.6.3 Data analysis	93
4.3 References	95
5. Chapter 5: Results and discussion	98
5.1 Scanning electron microscopy (SEM)	98
5.2 Energy dispersive spectroscopy (EDS)	102
5.3 Transmission electron microscopy (TEM)	104
5.4 X-ray diffraction (XRD)	107
5.5 Differential scanning Calorimetry/ Thermogravimetric analysis (DSC/TGA).....	112
5.6 Fourier Transform Infrared (FTIR)	117
5.7 References	120
6. Chapter 6: Conclusions and recommendations	121

6.1. Conclusion	121
6.2. Future plans and recommendations	122



Chapter 1: Introduction

1.1 Background

Nanotechnology is a relatively recent development in scientific research. The inspiration for the field dates long back to 1959, when Richard P. Feynman, an American physicist at Caltech, lectured, “There is plenty of room at the bottom,” in one of his classes. He suggested that scaling down to nano-level was the key to future technology and advancement [1]. Nanotechnology research henceforth has gained momentum in recent years by providing fundamental and applied research prospects at the nanoscale for various fields which include biomedical, materials science, astronomy and geology, amongst others [2]. Nanoparticles are known to be materials with a diameter of less than 100 nm in size. Unlike their larger counterparts, they have a reduced size associated with high surface/volume ratios that increase as their size decreases [3]. As the particle size decreases to some extent, a large number of constituting atoms is found around the surface of the particles, resulting in highly reactive particles with distinguished physical, optical, chemical and electronic properties. Hence, manipulation and control of the material properties is crucial [4].

Various types of nanoparticles such as metal oxides nanoparticles, polymer nanoparticles and metal nanoparticles have been reported [5]. Metal oxide nanoparticles such as Al_2O_3 , MgO , ZrO_2 , CeO_2 , TiO_2 , ZnO , Fe_2O_3 , SnO ; are the most versatile materials due their diverse properties and functionalities [6]. Amongst these nanoparticles, zinc oxide (ZnO), also known as zincite has attracted much attention within the scientific community as a ‘future material’ and thus an important n-type semiconducting metal oxide [7].

Zinc oxide (ZnO) is characterized by its direct and wide band gap of 3.37 eV at room temperature thus, enabling its use in optoelectronic applications such as light emitting diodes, laser diodes and photodetectors. Most notable, among these properties is its high excitonic binding energy of 60 meV at room temperature which makes it a promising material for optical devices that are based on excitonic effects. Its effective piezoelectric property which is generally used in sensors, transducers and actuators amongst others, has made it one of the most studied oxides in its nano-form in the modern era [8]. Due to its strong luminescence, ZnO has been proved to be a suitable material for phosphor applications [9]. Its high thermal conductivity also makes it useful as an additive in materials and products including plastics, rubbers, cement and ointments. Furthermore, the ZnO radiation hardness is important for optoelectronic applications at high altitudes or even in space [10].

Zinc oxide crystallizes in two main forms: hexagonal wurtzite and cubic zinc blende. The wurtzite structure is mainly used in the thin film industry as a transparent conducting oxide (TCO) [11], while the zinc blende structure can be formed as a metastable phase by means of epitaxial growth on substrate with cubic lattice structures [12]. At ambient conditions, ZnO has a similar wurtzite structure and optical properties as those of its main competitor Gallium nitride (GaN). The big advantage over GaN is its availability of large single crystals and its compliance to wet chemical etching. Other favourable aspects of ZnO include its broad chemistry leading to many opportunities for low power threshold for optical pumping, radiation hardness and biocompatibility. These properties make it an ideal candidate for a variety of devices ranging from sensors through to ultra-violet laser diodes and nanotechnology-based devices such as displays, the design and fabrication of small size devices (i.e., transparent electrodes, window materials for displays and solar cells). The prospect of using ZnO as an alternative to GaN in optoelectronics has driven many research groups worldwide to focus on its semiconductor properties [13, 14].

ZnO probably has the most diverse nanostructures among all other materials, both in structures and properties. Varieties of ZnO nanostructures such as nano-wires [15], nano-belts [16], nano-nails [17], flower-shaped [18], nano-rods [19], whiskers [20], nano-combs [21] and nano-bows [22] have been synthesized in a nano-size controlled manner in view of targeted applications in electronic, photonic and spintronic devices. These nanostructures have potential applications in fabricating functional advanced Nano electronic devices since the behaviour of materials depends also on the crystal morphologies [23]. Nano-rods and nanowires have recently attracted considerable attention towards scientific community because of their novel properties and potential technological applications. They are widely used in the field of catalysis, gas sensor, solar cell materials, antimicrobial materials and optoelectronic devices [24]. The ZnO nano-belts are being used as nano-sensors, nano-cantilevers, field effect transistors and nano-resonators [25]

A rich variety of physical (vapor-phase process) and chemical (solution phase) methodologies have been used to synthesize undoped and doped ZnO. The vapor phase process includes molecular beam epitaxy (MBE) [26], metal-organic chemical vapor deposition (MOCVD) [27], sputtering method [28], pulsed laser deposition (PLD) [29], thermal decomposition [30], and thermal evaporation and condensation [31] which is favoured for the high quality of the ZnO final product. However, the physical method in general requires a non-cost-effective vacuum based infrastructure whilst limited in terms of

large-scale production. For the past years, the solution phase methods have been popularly adopted to synthesize ZnO nanoparticles due to the low cost, superior uniformity and high yield of nanoparticles [32]. Hitherto hydrothermal decomposition [33], solvothermal decomposition [34], liquid ultra-sonication [35], free surfactant microwave [36], solid state chemistry [37], solution plasma [38], electrochemical reaction [39], and sol gel process [40] have been employed to synthesize nano-scaled ZnO. The chemical method has the disadvantage of using organic solvents as reducing agents, which can be toxic as well as not easy in treatment of the waste end product [41].

There is an obvious need to develop alternative nanoparticle synthesis methods which are cost-effective and at the same time eliminate the use of toxic reagents in their synthesis procedures. Thus, the “green nano-synthesis” methods are more favourable than the chemical and physical methods of synthesis because of their eco-friendliness and compatibility for pharmaceutical and other biomedical applications [42]. The green process approach uses various microorganisms, enzymes, part of plants and plant extracts as reducing agents during synthesis. Hence, hazardous wastes are kept out of the environment in the first place rather than cleaning them up once they have been formed [43].

A large number of reports have been dedicated to greener synthesis of zinc oxide nanoparticles [44 - 49]. Extracts from brown marine *Sargassum Myriocystum* sea weeds, *Abus Precatorius* seeds, *Calotropis Gigantea* leaves, *Camellia Sinensis* leaves, *Azadirachta Indica* leaves, *Ocimum Tenuiflorum* leaves, *Calotropis Procera* milky latex, *Agathosma Betulina*, etc. have been reported to produce highly stable ZnO nanoparticles of different sizes ranging from 13 - 500 nm and shapes including spherical, hexagonal, rectangle, radical and triangle.

1.2 Problem statement

Over the years ZnO nanoparticles have gained global interest, because of their interesting properties such as a wide and direct band gap, high thermal stability, large exciton binding energy, strong luminescence. Thus, making ZnO nanoparticles suitable to be used as an additive in numerous materials and products such as rubbers, paints, ointments, adhesives, batteries, and sealants [50].

Despite the progress, the ongoing interest of ZnO nanoparticles in the emerging applications for transparent electrodes, transparent thin film transistors (TTFT) chemical sensors, laser diodes, light emitting diodes (LEDs), water purification, solar cell, gas sensors and transparent electrode technologies, has raised major challenges that are still in need of further investigation. Such challenges include controlling the electrical conductivity of ZnO, achieving reproducible p-type ZnO, and the cause of the unintentional n-type conductivity that is observed in as-grown ZnO thin films.

Currently, investigations on the ‘green’ synthesis method of ZnO nanoparticles are being studied as an alternative to the chemical and physical methods which are non-compatible, toxic and costly. Unlike these methods, the ‘green’ synthesis method is a compatible, eco-friendlier and cheaper approach.

1.3 Aims and objectives

The aim of this research work is to make a literature survey on ZnO nanoparticles and their properties using the “green chemistry” synthesis approach. More specifically, the focus will mainly be on using the *Aspalathus Linearis*'s natural extract as a reducing agent in the ZnO synthesis. The annealing temperature has been reported to contribute to the fabrication of the ZnO nanoparticles, the shape of the crystalline grain, the life-time of the charge carriers and the conduction type of the material; therefore it is an essential task to be investigated.

The main objectives of the study are:

- To synthesize high quality zinc oxide (ZnO) nanoparticles by an entirely green chemistry process using the *Aspalathus Linearis*'s extract as an effective chemical reduction agent without addition of any acidic or basic standard medium
- To report on the effect of the annealing temperature on the stability, structural, electrical and optical properties of the synthesized nano-scaled ZnO nanoparticles by using characterization techniques such as the Scanning Electron Microscopy (SEM), Energy Dispersive X-ray Spectroscopy (EDS), Transmission Electron Microscopy (TEM), X-ray Diffraction (XRD), Fourier Transform Infrared spectroscopy (FTIR), as well as Differential Scanning Calorimetry (DSC) and Thermogravimetric Analysis (TGA) characterizing techniques.

1.4 Thesis layout

Chapter 1: provides a brief background on the study as well as a motivation for the present study.

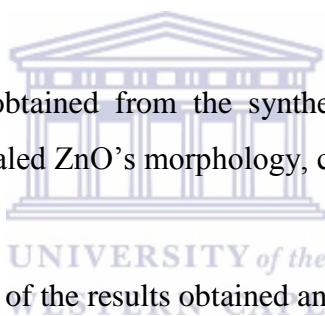
Chapter 2: highlights the basic properties of ZnO such as its crystal structure, encompassing lattice parameters, electronic band structure, electrical properties, magnetic properties, optical properties and thermal properties. This chapter also provides an overview of the various applications of the ZnO nanoparticles.

Chapter 3: provides an overview of the various synthesis methods for obtaining ZnO nanoparticles.

Chapter 4: provides description of the methods and materials used in the course of the study, as well as an overview of the characterization techniques employed to analyse the zinc oxide nanoparticles.

Chapter 5: covers the results obtained from the synthesis of the ZnO nanoparticles. It provides in particular the nano-scaled ZnO's morphology, chemical composition, crystallinity as well as thermal properties.

Chapter 6: presents the summary of the results obtained and the future work.



1.5 References

- [1] T. Appenzeller, "The man who dared to think small," *Science*, vol. 254, no. 5036, pp. 1300-1301, 1991.
- [2] AzoNano, "Zinc Oxide (ZnO) Nanoparticles – Properties, Applications," [Online]. Available: <http://www.azonano.com/article.aspx?ArticleID=3348>. [Accessed 03 November 2015].
- [3] ScienceDaily, "Nanoparticle," [Online]. Available: <https://www.sciencedaily.com/terms/nanoparticle.htm>. [Accessed 28 October 2016].
- [4] L. Vayssieres, "On the design of advance metal oxide nanomaterials," *International Journal of Nanotechnology*, vol. 1, no. 1, pp. 1-41, 2004.
- [5] V. Mody, "Introduction to metallic nanoparticles," *Journal of Pharmacy & BioAllied Sciences*, vol. 2, no. 4, pp. 282-289, 2010.
- [6] M. Fernández-Garcia and J. Rodriguez, "Metal Oxide Nanoparticles. Manuscript submitted for publishing," *Nanomaterials: Inorganic and Bioinorganic Perspectives*, 2007.
- [7] V. Coleman and C. Jagadish, "Basic Properties and Applications of ZnO," in *Zinc Oxide Bulk, Thin Films and Nanostructures: Processing, Properties and Application*, C. Jagadish and S. Pearton, Eds., Amsterdam, Elsevier, 2006, pp. 1-20.
- [8] W. Mai, "Synthesis, Characterization and Application of ZnO Nanomaterials," Atlanta, 2009.
- [9] A. Janotti and C. Van de Walle, "Fundamentals of zinc oxide as a semiconductor," *Reports on progress in Physics*, vol. 72, no. 12, pp. 1-2, 2009.
- [10] R. Panwar, "Preparation of modified ZnO nanoparticles by sol-gel process and their characterization," Punjab, 2009.
- [11] S. Vijayalakshmi, "Investigations on ZnO:M (M=Al, Cd), SnO₂:Zn and Zn₂SnO₄ thin films deposited by spray pyrolysis method," Chennai, 2009.

- [12] Z. Xin-Yu, C. Zhou-Wen, Q. Yan-Peng, F. Yan, Z. Liang, Q. Li, M. Ming-Zhen, Ri-Ping, L and W. Wen-Kui, "Ab Initio Comparative Study of Zincblende and Wurtzite ZnO," *Chinese Physics Letters*, vol. 24, no. 4, pp. 1032-1034, 2007.
- [13] H. Morkoç and Ü. Özgür, "General properties of ZnO," in *Zinc Oxide: Fundamentals, Materials and Device Technology*, Weinheim, Wiley-VCH, pp. 1-70, 2007.
- [14] V. Coleman and C. Jagadish, "Basic Properties and Applications of ZnO," in *Zinc Oxide Bulk, Thin Films and Nanostructures: Processing, Properties and Applications*, Amsterdam, Elsevier, pp. 1-20, 2006.
- [15] J. Wu, Y. Chen and W. Kao, "Ultrafine ZnO Nanoparticles/Nanowires Synthesized on a Flexible and Transparent Substrate: Formation, Water Molecules, and Surface Defect Effects," *ACS*, vol. 6, no. 1, pp. 487-494, 2013.
- [16] S. Sandhu, "ZnO Nanobelts: An Efficient Catalyst for Synthesis of 5-Arylidine-2,4-Thiazolidinediones and 5-Arylidine-Rhodanines," *International Journal of Organic Chemistry*, vol. 2, no. 3A, pp. 305-310, 2012.
- [17] J. Lao, J. Huang, D. Wang and Z. Ren, "ZnO Nanobridges and Nanonails," *Nano Letters*, vol. 3, no. 2, pp. 235-238, 2003.
- [18] M. Khan, M. Hameedullah, A. Ansari, M. Ahmad, M. Lohani, R. Khan, M. Alam, W. Khan, F. Husain and I. Ahmad, "Flower-shaped ZnO nanoparticles synthesized by a novel approach at near-room temperatures with antibacterial and antifungal properties," *International Journal of Nanomedicine*, vol. 9, no. 1, pp. 853-864, 2014.
- [19] P. Giri, S. Bhattacharyya, B. Chetia, S. Kumari, D. Singh and P. Iyer, "High-Yield Chemical Synthesis of Hexagonal ZnO Nanoparticles and Nanorods with Excellent Optical Properties," *Journal of Nanoscience and Nanotechnology*, vol. 12, no. 1, pp. 201-206, 2012.
- [20] L. Zhang, L. Yang, J. Wang and L. Xiang, "Synthesis of ZnO whiskers via EDTA-assisted hydrothermal routes," *International Journal of Nanotechnology*, vol. 10, no. 1, pp. 38-47, 2013.

- [21] X. Xu, M. Wu, M. Asoro, P. Ferreira and D. Fan, "One-Step Hydrothermal Synthesis of Comb-Like ZnO Nanostructures," *American Chemical Society*, vol. 12, no. 10, pp. 4829-4833, 2012.
- [22] X. Yu, H. Ji, H. Wang, J. Sun, Du and X, "Synthesis and Sensing Properties of ZnO/ZnS Nanocages," *Nanoscale Research Letters*, vol. 5, no. 644, pp. 644-648, 2010.
- [23] R. Rusdi, A. Rahman, N. Mohamed, N. Kamarudin and N. Kamarulzaman, "Preparation and band gap energies of ZnO nanotubes, nanorods and spherical nanostructures," *Powder Technology*, vol. 210, no. 1, pp. 18-22, 2011.
- [24] C. Bhakat and P. Singh, "Zinc Oxide Nanorods: Synthesis and Its Applications in Solar Cell," *International Journal of Modern Engineering Research*, vol. 2, no. 4, pp. 2452-2454, 2012.
- [25] Z. Wang, "Zinc oxide nanostructures: growth, properties and applications," *Journal of Physics: Condensed Matter*, vol. 16, no. 25, pp. R829-R858, 2004.
- [26] J. Arthur, "Molecular beam epitaxy," *Surface Science*, vol. 500, no. 1, pp. 189-217, 2002.
- [27] A. Jones and M. Hitchman, "Overview of Chemical Vapour Deposition," in *Chemical Vapour Deposition: Precursors, Processes and Applications*, A. Jones and M. Hitchman, Eds., Cambridge, Royal Society of Chemistry, pp. 1-36, 2009.
- [28] J. Dong, C. Zhen, H. Hao, J. Xing, Z. Zhang, Z. Zheng and X. Zhang, "Controllable synthesis of ZnO nanostructures on the Si substrate by a hydrothermal route," *Nanoscale Research Letters*, vol. 8, no. 378, pp. 1-7, 2013.
- [29] J. Zhao, X. Li, J. Bian and W. Yu, "Structural, Optical and Electrical Properties of ZnO Films Grown by Pulsed Laser Deposition (PLD)," *Research Gate*, vol. 276, no. 3, pp. 507-512, 2005.
- [30] C. Lin and Y. Li, "Synthesis of ZnO nanowires by thermal decomposition of zinc acetate dihydrate," *Materials Chemistry and Physics*, vol. 113, no. 1, p. 334-337, 2009.

- [31] M. Vaghayenegar, A. Kermanpur and M. Abbasi, "Formation mechanism of ZnO nanorods produced by the electromagnetic levitational gas condensation method," *Scientia Iranica*, vol. 18, no. 6, pp. 1647-1651, 2011.
- [32] J. Soni and A. Koser, "Synthesis of ZnO nanoparticle using different concentration of Capping Agent," *International Journal of Technology Innovations and Research*, vol. 16, no. 1, pp. 1-7, 2014.
- [33] W. Shi, G. Gao and L. Xiang, "Synthesis of ZnO whiskers via hydrothermal decomposition route," *Transactions of Nonferrous Metals Society of China*, vol. 20, no. 6, pp. 1049-1052, 2010.
- [34] D. Yiamsawas, K. Boonpavanitchakul and W. Kangwansupamonkon, "Preparation of ZnO Nanostructures by Solvothermal Method," *Journal of Microscopy Society of Thailand*, vol. 23, no. 1, pp. 75-78, 2009.
- [35] S. Chung, J. Leonard, I. Nettleship, J. Lee, Y. Soong, D. Martello and M. Chyu, "Characterization of ZnO nanoparticle suspension in water: Effectiveness of ultrasonic dispersion," *ResearchGate*, vol. 194, no. 1, pp. 75-80., 2009.
- [36] D. Sharma, S. Sharma, B. Kaith, J. Rajput and M. Kaur, "Synthesis of ZnO nanoparticles using surfactant free in-air and microwave method," *Applied Surface Science*, vol. 257, no. 22, p. 9661–9672, 2011.
- [37] A. Noroozi, M. Sadeghi, A. Tehrani, P. Sarabadani, S. Rajabaifar and M. Mirzaee, "Synthesis and Characterization of Zinc Oxide Nano-particles by Solid State Chemical Reaction Method," *Springer Link*, vol. 24, no. 3, pp. 757-770, 2013.
- [38] G. Saito, S. Hosokai and T. Akiyama, "Synthesis of ZnO nanoflowers by solution plasma," *Science Direct*, vol. 130, no. 1, p. 79–83, 2011.
- [39] M. Stariwicz and B. Stypula, "Electrochemical Synthesis of ZnO Nanoparticles," *Research Gate*, vol. 2008, no. 6, pp. 869 - 872, 2007.
- [40] R. Alwan, Q. Kadhim, K. Sahan, R. Ali, R. Mahdi, N. Kassim and A. Jassim, "Synthesis of Zinc Oxide Nanoparticles via Sol – Gel Route and Their Characterization," *Scientific*

and Academic Publishing, vol. 5, no. 1, pp. 1-6, 2015.

- [41] A. Diallo, B. Ngom, E. Park and M. Maaza, "Green synthesis of ZnO nanoparticles by *Aspalathus linearis*: Structural and optical properties," *Journal of Alloys and Compounds*, vol. 646, no. 1, pp. 425-430, 2015.
- [42] S. Azizi, M. Ahmad, F. Namvar and R. Mohamad, "Green biosynthesis and characterization of zinc oxide nanoparticles using brownmarinemacroalga *Sargassum muticum* aqueousextract," *Materials Letters*, vol. 116, no. 1, pp. 275-277, 2013.
- [43] U. Pattanayak, "Green synthesis of Zinc nanoparticle by microbes," Orissa, 2013.
- [44] S. Nagarajan and K. Kuppusamy, "Extracellular synthesis of zinc oxide nanoparticle using seaweeds of gulf of Mannar, India," *Journal of Nanobiotechnology*, vol. 11, no. 39, pp. 1-11, 2013.
- [45] C. Vidya, S. Hiremath, M. Chandraprabha and M. Antonyraj, "Green synthesis of ZnO nanoparticles by *Calotropis Gigantea*," in *Nat. Conf. on Women in Science & Engineering*, Dharwad, 2013.
- [46] A. Oudhia, P. Kulkarni and S. Sharma, "Green synthesis of ZnO nanotubes for bioapplications," in *Nat. Conf. on Nanostructured Materials and their Characterization*, Chhattisgarh, 2015.
- [47] S. Raut, T. P.V and R. Thakre, "Green Synthesis of Zinc Oxide (ZnO) Nanoparticles Using *Ocimum Tenuiflorum* Leaves," *International Journal of Science and Research (IJSR)*, vol. 4, no. 5, pp. 1225-1228, 2015.
- [48] S. Sabir, M. Arshad and S. Chaudhari, "Zinc Oxide Nanoparticles for Revolutionizing Agriculture: Synthesis and Applications," *The Scientific World Journal*, vol. 2014, no. 2014, pp. 1-8, 2014.
- [49] S. Senthilkumar and T. Sivakumar, "Green tea (*Camellia sinensis*) mediated synthesis of Zinc Oxide (ZnO) nanoparticles and studies on their antimicrobial activities," *International Journal of Pharmacy and Pharmaceutical Sciences*, vol. 6, no. 6, pp. 461-465, 2014.

- [50] "Zinc Oxide Applications," [Online]. Available: <http://www.zinc.org.in/zinc-oxide-applications/>. [Accessed 05 November 2015].



Chapter 2: ZnO Properties and Applications

In this chapter, the basic properties of ZnO such as its crystal structure, lattice parameters, electronic band structure, electrical properties, optical properties, magnetic properties and thermal properties will be discussed. Furthermore, the chapter will give an overview of the ZnO's principal applications.

2.1 Crystal structure

ZnO is a group II –VI binary compound semiconductor which usually crystallizes in either three forms: hexagonal wurtzite, cubic zincblende, and cubic rocksalt (or Rochelle salt) as schematically shown in Figure 2.1. The zinc blended ZnO symmetry can be stabilized only by growth on cubic substrates whereas the rocksalt or Rochelle salt may be observed at relatively high pressures [1]. The crystal structure of ZnO at the nanoscale is wurtzite and hence is the most common form at ambient conditions. It is non-centrosymmetric (has no inversion symmetry), and due to this, the ZnO crystals have piezoelectricity and pyroelectricity properties [2].

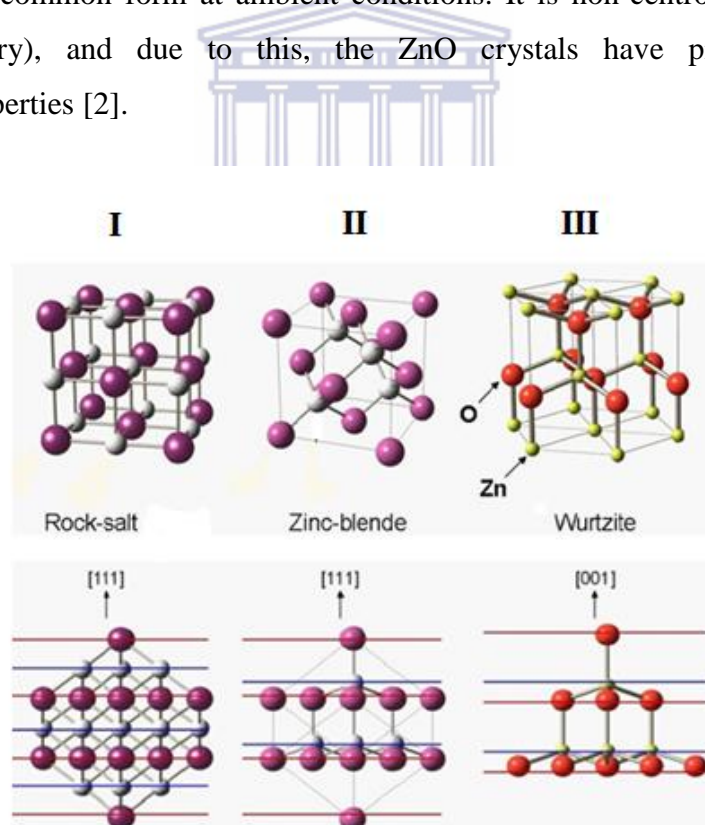


Figure 2.1: Models showing (i) the rocksalt, (ii) zinc blende, and (iii) wurtzite crystal structures of ZnO [3].

The ZnO wurtzite structure has a hexagonal unit cell with two lattice parameters $a = 0.329$ nm and $c = 0.520$ nm in the ratio of $c/a = 1.633$. The ZnO wurtzite structure belongs to the

space group C_{6v}^4 in the Schoenflies notation and $P63mc$ in the Hermann-Mauguin notation [4]. Figure 2.2 clearly shows the structure composed of two interpenetrating hexagonal close packed (hcp) sublattices, (where O^{2-} and Zn^{2+} ions are tetrahedrally-coordinated with each other). Each sublattice consists of one type of atom (Zn or O) displaced with respect to each other along the threefold c-axis by the amount of $u = 3/8 = 0.375$ (in an ideal wurtzite structure) in fractional coordinates [1, 5]. Also, each sublattice includes four atoms per unit cell, and every group II atom is surrounded by four atoms of the group VI atom, or vice versa. The oppositely charged ions produce positively charged Zn-(0001) and negatively charged O-(000-1) surfaces resulting in a normal dipole moment and spontaneous polarization along the c-axis as well as a divergence in surface energy. Many ZnO properties such as growth, etching, defect generation and plasticity, spontaneous polarization and piezoelectricity depend on its polarity [6].

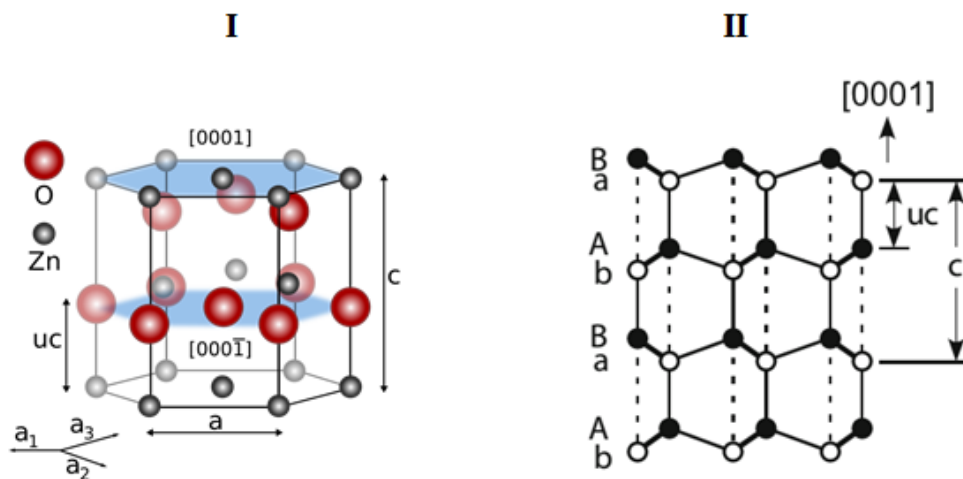


Figure 2.2: Representation of (i) ZnO wurtzite crystal structure, (ii) atomic structure of wurtzite-closed circle, open circle, and thick solid line represent cation, anion, and projection of two bonds, respectively [7].

The pairs of cation and anion atoms in the wurtzite structure (connected by dashed lines along the $[0001]$ direction in Figure 2.2 (ii)) are attracted to each other by electrostatic force. It is considered that these electrostatic interactions make the wurtzite-ZnO to be more stable than the zincblende-ZnO. Besides the (0001) polar plane which is associated with the direction $\langle 0001 \rangle$ commonly used for growth, many other ZnO secondary planes and directions exist in the crystal structures [8].

2.2 Electronic band structure

ZnO exhibits a wide band gap of approximately 3.3 eV at room temperature [9]. Electronic band structure describes the range of energies that an electron within the solid may have (called energy bands) and ranges of energy that it may not have (called band gaps). Figure 2.3 shows a simplified energy band diagram used to describe semiconductors. The band gap represents the minimum energy difference between the top of the valence band (full state) and the bottom of the conduction band (empty state). Since for ZnO the valence band and the conduction band edges occur at the same value of the electron momentum as shown in Figure 2.4, the material is called a direct band gap semiconductor [10, 11].

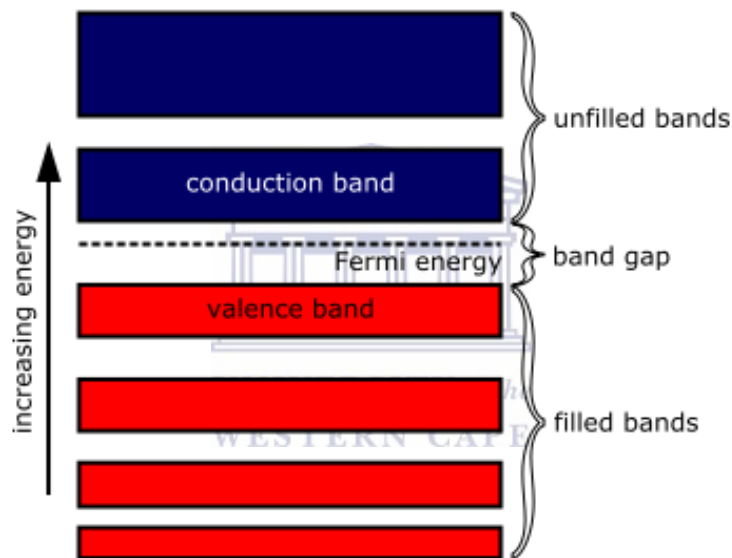


Figure 2.3: Schematic diagram showing the electronic band structure of a semiconductor [12].

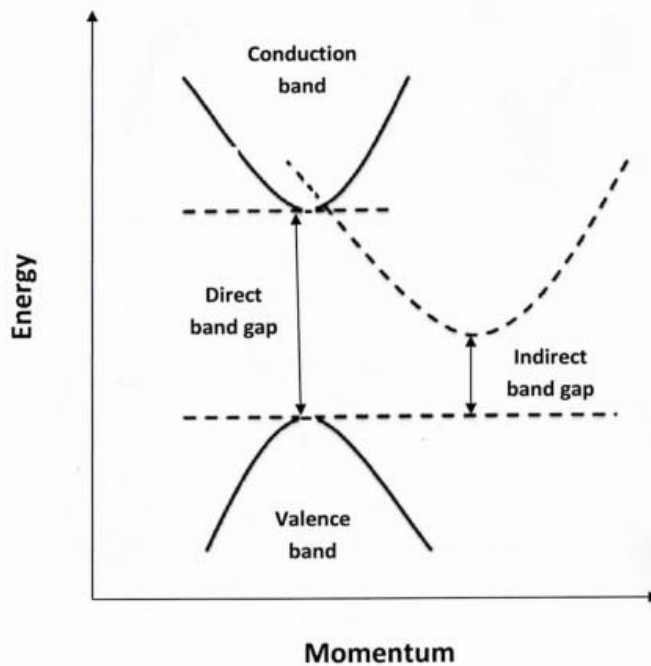


Figure 2.4: A schematic representation of the valence and conduction band curves of energy vs. crystal momentum for a direct and indirect semiconductor. The minimum energy of the indirect band gap has an offset crystal momentum from the valence curve [13].

Incident photons excite electrons from the valence band to the conduction band given that the energy of the photon exceeds that of the band gap of the semiconducting material. When these electrons fall from the conduction band to the valence band, they emit the electronic transition energy into the range of visible light. This creates an electron-hole pair (hole in the valence band, electron in the conduction band) that may move freely, thus generating electricity as a result of moving charges [14]. Hence, light emitting devices such as light-emitting diodes (LEDs) and semiconductor lasers that emit in the visible spectrum, or even produce ultraviolet emission are made. Wide band gap semiconductors are a useful property in high-power applications that require large electric fields. A higher energy gap gives devices the ability to operate at higher temperatures, and for power switching applications [15, 16].

2.3 Electrical properties

ZnO mostly exists as an n-type semiconductor, whose frequently observed unintentional n-type conductivity was supposedly believed to be due to the existence of native point defects attributed to the oxygen vacancies and Zn interstitial ions which act as donors in the ZnO lattice [17]. Recent studies indicate that oxygen vacancies are actually deep rather than shallow donors and cannot cause the observed n-type conductivity [18]. The cause would be related to the unintentional incorporation of donor impurities that act as shallow donors, with hydrogen being a likely candidate. It has been confirmed that both the interstitial and substitutional hydrogen act as shallow donors in ZnO [19]. The interstitial hydrogen forms a strong bond with O in ZnO, and acts as a shallow donor contrary to its amphoteric behaviour in controversial semiconductors and diffuses easily. Interstitial hydrogen prefers sites where it can strongly bind to an oxygen atom, forming an O-H bond length of 0.99 - 1.01 Å, as shown in Figure 2.5(a) and (b). On the other hand, the substitutional hydrogen on an oxygen site (shown in Figure 2.5(c)) diffuses easily and can alternatively be regarded as a complex consisting of hydrogen and an oxygen vacancy [20, 21].

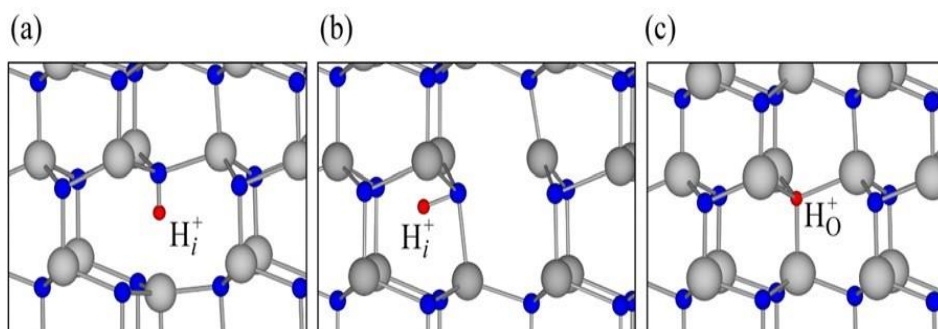


Figure 2.5: Ball and stick model of the relaxed atomic positions of interstitial hydrogen: (a) at the bond-centre site parallel to the c axis; (b) at the antibonding site perpendicular to the c axis; (c) at the substitutional oxygen site [22].

2.3.1 Defects and doping in ZnO

Controlling the electrical conductivity of oxide nanostructures is an important step toward their application in electronics and optoelectronics - for fabrication of high performance solar cells and ultraviolet detectors. In order to achieve the potential offered by ZnO, both high

quality n-type and p-type are necessary [2, 19]. Great progress has been made in the control and understanding of n-type doping and conductivity of ZnO yet reliable p-type doping of ZnO still remains difficult. Controlling the n-type conductivity is a necessary step toward achieving p-type conductivity in ZnO. The energy positions and concentrations of shallow and deep donors have been identified and are being used as the basis to explore p-type conductivity [19, 23].

2.3.1.1 n-type dopants

Excess zinc is always found in ZnO (this is due to its wurzite structure), as a result, ZnO is a non-stoichiometric compound and an n-type semiconductor. As previously discussed, the n-type conductivity of unintentionally doped ZnO has been proven to be due to hydrogen, which is valid since hydrogen is always present in all growth methods and easily diffuse into ZnO in large amounts due to its large mobility. Group III elements (Al, Ga, In) as substitutional elements for Zn and group VII elements (Cl and I) as substitutional elements for oxygen, used as dopants have resulted in highly conductive ZnO films [2, 24 - 29].

2.3.1.2 p-type dopants

ZnO is easily n-type doped but when it comes to p-type doping, there is still some difficulty. The candidates for acceptor impurities include group I elements: Li, Na, K, Cu and Ag and group V elements N, P and As. However many of these form deep acceptors and do not result in p-type conduction at room temperature. Lyons et al. reports on how N, which has been regarded as the most promising p-type dopant in ZnO, has recently been shown to act as a deep acceptor with an ionization of 1.3 eV [24]. Many reports on p-type ZnO have appeared in literature [30 - 32], however their reliability and reproducibility are still questionable. Current limitations to p-doping do not limit electronic and optoelectronic applications of ZnO, which usually require junctions of n-type and p-type material. Announcements about p-type ZnO have been made; hence this material could be potentially important for tunnel-junction interconnects in tandem-junction solar cells as well as for optically transparent transistors [33].

2.4 Optical properties

Optical transitions in ZnO have been studied by a variety of experimental techniques including optical absorption, reflection, photoluminescence, transmission, cathodoluminescence, etc. [34]. At room temperature the photoluminescence (PL) spectrum of ZnO typically consists of a UV emission band and a broad emission band. Luminescence is light emission by any process other than heating. Luminescence in semiconductors is the direct result of electron transitions from higher to lower energy levels. Figure 2.6 shows a simplified band structure of a semiconductor near the centre of the first Brillouin zone where a material with band gap energy E_g is irradiated by light or heat with energy $h\nu > E_g$, resulting in the excitation of an electron. The electron and hole thermalize to the lowest energy state of their respective bands via photon emission. Before recombining across the fundamental band gap or defect levels within the band gap, they emit photons of the corresponding energies [35].

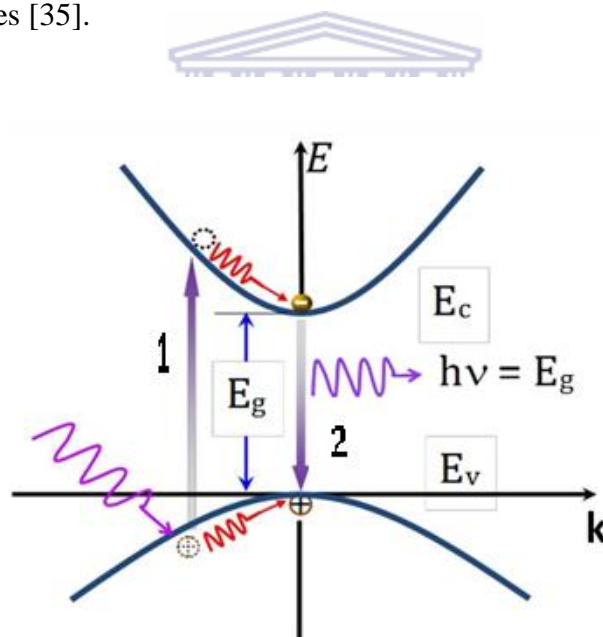


Figure 2.6: Band diagram illustrating different processes that make up the photoluminescence spectra, excitation relaxation and recombination in k -space [35].

The optical properties of a semiconductor are associated with both intrinsic and extrinsic effects. Intrinsic effects take place between the electrons in the conduction band and the holes in the valence band, including excitonic effects caused by the Coulomb interaction. Extrinsic effects are related to dopants/ impurities or point defects and complexes, which usually create electronic states in the band gap and therefore influence both optical absorption and emission

processes. Both intrinsic and extrinsic processes can effectively studied by analysing the PL (photoluminescence) spectra. At room temperature the PL spectrum from ZnO typically consists of a UV emission band and a broad emission band as shown in Figure 2.7. The UV emission band is dominated by free exciton (FE) emission related to a near band-edge transition of ZnO, namely the recombination of the free excitons and is associated with intrinsic effects.. The broad emission band between 420 - 700 nm, is observed in all small samples regardless of the growth conditions called Deep Level Emission (DLE) band. This band has previously been attributed to several defects in the crystal such as O-vacancy (V_O), Zn-vacancy (V_{Zn}), Oxygen-interstitial (O_i), Zn-interstitial (Zn_i) and substitutional Cu. Recently, this deep level emission band has been identified to be contributed by two different defect origins: V_O and V_{Zn} [34, 35].

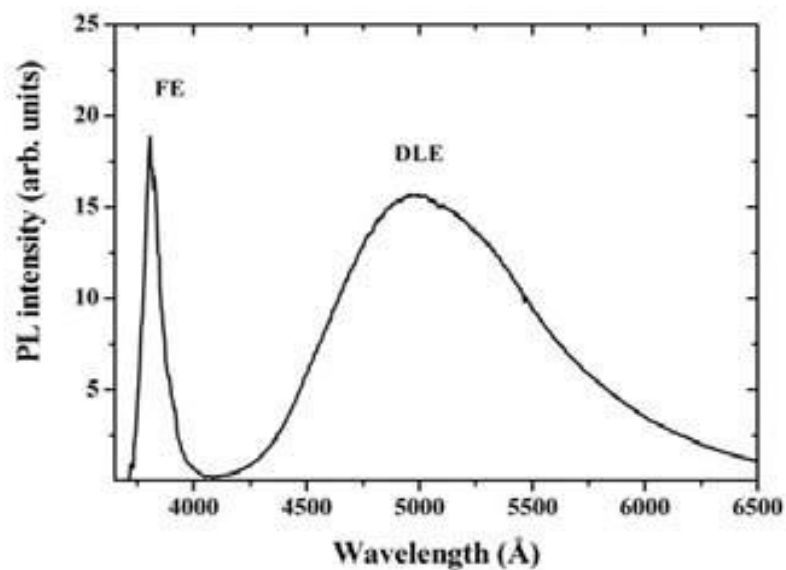


Figure 2.7: A typical PL spectrum of ZnO nanorods with the excitation wavelength of 350 nm [34].

ZnO's large exciton binding energy (~ 60 meV) paves the way for the intense near-band-edge excitonic emission at room and higher temperatures. As a result, laser operation based excitonic transitions are expected.

2.5 Magnetic properties

Diluted magnetic semiconductors (DMSs) are nonmagnetic semiconductors in which a small fraction of host cations are replaced by transition metal or rare-earth ions, with both spin and charge degrees of freedom in a single material. The group III–V and II–VI diluted magnetic semiconductors have attracted much interest in recent years and have been under intense research. This is due to their potential applications in spin-based multifunctional electronic devices such as ultraviolet absorbers, optoelectronics, gas sensors, non-volatile memory devices, and quantum computer. Of all the oxide diluted magnetic semiconductors, the transition metal (TM) doped ZnO has been identified as a promising one, because the host material ZnO, is a chemically and thermally stable type II–VI compound semiconductor. ZnO, like GaN, has been predicted to retain its ferromagnetism at room temperature in contrast to other DMSs such as GaAs and ZnTe [36]. Generally, 3d transition-metal ions (such as Sc, Ti, V, Mn etc.) and rare earth elements (e.g. Eu, Gd, Er, etc.) have partially filled f states which are substituted for the cations of the host semiconductors. Even in the absence of transition metal doping, pure ZnO and TiO₂ nanoparticles show ferromagnetism above room temperature due to oxygen deficiency [37]. Mn-doped GaN and Mn-doped ZnO have been intensively studied however, the origins of their ferromagnetism are still not fully understood [38]. They have been controversies about the origins of ferromagnetic ordering to be due to a change of electronic band structure, a carrier-induced mechanism, or an oxygen-vacancy-stabilized metastable ferromagnetic phase [39].

2.6 Thermal properties

The thermal properties of a semiconductor determine the response of the material to temperature changes. These properties depend on the ambient temperature and the ultimate temperature limit which is 1975 K for ZnO. The thermal properties of wurtzite ZnO include its thermal expansion and thermal conductivity [1].

2.6.1 Thermal expansion coefficients

The thermal expansion coefficients of a material are defined as α_a and α_c (for in and out of plane cases, respectively) and describe lattice deformation as a function of temperature. For ZnO, these coefficients are given as $\alpha_a = 4.31 \times 10^{-6} \text{ K}^{-1}$ and $\alpha_c = 2.49 \times 10^{-6} \text{ K}^{-1}$ at 300 K. Figure 2.8 shows the results of the temperature dependence on the lattice parameters of ZnO

employed in the range 4.2 – 296 K using the X-ray powder diffraction method. In order to analyze the dependence of the lattice parameter on temperature, fourth order polynomials were fitted by using the least square method, giving a minimum for a_0 at 93 K. The c_0 parameter doesn't give any minimum, probably due to its low precision and uncertainty in the measurement [1, 2, 22].

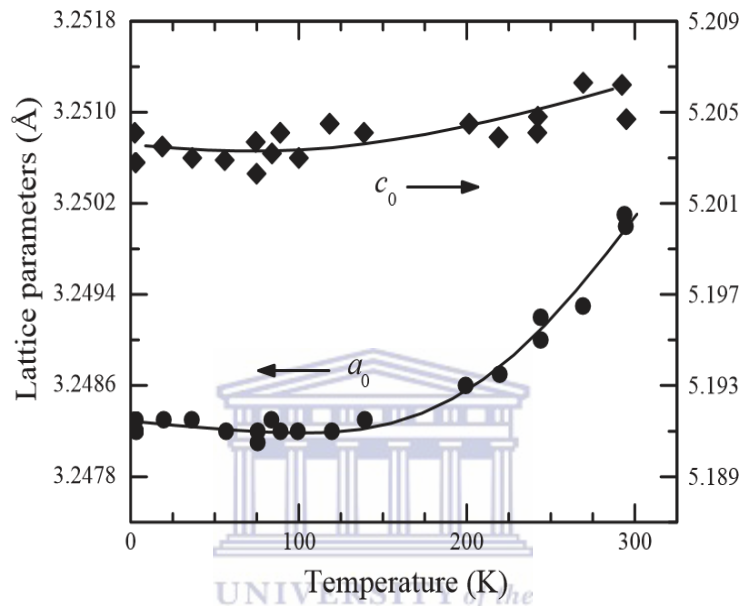


Figure 2.8: Thermal expansion of ZnO in the c-plane and along the c-axis as a function of temperature, also shown is the thermal expansion coefficient of polycrystalline ZnO [1].

2.6.2 Thermal conductivity

ZnO, like most semiconductors, contains a large number of point defects that have a significant effect on the thermal conductivity. Thermal conductivity (κ) is influenced by the vibrational, rotational and electronic degrees of freedom and is predominately limited by phonon-phonon scattering in a pure crystal. This property is extremely important when high power or high temperature electronic and optoelectronic devices are considered. The lattice contribution (phonon scattering) to the thermal conductivity is obtained from the kinetic theory as

$$\kappa_{\text{lattice}}(T) = \frac{1}{3} v_s C_{\text{lattice}}(T) L(T) \quad (2.1)$$

where T is the temperature, v_s is the velocity of sound (almost independent of temperature), $c_{\text{lattice}}(T)$ is the lattice specific heat, and $L(T)$ is the phonon mean free path. In almost all

materials, $\kappa(T)$ first increases with temperature, reaches a maximum (κ_{\max}) at some characteristic temperature T_{CH} , and then decreases. Figure 2.9 shows the measured thermal conductivity of a fully dense sintered ZnO sample heated from room temperature to 1000 °C. The thermal conductivity decreases from decreases from 37 to 4 $\text{Wm}^{-1}\text{K}^{-1}$ as the temperature is increased from room temperature to 1000 °C [1, 22].

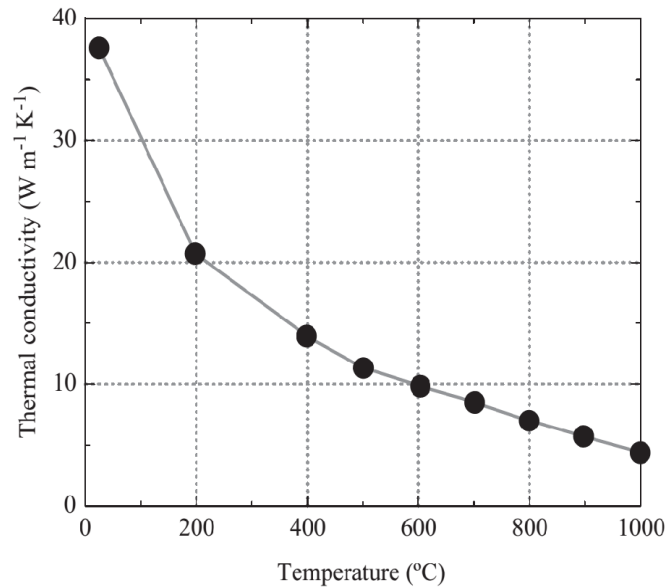


Figure 2.9: Thermal conductivity of fully sintered ZnO heated from room temperature to 1000 °C [1].

2.7 ZnO applications

ZnO is a very old technological material since it dates back to the late 1800's when its white powder was used in water colours and oil based paint [40]. ZnO nanoparticles have been paid attention to because of their unique properties. What has captured most of the attention in recent years is the fact that ZnO is a semiconductor with a direct band gap of approximately 3.4 eV, which in principle enables optoelectronic applications in the blue and UV regions of the spectrum including light emitting diodes, laser diodes and photodetectors. Its free exciton binding energy of 60 meV allows ZnO's efficient excitonic emission to persist at room temperature and higher, thus making it a promising material for optical devices that are based on excitonic effects. Due to its strong luminescence in the green-white region of the spectrum, ZnO is a suitable material for phosphor applications such as vacuum fluorescent displays and field emission displays. The high thermal conductivity and high catalytic efficiency of ZnO makes it useful as an additive in rubber (to increase the thermal

conductivity of tires), ceramic processing, waste treatment, and in the manufacture of sunscreens [18 - 22]. In fact, ZnO offers better protection and improved opaqueness as it can absorb both UV-A and UV-B radiation unlike its competitor, TiO₂ which can only block UV-B radiation. Thus, it contributes to various hair and skin care products such as powders and creams that protect the skin by absorbing the sun's harmful UV rays and promote healing. Also, ZnO enhances effectiveness of ointments, deodorants, soaps and anti-dandruff products. ZnO has been reported to have strong sensitivity toward presence of adsorbed species, making it applicable as a cheap smell sensor capable of detecting the freshness of foods and drinks [41]. ZnO has also attracted attention due to the possibility of making thin-film transistors on flexible substrates with high electron mobility when compared with amorphous silicon or organic semiconductors and is a well-known suitable candidate for the TCO layer of the thin film compound solar cells [42, 43].



2.8 References

- [1] U. Ozgur and H. Morkoc, "General Properties of ZnO," in *Zinc Oxide: Fundamentals, Materials and Device Technology*, Weinheim, Wiley-VCH, pp. 1-70, 2009.
- [2] R. Panwar, "Preparation of modified ZnO nanoparticles by sol-gel process and their characterization," Punjab, 2009.
- [3] A. Onodera and M. Takesada, "Electronic Ferroelectricity in II-VI Semiconductor ZnO," in *Advances in Ferroelectrics*, Sapporo, Intech, pp. 231-225, 2013.
- [4] A. Singh and H. Vishwakarma, "An Existential Study on Structural, Optical and Electrical Properties of ZnO Nanoparticles and Nanorods," *IOSR Journal of Applied Physics*, vol. 6, no. 2, pp. 28-32, 2014.
- [5] M. Vaseem, A. Umar and Y. Hahn, "ZnO nanoparticles: Growth, Properties and Applications," in *Metal Oxide Nanostructures and their Applications*, A. Umar and Y. Hahn, Eds., Carlifornia, American Scientific Publishers, pp. 1-36, 2010.
- [6] Z. Wang, "Zinc Oxide Nanostructures: Growth. Properties and Applications," *Journal of Physics: Condensed Matter*, vol. 16, no. 1, pp. R829-R858, 2004.
- [7] J. Behler, "A Neural Network Potential for Zinc Oxide," [Online]. Available: <http://www.theochem.ruhr-uni-bochum.de/~joerg.behler/zno.htm>. [Accessed 16 February 2016].
- [8] T. Hanada, "Basic Properties of ZnO, GaN and Related Materials," in *Oxide and Nitride Semiconductors; Processing, Properties and Applications*, T. Yao and S. Hong, Eds., Heidelberg, Springer, pp. 1-19, 2009.
- [9] "Zinc oxide," [Online]. Available: https://en.wikipedia.org/wiki/Zinc_oxide. [Accessed 28 January 2016].
- [10] B. Zeghbroeck, "Semiconductor Fundamentals," [Online]. Available: https://ecee.colorado.edu/~bart/book/book/chapter2/ch2_2.htm. [Accessed 16 February 2016].

2016].

- [11] “Direct and Indirect Band Gap Semiconductor,” [Online]. Available: <http://www.doitpoms.ac.uk/tlplib/semiconductors/direct.php>. [Accessed 28 January 2016].
- [12] “Smiconductors/What is a Semiconductor?,” [Online]. Available: https://en.wikibooks.org/wiki/Semiconductors/What_is_a_Semiconductor. [Accessed 19 February 2016].
- [13] J. Singh, *An Introduction to Solar Cell Technology*, New York: John Wiley, 2001.
- [14] R. Adam, “Synthesis and Characterization of Silver Nanoparticles for Photovoltaic Application,” Bellville, 2013.
- [15] “Wide-bandgap semiconductor,” [Online]. Available: https://en.wikipedia.org/wiki/Wide-bandgap_semiconductor. [Accessed 28 January 2016].
- [16] H. Abebe, “Introduction to Semiconductors,” in *Introduction to Applied Modern Physics*, Carlifornia, Abebe, H, pp. 121-149, 2007.
- [17] M. Willander, O. Nur, J. Sadaf, M. Qadir, S. Zaman, A. Zainelabdin, N. Bano and I. Hussain, “Luminescence from Zinc Oxide Nanostructures and Polymers and their Hybrid Devices,” *Materials*, vol. 3, no. 4, pp. 2643-2667, 2010.
- [18] A. Janotti and C. Van de Walle, “Fundamentals of Zinc Oxide as a Semiconductor,” *Reports on Progress in Physics*, vol. 72, no. 12, pp. 1-29, 2009.
- [19] A. Janotti, J. Varley, J. Lyons and C. Van de Walle, “Controlling the Conductivity in Oxide Semiconductors,” in *Functional Metal Oxide Nanostructures*, vol. 6, J. Wu, J. Cao, W. Han, A. Janotti and H. Kim, Eds., Santa Barbara, Springer, pp. 23-35, 2012.
- [20] A. Janotti and C. Van de Walle, “Native Point Defects and Doping in ZnO,” in *Zinc Oxide Materials for electronic and optoelectronic device applications*, C. Litton, D. Reynolds and T. Collins, Eds., West Sussex, Wiley, pp. 113-134, 2011.

- [21] C. Van de Walle, "Oxides as Semiconductors," Santa Barbara, 2014.
- [22] C. Jagadish and S. Pearton, Zinc Oxide Bulk, Thin Films and Nanostructures: Processing, Properties and Applications, Amsterdam: Elsevier, 2006.
- [23] W. Mtangi, F. Auret, M. Diale, W. Meyer, A. Chawanda, H. de Meyer, P. Janse van Rensburg and J. Nel, "Effects of high temperature annealing on single crystal ZnO and ZnO devices," *Journal of Applied Physics*, vol. 111, no. 1, pp. 1-6, 2012.
- [24] J. Lyons, C van de Walle, A. Janotti, "Why nitrogen cannot lead to p-type conductivity in ZnO," *Applied Physics Letters*, vol. 95, no. 25, pp. 1-3, 2009.
- [25] F. Giovannelli, "Synthesis of Al doped ZnO nanoparticles by aqueous coprecipitation," *Powder Technology*, vol. 262, no. 1, pp. 203208, 2014.
- [26] L. Yuan-Qing, "Preparation and electrical properties of Ga-doped ZnO nanoparticles by a polymer pyrolysis method," *Materials Letter*, vol. 64, no. 15, pp. 1735-1737, 2010.
- [27] G. Machado, D. Guerra, D. Leinen, J. Ramos-Barrado, R. Marotti and E. Dalchielea, "Indium doped zinc oxide thin films obtained by electrodeposition," *Thin Solids Films*, vol. 490, no. 2, pp. 124-131, 2005.
- [28] R. Yousefi, A. Zak and M. Mahmoudian, "Growth and characterization of Cl-doped ZnO hexagonal nanodisks," *Journal of Solid State Chemistry*, vol. 184, no. 10, pp. 2678-2682, 2011.
- [29] Z. Yan-Zhen, "Investigation of iodine dopant amount effects on dye-sensitized hierarchically structured ZnO solar cells," *Materials Research Bulletin*, vol. 55, no. 1, pp. 182-189, 2014.
- [30] M. Kumar, "Growth of p-type ZnO thin film on n-type silicon substrate and its application as hybrid homojunction," *Current Applied Physics*, vol. 11, no. 1, pp. 65-69, 2011.
- [31] J. Fan, "p-Type ZnO Materials: Theory, Growth, Properties, and Devices," *Progress in Materials Science*, vol. 58, no. 1, pp. 874-985, 2013.

- [32] X. Li, "p-Type ZnO Thin Films Grown," in *IEEE Photovoltaics Specialists Conf. and Exhibition*, Florida, 2005.
- [33] A. Diallo, "Green synthesis of ZnO nanoparticles by *Aspalathus Linearis*: Structural and Optical Properties," *Journal of Alloys and Compounds*, vol. 646, no. 1, pp. 425-430, 2015.
- [34] L. Yang, "Synthesis and Optical Properties of ZnO Nanostructures," Sweden, 2008.
- [35] J. Ungula, "Growth and characterization of ZnO nanoparticles by sol-gel process," QwaQwa, 2015.
- [36] N. Rajkumar and K. Ramachandran, "Structural, Optical and Magnetic Investigations on undoped and Mn-doped ZnO Nanoparticles," *International Journal of Nanoscience*, vol. 9, no. 5, pp. 495-502, 2010.
- [37] V. Sharma and G. Varma, "Oxygen vacancies induced temperature ferromagnetism in hydrogenated Mn-doped ZnO," *Journal of Applied Physics*, vol. 102, no. 5, pp. 1-3, 2007.
- [38] C. Schnohr and M. Ridgway, *X-Ray Absorption Spectroscopy of Semiconductors*, Berlin: Springer, 2015.
- [39] S. Kumar, "Insight into the origin of ferromagnetism in Fe-doped ZnO diluted magnetic semiconductor nanocrystals: an EXFAS study of local structure," *RSC Advances*, vol. 5, no. 115, pp. 94658-94669, 2015.
- [40] K. Ellmer and A. Klein, "Zinc Oxide and its Applications," in *Transparent Conductive Zinc Oxide-Basics and Applications*, K. Ellmer, A. Klein and B. Rech, Eds., New York, Springer, pp. 1-33, 2008.
- [41] C. Wang, L. Zhang, D. Xiang and R. Gao, "Metal Oxide Gas Sensors: Sensitivity and Influencing Factors," *Sensors*, vol. 10, no. 3, pp. 2088-2106, 2010.
- [42] Q. Peng and Y. Qin, "ZnO Nanowires and their Application for Solar Cells," in *Nanowires-Implementations & Applications*, Nanchang, InTech, pp. 157-178, 2011.

- [43] S. Gunalan, R. Sivaraj and V. Rajendran, “Green synthesis of ZnO nanoparticles against bacterial and fungal pathogens,” *Progress in Natural Science: Materials International*, vol. 22, no. 6, pp. 693–700, 2012.

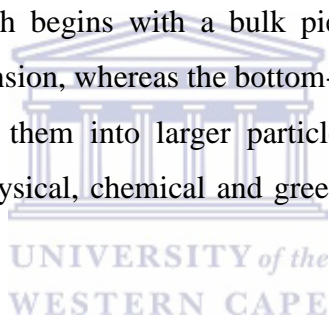


Chapter 3: Synthesis methods

Nanoparticles are known as the fundamental building blocks of nanotechnology, a study dedicated to materials sized from 1 to 100 nm [1]. As a result, the synthesis of many nanoparticles has become an important component in nanoscale science and engineering. Amongst them, zinc oxide (ZnO) nanoparticles are of great interest due to several favourable properties including good transparency, high electron mobility, wide band gap, and room-temperature luminescence. A wide range of nanoparticles in the form of colloids, clusters, powders, tubes, rods, wires, thin films, etc. can be prepared by a variety of methods [2].

This chapter focusses on some of the commonly used methods for preparing ZnO nanoparticles and also discusses the advantages, disadvantages, as well as limitations associated with the different methods.

Nanoparticle synthesis is divided broadly into two categories: “top-down” and “bottom-up” methods. The top-down approach begins with a bulk piece of starting material and then reduces it to the nano-sized dimension, whereas the bottom-up approach starts from atomic or molecular levels and assembles them into larger particles. These synthesis methods are further broadly classified into physical, chemical and green chemistry methods as shown in Figure 3.1 [3, 4].



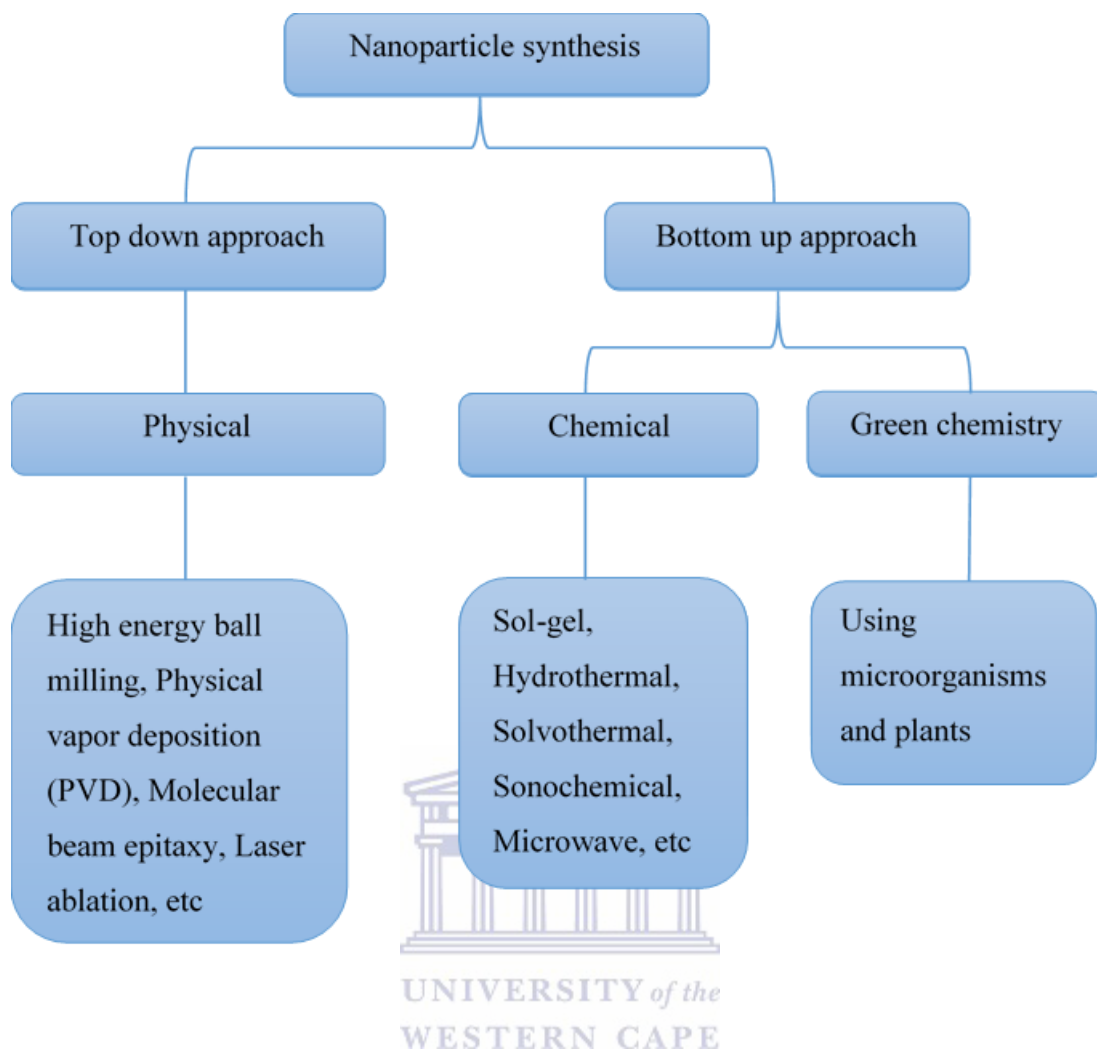


Figure 3.1: The different synthesis methods for growing nanoparticles [5].

3.1 Physical methods

The physical synthesis approach includes a variety of methodologies (as shown in Figure 3.1) which are favoured for their high quality ZnO nanoparticles. These methodologies include ball milling, physical vapor deposition, thermal evaporation, sputter deposition, molecular beam epitaxy, laser ablation, chemical vapor decomposition, thermal evaporation and condensation, amongst others [6]. However, this methods necessitate high vacuum and high temperatures which not only require special attention by operating personnel but also a cooling water system to dissipate large heat loads [7, 8].

3.1.1 High Energy Ball Milling

High Energy Ball Milling, also known as mechanical alloying, is a process where a powder mixture of micron size is placed in the ball mill and subjected to high energy collision from the balls. As containers are rotating at a few hundred rounds per minute (rpm), the material is forced to the walls and is pressed against the walls as illustrated in Figure 3.2, thus, producing fine, uniform dispersions of oxide particles. The milling process can be carried out using different apparatus such as attritor, planetary mill or a horizontal ball mill [2, 9, 10].

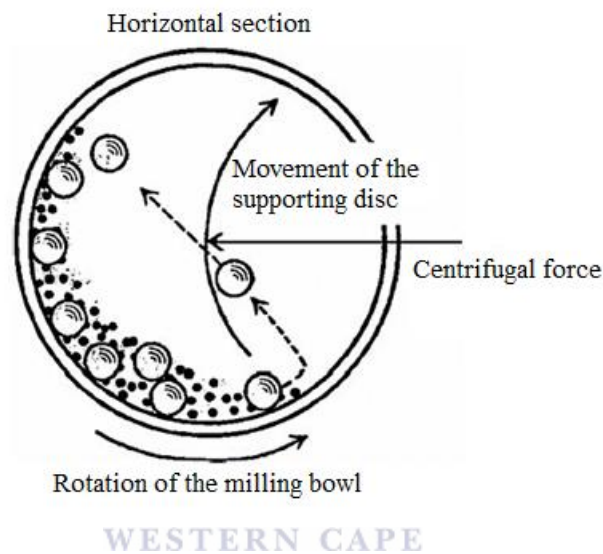


Figure 3.2: Schematic view of the motion of the ball and the powder mixture [9].

Amikhanlou et al. [11] reports on using the high energy planetary ball milling to obtain spherical ZnO nanoparticles with a crystallite size of 5 nm and a particle size of about 60 nm from milling commercial ZnO with an average particle size for 8 hours. The milling was carried out at a rotation speed of about 300 rpm in air and at room temperature. Similarly, Salah et al. [12] obtained spherical ZnO nanoparticles using a high energy horizontal oscillatory mill carried out at a similar speed of 300 rpm in ambient temperature. Their commercial ZnO nanoparticles (size $\sim 0.6 - 1 \mu\text{m}$) was milled for different times ranging from 2 to 50 hours.

Advantages of the ball milling method [2, 5]

- I. Simple and efficient.
- II. Formation of alloying phase at low temperature.

Disadvantages of the ball milling method [13, 14]

- I. Powder impurities from the balls added during the milling.
- II. High energy requirement.
- III. Extensive long period of milling time.

3.1.2 Physical Vapor Deposition

Physical Vapor Deposition (PVD) process, often called thin film process, is a collective set of processes used to deposit thin layers of material. This technique basically involves the vaporization of the material from a solid or liquid source through a high temperature vacuum and transportation of the vapor in vacuum to the substrate surface, where it is condensed onto the substrate to generate thin films [15, 16]. These fundamental steps are shown in Figure 3.3. PVD process can be divided into two most common processes, namely, thermal evaporation and sputtering. In both processes, the resulting vapor phase is subsequently deposited onto the desired substrate through a condensation mechanism [17].

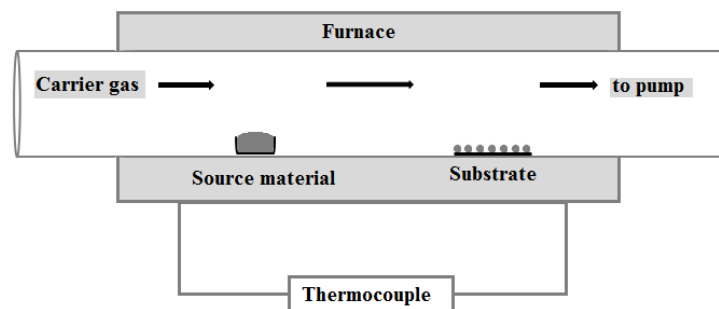


Figure 3.3: Schematic diagram of the thermal evaporation system [18].

3.1.2.1. Thermal evaporation

Thermal evaporation involves vaporizing the condensed or powder material (source) at an elevated temperature and then condensing the resultant vapor phase to form the desired product. The process takes place inside a low pressure vacuum chamber as shown in Figure 3.3. The high purity source materials contained in a quartz boat are placed in the middle of the furnace, the highest temperature region. The substrates for collecting the desired nanostructures are placed down-stream following the carrier gas. During the experiment, the source materials are vaporized at the high temperature and low pressure region. The vapor is

then carried by the inert carrying gas such as argon or nitrogen down to the lower temperature region, where the vapor gradually becomes supersaturated. The reaction temperature and pressure are held for a certain period of time to vaporize the source material and achieve a reasonable amount of deposition. Table 3.1 summarises the synthesis conditions used to synthesis various ZnO nano-structures by the thermal evaporation method [19, 20].

Table 3.1: Thermal evaporation synthesis conditions and morphology characteristics of ZnO.

Nanostructure	Source material	Substrate	Evaporation temperature (°C)	Carrier gas	Diameter (nm)	Reference/s
Nanorods	Zn granule	ZnO/Si(100)	600	Ar/O ₂	50	[21]
Nanowires	Zn/ZnO powders	Si(111) wafers	1300	Ar	30 - 100	[22]
	ZnO powder	Au coated Si(100)	960	Ar	260 - 350	[23]
Nanobelt	ZnS powder	Si	1050	Ar/O ₂ /H ₂	20 - 100	[24]

UNIVERSITY OF WESTERN CAPE

3.1.2.2. Sputtering

Sputtering is a special type of PVD process. In sputtering, the target material and the substrate is placed in a vacuum chamber. A voltage is then applied between them so that the target is the cathode and the substrate is attached to the anode, as shown in Figure 3.4. A plasma is created by ionizing a sputtering gas (usually Argon). The sputtering gas bombards the target and sputters off the material of interest [25]. The different types of sputtering power sources that are used to bombard the target material to sputter the atoms are summarised in Table 3.2. Ghafouri, et al. [26] reports on fabricating crystalline ZnO nano grains (in the range 50 - 100 nm) on glass substrates and ZnO nanoparticles (in the range 40 - 150 nm) and nanorods (with diameter of 60 nm and length of about 650 nm) on silicon substrates by RF sputtering. Similarly in 2014, Rashid et al. [27] used the low temperature Radio Frequency (RF) sputtering deposition method to synthesize ZnO thin films over glass substrate. The produced thin film with a thickness of 200 nm was used as a catalyst for the photodegradation of 2-chlorophenol (2-CP).

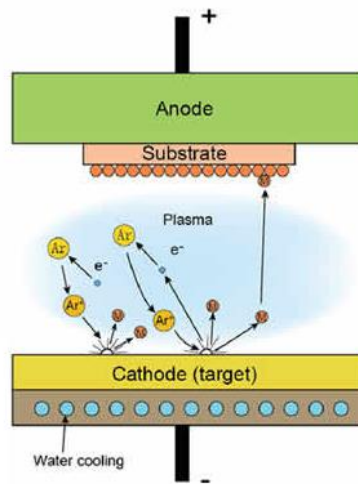


Figure 3.4: Schematic diagram of the Sputtering process. Argon is ionized by a strong potential difference. After impact the target atoms are released and travel to the substrate where they form layers of atoms in the thin film [28].

Table 3.2. Various types of sputtering magnetrons power sources [29 - 35].

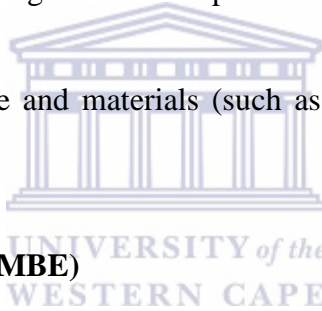
Power source	Explanation	Limitations
Direct Current (DC) Sputtering	Usually used with electrically conductive target materials like metals	Coatings which are non-conducting (insulating materials) cause a build-up of charge on the target surface once the insulating layer has been established
Radio Frequency Magnetron Sputtering (RF-MS)	Mainly used to sputter thick electrically insulating target materials such as ceramics	Have a low deposition rate due to lack of secondary electrons for gas ionization
Pulsed DC Sputtering	Particularly used for reactive dielectric compounds essentially impossible with straight DC	Transients are more severe
Mid Frequency Alternating Current (MD AC) Sputtering	Used for depositing non-conductive thin film coatings	Substrate heating higher compared to DC sputtering

Advantages of the Sputtering Process for Deposition [35, 36]:

- I. Replication of target composition in the deposited films is achievable.
- II. Materials with very high melting point are easily sputtered.
- III. Sputtered films usually have a better adhesion on the substrate.
- IV. Deposition of a wide variety of metals, insulators, alloys and composites are possible.
- V. Capable of in-situ cleaning prior to film deposition by reversing the potential on the electrodes.

Disadvantages of the Sputtering Process for Deposition [37]:

- I. Difficult to deposit uniformly on complex shapes, e.g. turbine blades.
- II. Localization of the plasma over the substrate tends to be built into the growing film.
- III. High performance thick coatings are hard to produce due to high internal residual stress levels.
- IV. Undergoes substrate damage and materials (such as organics) degradation due to ion bombardment.



3.1.3 Molecular Beam Epitaxy (MBE)

This is a modified evaporation method which takes place in an ultra-high vacuum system of $\sim 10^{-8} - 10^{-12}$ Torr. Elements such as gallium and arsenic in their ultra-purest form are separately heated in the source cells referred to as Knudsen effusion cells. The molecular beams generated from these source cells are incident upon a heated substrate which can be a semiconductor material for instance: silicon, germanium, or gallium arsenide, as shown in Figure 3.5. The arriving constituent atoms condense and build up (grow) on the substrate under kinetically controlled conditions, producing ultra-thin layers one atomic layer at a time. The Reflected High Energy Electron Diffraction (RHEED) technique is incorporated to monitor the crystallinity of the growing film [38, 39].

Asgar et al. [40] presented a study on MBE-assisted synthesis of ZnO nanorods. ZnO layers of $\sim 1 \mu\text{m}$ were grown on a p-type silicon wafer at a temperature of 300 °C. This resulted in ZnO nanorods which were 100 nm in length. They further studied the properties of the p-n junction observed between Si/ZnO, which showed n-type conductivity with a carrier concentration of

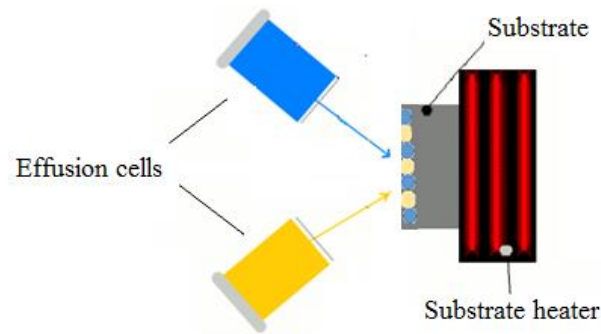


Figure 3.5: Schematic diagram of molecular beam epitaxy showing the evaporation of atoms or molecules from two different sources onto a heated substrate [42].

$1 \times 10^{15} \text{ cm}^{-3}$. Wang et al. [41] investigated the influence of Mg concentrations on the structural, optical and electrical properties of single and multiple (three) ZnO/ZnMgO quantum wells grown on sapphire by MBE. The investigation revealed that the thicker first ZnMgO barrier layer accumulated larger compressive stress to achieve higher quality ZnO/ZnMgO quantum well. They also found out that the multiple quantum well (MQW) structure increased the light emission efficiency of the sample.

Advantages of using the MBE method [43, 44]:

- I. Has a very low defect concentration.
- II. Extremely thin films can be fabricated in a very precise controlled way.
- III. Has the ability to make high quality semiconductor crystals from a number of different elements, instead of from a single element.

Disadvantages associated with the MBE method [43, 45]:

- I. Complex and expensive setup.
- II. It is a slow method with a crystal growth rate of usually a few microns per hour.

3.1.4 Laser ablation

In the Laser ablation method, vaporization of the material is achieved by using pulses of laser beam of high power. A typical schematic diagram of the laser ablation is shown in Figure 3.6. The high powerful beam of the laser induces large light absorption on the surface target, thus vaporizing the material on the surface (substrate) into a smoke particulate debris called laser plume [46, 47].

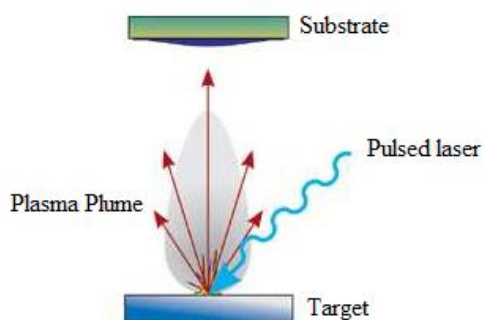


Figure 3.6: Laser ablation schematic diagram [48].

In order to achieve an efficient high purity synthesis, the laser ablation of a solid target is generated in liquid dispersions. The substrate ablated by a pulsed laser beam in a liquid medium releases nanoparticles that are stabilized by the surrounding medium against agglomeration and contamination originating from unreacted **educts** [48]. The synthesis of hexagonal rod-like nanostructures was achieved by Ishikawa et al. [49] by irradiating a harmonic Nd:YAG laser operated at 10 Hz at a pulse width of 7 ns on a Zn metal plate immersed in deionized water with a temperature of 80 °C. Conversely, Usui et al. [50] irradiated a Zn metal plate immersed in a cationic surfactant with the Nd:YAG pulse laser at 10 Hz and a pulse width of 5 - 7 ns to obtain spherically shaped ZnO nanoparticles with an average diameter of 38 nm. Singh, et al. [51] synthesized ZnO nanocrystals by combination of pulsed laser ablation of a piece of zinc metal in an aqueous media of anionic Sodium dodecyl sulfate (SDS) with simultaneous flow of pure oxygen. The piece of metal was irradiated with a second harmonic of a pulsed Nd:YAG laser operated at 10 Hz.

Advantages of using the laser ablation method [52, 53]:

- I. There is no need for solvents and harsh chemicals.
- II. Doesn't have pattern or geometry limitations.
- III. Ablation can be combined with other laser processes for a complete manufacturing solution.
- IV. Direct elemental analysis of large variety samples.

Disadvantages of using the laser ablation method [5, 13, 54]:

- I. Low production rate.
- II. High energy consumption.

- III. Is an expensive and uneconomical method.
- IV. Difficult to obtain uniform and stable nanoparticles.

3.2 Chemical methods

The chemical method is also known as the bottom-up approach. The wet chemical method generally refers to a group of methods that use the liquid phase at one of the process stages. These methods include sol gel, hydrothermal decomposition, solvothermal decomposition, liquid ultrasonication, free surfactant microwave, solution plasma, electrochemical reaction, and solid state chemistry [2]. In some of these methods, nanoparticles are obtained as colloidal particles in solutions, which can be filtered and dried to obtain powder. Depending on the chemicals used and reaction conditions, particles of different shapes and sizes at lower temperatures are easily obtainable from these chemical methods [10, 55, 56].

3.2.1 Sol-gel

The sol-gel technique is one of the attractive and versatile wet chemical method. Sol-gel method involves the formation of solid particles in a liquid called sol, followed by the crosslinking of the ‘sol’ to form a continuous network of particles (enclosed with liquid) called a gel. The most commonly used precursors are the metal alkoxides, which are compounds whereby a metal is bonded to one or more alkyl groups through an intermediate oxygen atom. Other precursors that serve as sol forming constituents include metal organic compounds, salts of inorganic acids and salts of organic acids [2, 10, 57].

A typical sol-gel process, as the one shown in Figure 3.7, generally involves four stages, namely, hydrolysis of the precursor/s, condensation and polymerization process that establishes metal–OH–metal or metal–O–metal bridges between metallic atoms of the precursor materials, growth of particles, and agglomeration of particles. These stages are followed by the formation of networks that extend throughout the liquid medium, resulting in the formation and congealing of the gel [2, 58, 59].

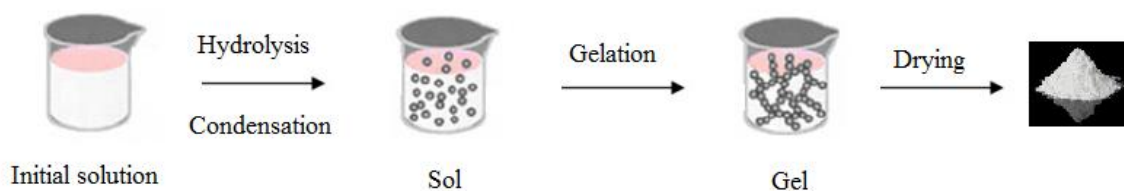


Figure 3.7: Schematic diagram of a sol-gel process for nanopowders [60].

A number of ZnO nanoparticles, nanorods or nanotubes have been synthesized using the sol gel method [61]. Hasnidawani et al. [62] reported on synthesizing ZnO nanoparticles via the sol gel method using zinc acetate dihydrate ($\text{Zn}(\text{CH}_3\text{COO})_2 \cdot 2\text{H}_2\text{O}$) as a precursor, ethanol (CH_2COOH) as solvent, and sodium hydroxide (NaOH) and distilled water (H_2O) as solvent medium. The results showed ZnO rod-like structure within the range 81.2 nm - 84.9 nm. On the other hand, Jurablu et al. [63] obtained spherically shaped ZnO nanoparticles with an average particle size of 28 nm by the sol-gel method using zinc sulphate heptahydrate ($\text{ZnSO}_4 \cdot 7\text{H}_2\text{O}$) and diethylene glycol as surfactant. Khan et al. [64] obtained thorn like ZnO nanoparticles of less than 50 nm. The starting reagents used for this synthesis were Zinc acetate dihydrate and sodium hydroxide while cetyltrimethylammonium bromide (CTAB) was used as a capping agent.

The advantages of the sol-gel method [65, 66]:

- I. Sol gel formation is a relatively low temperature process.
- II. Uses less energy consumption thus less pollution too.
- III. Sintering at low temperature possible.
- IV. Allows the fine control of the product's chemical composition.
- V. Can create very fine powders of high purity.

Disadvantages of the sol-gel method [10, 63]:

- I. High cost of the raw materials (the chemicals).
- II. Often, there's a large volume shrinkage and cracking during drying.
- III. Very much substrate dependent in the case of thin film synthesis.
- IV. Since several steps are involved, close monitoring of the process is required.

3.2.2 Hydrothermal/solvothermal synthesis

Hydrothermal synthesis is generally defined as the method of crystal synthesis that is based on the ability of an aqueous solvent at moderate to high temperature and pressure to facilitate the interaction of precursors during synthesis [67, 68]. When any solvent other than water is used, the method is called solvothermal synthesis. Synthesis under hydrothermal/solvothermal conditions is usually performed in the presence of a solvent (aqueous or non-aqueous) at a temperature greater than 25 °C and at pressure above 0.1 MPa. The crystallization process is carried out in a steel pressure vessel called autoclave (shown in Figure 3.8), in which adequate chemical precursors are dissolved in the solvent under

hydrothermal/solvothermal conditions [10]. The autoclave is heated and maintained between two temperature zones, a hotter end and a cooler end. The saturated solution is transported from the hotter end and becomes supersaturated in the cooler end thus forming the desired crystal [69]. A number of articles have been devoted to synthesize ZnO as thin films and nanoparticles. Aneesh, et al. [70] reports on synthesizing ZnO nanoparticles with an average size of about 7 to 24 nm by varying the concentration of the NaOH precursor into the methanol prepared $\text{Zn}(\text{CH}_3\text{COO})_2 \cdot 2\text{H}_2\text{O}$ solution. Reddy et al. [71] obtained ZnO nano crystals of diameters ranging from 9 to 12 nm by varying the NaOH concentrations. Zinc nitrate hexahydrate ($\text{Zn}(\text{NO}_3)_2 \cdot 6\text{H}_2\text{O}$) and sodium hydroxide (NaOH) were used as the starting precursors. Sun, et al. [72], synthesized ZnO crystal thin from the hydrothermal reaction on sapphire substrate.

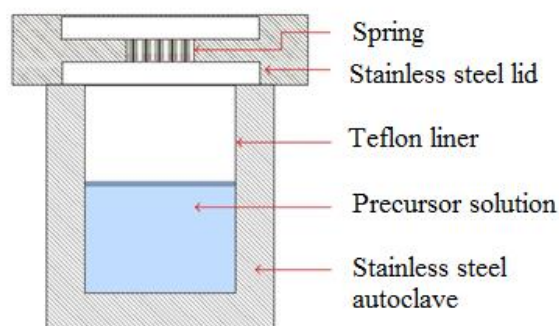


Figure 3.8: Schematic illustration of the autoclave used in the hydrothermal synthesis [73].

Advantages of the hydrothermal/solvothermal method [10]:

- I. Possible to precipitate powders directly from solution
- II. Ability to synthesize crystals of substances which are unstable near melting point
- III. Suitable when it is difficult to dissolve precursors at room or lower temperatures
- IV. Can be hybridised with other processes like microwave, electrochemistry, ultrasound, etc.

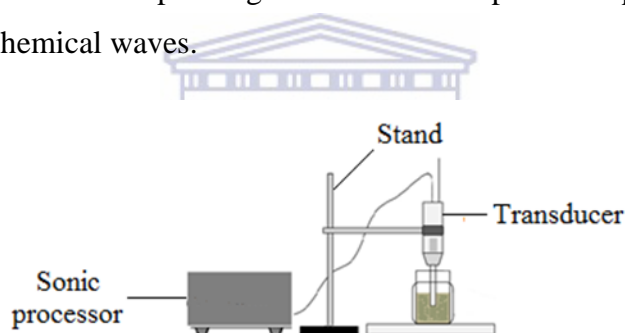
Disadvantages of the hydrothermal/solvothermal method [69, 74]:

- I. High cost of equipment e.g. the need of expensive autoclaves
- II. Inability to observe the crystals in the process of their growth

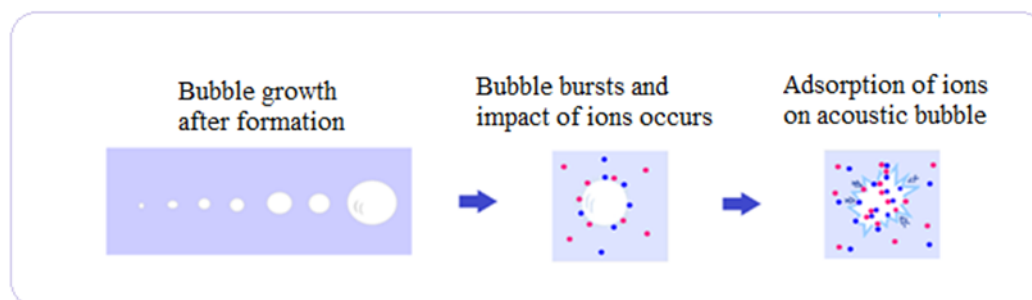
3.2.3 Sonochemical synthesis

Sonochemistry is the method that depends on the application of ultrasound energy to chemical reactions. The transducer generates sound waves in a frequency range of 20 kHz to 10 MHz, thus producing void bubbles known as cavitation bubbles as illustrated in Figure 3.9. These cavitation bubbles keep on growing until they reach a critical size and then collapse, releasing very large amount of energy reaching a localized temperature of $\sim 5000\text{ }^{\circ}\text{C}$ and a pressure of $\sim 180\text{ MPa}$ [2, 75].

In order to investigate the direct transformation of $\text{Zn}(\text{OAc})_2 \cdot 3\text{H}_2\text{O}$ precursor to create ZnO nanoparticles, Azadeh et al. [76] employed ultrasonic technique. Nanocrystalline ZnO particles were prepared from the ultrasonic irradiation of zinc acetate dissolved in ethanol and sodium hydroxide at a frequency of 20 kHz with a maximum power output of 600 W. Also, ZnO nanoparticles have been synthesized by ultrasonic irradiation of an aqueous–alcoholic-ethylenediamine (EDA) solution of zinc nitrate and sodium hydroxide as reported by Yadav, et al. [77]. A sonochemical bath operating at 33 KHz and a power output of 350 W was used as the source of sonochemical waves.



I.



II.

Figure 3.9: Schematic diagram illustrating (i) the setup, (ii) acoustic cavitation effect in the sonochemical synthesis [78, 79].

The advantages of using sonochemical method [13, 80]:

- I. Cheap to get started in a field
- II. Has the capacity to form uniform shapes and narrow distributions of particle size
- III. Uses high velocity rates and controllable reaction conditions

Disadvantage of sonochemical method [5, 13]

- I. The explanation as to how the nano structured products are created is not fully understood.
- II. Very small concentration of the prepared nanoparticles

3.2.4 Microwave synthesis

Microwave energy is a form of electromagnetic energy within the frequency range of ~300 – 300 000 MHz [81]. Microwave heating is caused by the energy transferred to molecules through the mechanism of dipole rotation, a process (shown in Figure 3.10) wherein molecules orient their dipoles with the rapidly changing electric field [2]. While conventional heating works by means of a heated surface which in turn heats the reaction vessel content, microwave reaction solutions are heated directly and volumetrically with the molecules that are present in the reaction mixture [82]. This direct interaction results in extremely fast heating rates not reproducible with conventional heating [83].

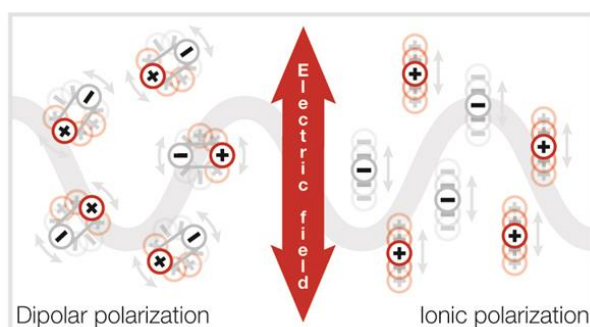


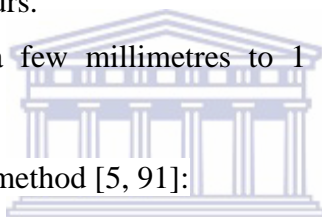
Figure 3.10: The rotation of a molecule under the influence of the electric field component in an electromagnetic wave [84].

Hasanpoor et al. [85], reported microwave-assisted hydrothermal synthesis of ZnO nanoparticles with different morphologies. By changing the power and time of microwave irradiation, flower-shaped, needle-shaped and spherical-shaped nanoparticles with diameters

ranging from 50 - 150 nm were obtained. Barreto et al. [86] investigated the effect of different precursors, temperature and additives on the morphology of ZnO nanoparticles synthesized by the microwave-assisted technique. As a result, cauliflower-like particles with sizes in the range of 200 - 300 nm were formed. Shojaee et al. [87] synthesized ZnO nanorods using a domestic microwave oven for irradiation. These nanorods had an average diameter in the order of 112 and 117 nm. The effect of the parameters such as precursor's concentration and heating time were also studied.

Advantages associated with microwave synthesis [88 - 90]:

- I. Allows direct 'in core' heating of the reaction mixture, which results in a faster and more even heating of the reaction mixture.
- II. Purification step enhanced by reducing unwanted side reactions is faster and easier.
- III. Microwave energy enhances organic reactions by reducing chemical reaction times to few minutes instead of hours.
- IV. Permits scale-up (from a few millimetres to 1 litres) without changing reaction parameters.



Disadvantages of the microwave method [5, 91]:

- I. Microwave systems designed for synthesis use are often quite costly.
- II. Health hazard: prolonged exposure may result in complete degeneration of body tissues and cells.
- III. Has limited applicability for materials that absorb them.

3.2.5 Chemical Vapor Deposition

The chemical vapor deposition (CVD) is similar to the PVD method (described in section 3.1.2). The CVD involves exposing a substrate to one or more volatile precursor gases which decompose on the substrate surface to produce the desired deposit. The vapors of the desired material are pumped into the reaction chamber using some carrier gas, as illustrated in Figure 3.11. As they pass the heated substrate, they are drawn into the boundary layer where they are deposited onto the substrate. This process is accompanied by the production of chemical by-products that are exhausted out of the chamber along with unreacted precursor gases [92 - 94].

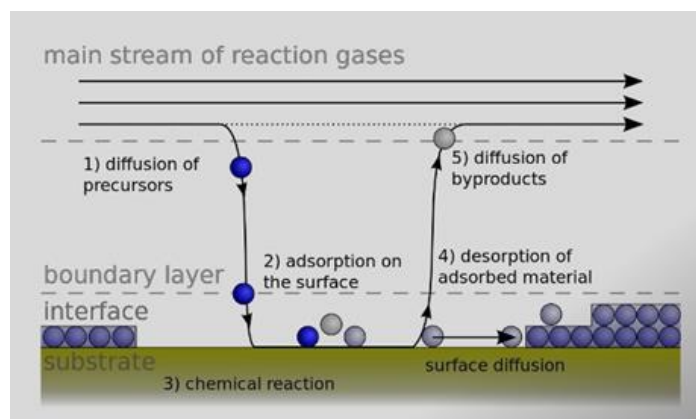


Figure 3.11: Schematic diagram showing the basic concept of the chemical vapor deposition (CVD) method [95].

The chemical vaporization method has been frequently used to synthesis functional nanoparticles. Guan et al. [96] reports on the combined synthesis and self-organization of Zn and ZnO nanoparticles into linear arrays through laser-assisted chemical vapor deposition. In this report, use of templates with laser-generated 1D arrays were produced by employing a Lloyd's mirror arrangement. Polarz et al. [97] investigated the fundamental differences between the solid-state versus the gas-phase chemistry of the formation of ZnO agglomerates using the volatile organometallic tetrameric alkyl-alkoxy zinc compound ($[\text{CH}_3\text{ZnOCH}(\text{CH}_3)_2]_4$) as precursor. The authors concluded that it was very difficult to control the size of the nanoparticles by solid-state synthesis, and that instead of isolated particles, agglomerates were always obtained. In addition to the morphological control over ZnO, they found out that it was not possible to obtain pure and defect-free materials. On the other hand, the gas phase (chemical vapor) synthesis approach showed that not only are defect-free ZnO materials obtainable, the morphological control over the ZnO is also achievable.

Advantages of the CVD method [13, 98, 99]:

- I. Precise control of composition is possible.
- II. Less waste deposition.
- III. Able to deposit materials which are hard to evaporate.
- IV. Ability to grow epitaxial films.
- V. Pressures used allow coating of three dimensional structures.

Disadvantages of the CVD method [98, 99]:

- I. Involve the frequent use of hazardous and corrosive gases.

- II. Utilize high deposition temperatures compared to the PVD method.
- III. Many precursors used are relatively expensive.

3.3 Green chemistry

Green chemistry is the fabrication of products and methods that reduce or eliminate the use and ultimately the disposal of hazardous substances out of the environment [100]. Passed in 1990 as a Pollution Prevention Act, green chemistry is a new approach for dealing with pollution by preventing environmental problems before they happen [101]. In 1998 American chemists Paul Anastas and John Warner based this initiative under the ‘12 principles of green chemistry’. These principles (summarized in Table 3.3) are a classic guide on a variety of ways to reduce the environmental and health impacts of chemical production [102, 103]. Recently, synthesis of nanoparticles using plants [106 - 108] and microorganisms including bacteria [107, 108], viruses [109, 110], fungi and yeast [111, 112] has been reported to be an eco-friendly alternative method of synthesizing a wide variety of nanoparticles [113]. Table 3.4 shows some of the different microorganisms used to synthesize different nanoparticles with a different shapes and sizes. Of these biological entities, synthesis of nanoparticles using plant parts and plant extracts has been demonstrated to be cost-effective and much simpler because it doesn’t require multi-step procedures that involve complex culturing and isolation techniques [104, 114, 115]. The ability of plants to hyper-accumulate and biologically reduce metal ions has been known since the early 1900s and has been used for extracting precious metals from land unjustifiable to mine [105, 116 - 118]. However, the use of whole plants in the synthesis of nanoparticles has certain limitations where the heterogeneity of the size and morphology of nanoparticles produced hinders their use. For instance, in clinical applications whereby the size and shape play a critical parameter effecting cell uptake, rate and site specific for drug delivery from the system [105, 119]. In this regard, using plant extracts have been favoured as a simpler alternative for synthesizing nanoparticles [120].

Crude plant extract containing various biomolecules with functional groups such as C=C (alkenyl), C=N (Amide), -O-H (phenolic and alcohol), N-H (amine), C-H and COO- (carboxylic group) are mainly responsible for the reduction and stabilization of metallic ions into metallic nanoparticles. [105, 121]. Examples of these biomolecules capable of reducing metal ions are shown in Figure 3.12. The extract can be prepared from different parts of the plants such as the stem, flower, leaf, root, shoot, petal, fruit, and peel. The extraction method

involves boiling the plant part. The obtained extract contains the reducing and capping agents needed to reduce metallic ions [106, 114, 122]. Some of the plants extracts used in the bioreduction of ZnO nanoparticles are reported in Table 3.5.

Table 3.3. The twelve principles of green chemistry which were formulated as guidelines in effort to reduce and/or eliminate environmental pollution [123].

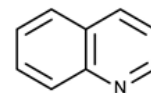
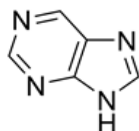
<p>1. WASTE PREVENTION</p> <p>Prevent waste from the start rather than treating or cleaning it afterwards</p>	<p>5. SAFER AUXILIARIES</p> <p>Minimize the use of solvents and other auxiliary substances and make them as innocuous as possible</p>	<p>9. CATALYSIS</p> <p>Prefer catalytic reagents-as selective as possible-over stoichiometric reagents</p>
<p>2. ATOM ECONOMY</p> <p>Design synthetic methods to maximize the incorporation of intermediate materials into the final product</p>	<p>6. ENERGY EFFICIENCY</p> <p>Minimize the energy used in chemical processes, and if possible, carry them out at ambient temperature and pressure</p>	<p>10. DEGRADABILITY</p> <p>Design chemical products for eventual disposal, so that they break down into innocuous compounds that do not persist in the environment</p>
<p>3. SAFER SYNTHESIS</p> <p>Design synthetic methods to minimize the use and generation of toxic substances</p>	<p>7. RENEWABLE FEEDSTOCKS</p> <p>Use biomass and other renewable raw materials whenever practicable</p>	<p>11. POLLUTION EVENTION</p> <p>Develop methods for real-time monitoring and control of chemical processes that might form hazardous substances</p>
<p>4. SAFER PRODUCTS</p> <p>Design chemical products to carry out their function while minimizing their toxicity</p>	<p>8. DERIVATIVE REDUCTION</p> <p>Minimize the potentially wasteful use of blocking groups and other temporary modifications of intermediates</p>	<p>12. ACCIDENT REVENTION</p> <p>Choose processes and practices that minimize the potential for chemical accidents, including releases, explosions and fires</p>

Table 3.4. A selection of biological entities used in the synthesis of nanoparticles.

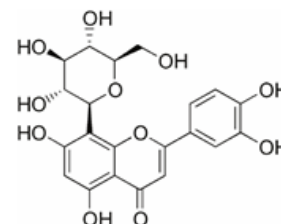
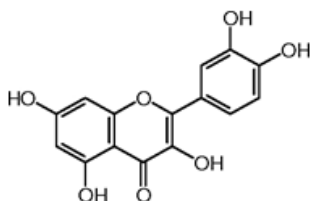
Biological entity	Type of Nanoparticle	Size (nm)	Shape	References
Bacterial species				
<i>Aeromonas hydrophila</i>	ZnO	57.72	Spherical, oval	[124]
<i>Bascillus sp</i>	Ag	42 - 92	Spherical	[125]
<i>Lactobacillus plantarum</i>	ZnO	7 - 19	Hexagonal, spherical	[126]
<i>Rhodopseudomonas capsulata</i>	Au	10 - 20	Spherical	[127]
Fungi and yeast				
<i>Aspergillus terreus</i>	Ag	1 - 20	Spherical	[128]
<i>Humicola sp</i>	Ag	5 - 25	Spherical	[129]
<i>Sacchromyces cerevisiae</i>	ZnO	52.72	Polycrystalline	[130]
<i>Sclerotium rolfsii</i>	Au	~25	Isotropic spherical	[131]
<i>Trichoderma koningii</i>	Au	30 - 50	Spheres, triangles and hexagons	[132]
Viral				
<i>Tobacco mosaic virus</i>	Au	13 - 18	Rods	[133]
<i>M13 phage</i>	Bi	~3.0	Wire-like	[134]
	Cu ₂ S	~6.5	Irregular	[135]
Plant				
<i>Azadirachta indica</i>	Ag	~34	Spherical	[136]
<i>Agathosma betulina</i>	CdO	~8	quasi-spherical	[137]
<i>Callistemon viminalis</i>	Sm ₂ O ₃	~23	Quasi-spherical	[138]
<i>Angelica archangelica</i>	Au	4 - 8	Polyhedral, spherical	[139]
<i>Hypericum perforatum</i>				
<i>Hamamelis virginiana</i>				
<i>Hibiscus Sabdariffa</i>	CdO	23 - 35	Nanocrystals	[140]
<i>Nepenthes khasiana</i>	Au	50 - 80	Triangular, spherical	[141]

<i>Psidium guajava</i>	Ag	10 - 90	Spherical	[142]
------------------------	----	---------	-----------	-------

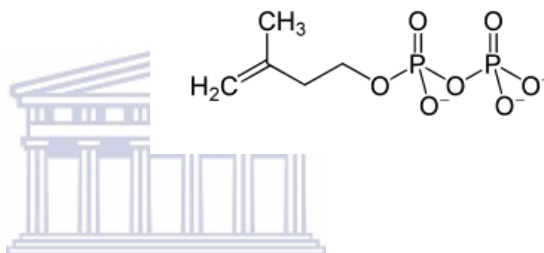
Alkaloids



Phenolic acids

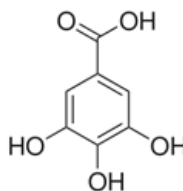


Terpenoids

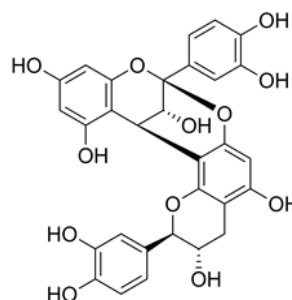


Phenolic acids

UNIVERSITY
WESTERN CA



Tannins



Chalcones

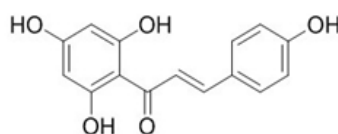


Figure 3.12: Possible biological entities in the plant extract responsible for the bioreduction of metal ions [143].

Table 3.5. List of different plants used for synthesis of ZnO nanoparticles.

Scientific name	Common name	Extract source	Precursor	Size (nm)	Shape	Reference
<i>Abrus precatorius</i>	Rosary pea	seeds	Zn(Ac)	90-500	Irregular to spherical	[144]
<i>Agathosma betulina</i>	Buchu	leaves	Zn(NO ₃) ₂	~19.4	Spherical	[145]
<i>Aloe barbadensis miller</i>	Aloe vera	leaves	Zn(NO ₃) ₂	25-40	Spherical	[146]
<i>Apalathus linearis</i>	Rooibos	flower	Zn(NO ₃) ₂	~12.5	Quasi-spherical	[147]
<i>Azadirachta indica</i>	Neem	leaves	Zn(NO ₃) ₂	~25	Nanotubes	[148]
<i>Azadirachta indica</i>	Neem	leaves	Zn(Ac)	9.6-25.5	Spherical	[149]
<i>Calotropis gigantea</i>	Crown flower	leaves	Zn(NO ₃) ₂	30-35	Spherical	[150]
<i>Calotropis procera</i>	Maddar	latex	Zn(Ac)	5-40	Spherical and granular	[151]
<i>Camellia sinensis</i>	Green tea	leaves	Zn(Ac)	~16	-	[152]
<i>Cassia auriculata</i>	Tanners cassia	flower	Zn(Ac)	-	Spherical	[153]
<i>Citrus aurantifolia</i>	Lime	fruit	Zn(NO ₃) ₂	9-10	Spherical	[154]
<i>Corymbia citriodora</i>	Lemon-scented Gum	leaves	Zn(NO ₃) ₂	~64	Hexagonal	[155]
<i>Euphorbia Jatropa</i>	-	latex	Zn(NO ₃) ₂	~15	Hexagonal	[156]

Table 3.5. -- Continued

Scientific name	Common name	Extract source	Precursor	Size (nm)	Shape	Reference
<i>Euphorbia milli</i>	Crown of thorns	latex	Zn(NO ₃) ₂	~50	Spherical	[157]
<i>Ocimum tenuiflorum</i>	Holy basil	leaves	Zn(NO ₃) ₂	11-25	Hexagonal	[158]
<i>Pongamia pinnata</i>	Indian beech	leaves	Zn(NO ₃) ₂	~100	Spherical	[159]
<i>Ruta graveolens</i>	Rue	stem	Zn(NO ₃) ₂	~28	Hexagonal, spherical	[160]
<i>Solanum nigrum</i>	Makoi/black night shade	leaves	Zn(NO ₃) ₂	~27.79	Quasi-spherical	[161]

A plant-mediated bioreduction involves the mixing of a plant with an aqueous solution of the relevant metal salt at room temperature. The bioreduction of the salt is visually observed by a change in the colour of the reaction mixture [114]. Paul, et al. [162] biosynthesized Zinc nanowires using *Spilanthes acmella* leaves. After mixing the leaf extract with a zinc sulphate solution, the colour change from pale yellow to pale brown was observed. Similarly to Ravindran, et al. [163], colour change was visually observed from colourless to pale yellow during the exposure of the Zn(NO₃)₂ solution with the plant extracts from different parts of the *Duranta erecta L.* plant (i.e. leaf, root, flower and fruit). On the other hand, Manokari, et al. [164] used aqueous extracts of leaf, stem, roots, flowers and fruits of *Melia azedarach* in the synthesis of ZnO nanoparticles. Colour change was observed after incubation for 6 hours at room temperature for the leaf extract mixture with Zn(NO₃)₂·6H₂O. For the other reaction mixtures, colour change was observed an hour after heating at 60 °C for 15 min.

The overall mechanism of the nanoparticle formation involves an initial activation phase. This is where the metal ions are reduced from their mono or divalent oxidation states to zero-valent states and heterogeneous nucleation of the reduced metal atoms occurs. This is

followed by a growth phase referred to as **Ostwald ripening**, the dissolution and redeposition of small contiguous particles on the surfaces of larger particles [165]. The termination phase is the final stage whereby the plant extracts ability to stabilize the metal nanoparticle acquires the most energetically favourable (more stable) conformation [105, 113]. Figure 3.13 shows the detailed schematic mechanism of nanoparticle formation.



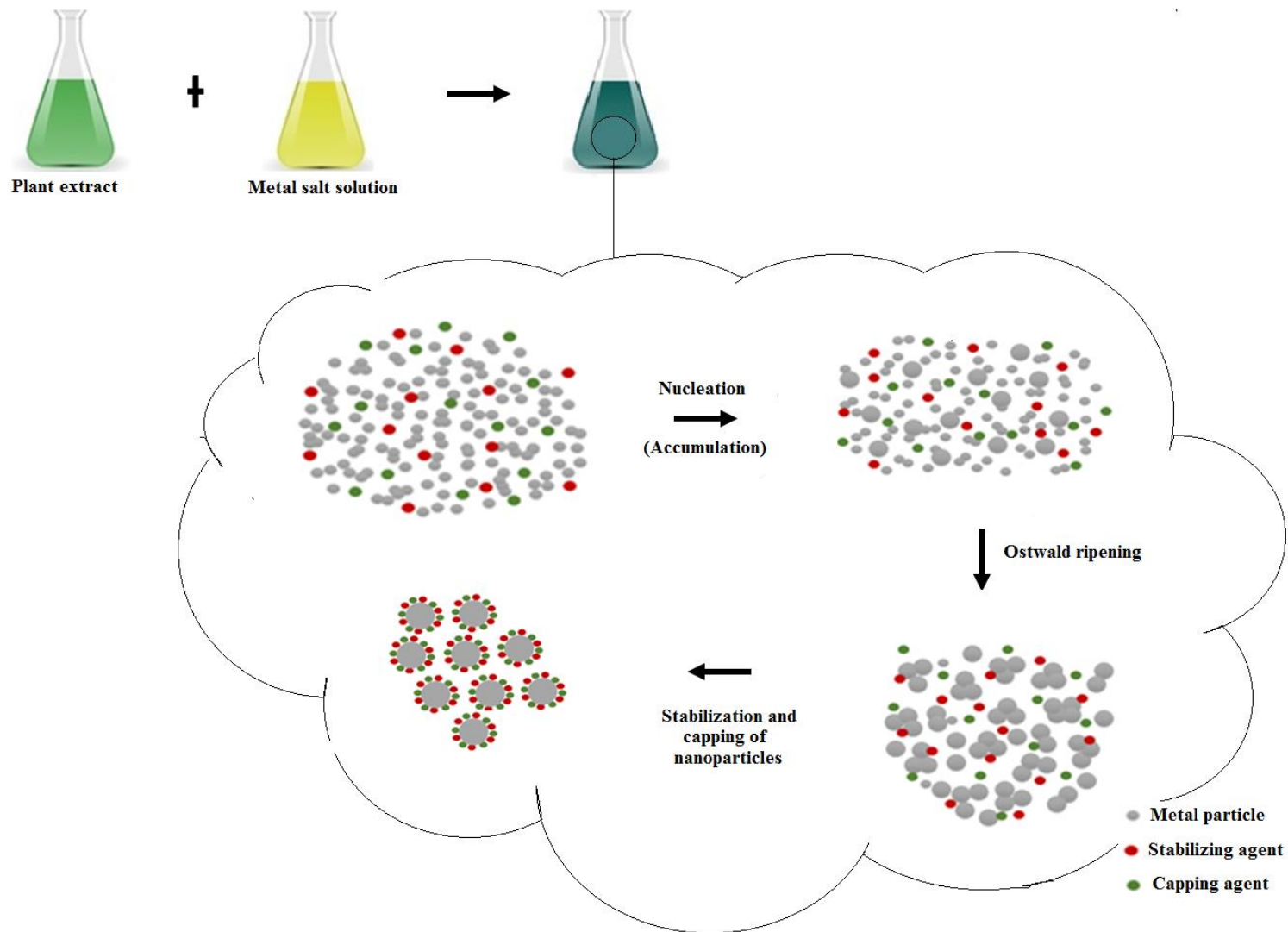


Figure 3.13: Mechanism of the nanoparticle formation using the plant extracts [113].

Advantages of using the green chemistry method [103, 154, 166, 167]:

- I. Easily scaled up for a large scale synthesis of nanoparticles
- II. Metal nanoparticles produced by plants are more stable
- III. Rate of synthesis is faster
- IV. Nanoparticles produced are more various in shape and in sizes : their sizes and morphologies can be controlled by varying some of the critical synthetic conditions such as the concentration of the metal salt, contact time, mixing ratio, pH and incubation temperature
- V. Cost effective: eliminates the use of expensive chemicals
- VI. No need to use high pressure, energy, or temperature
- VII. Minimizes environmental and human health risks by eliminating the use of harsh or toxic reagents during synthesis
- VIII. Biodegradable products and by-products (since they come from either plants or microorganisms)
- IX. Bio-compatible
- X. Results in high yield and more stable nanoparticles

Disadvantages associated with the green chemistry method [56, 103, 154, 166]:

- I. When using plants, the plant extract prepared from one species in various laboratories may lead to different results.
- II. Although rapidly being developed, biosynthesis of nanoparticles is still in its infancy.

3.4 References

- [1] V. Mody, R. Siwale, A. Singh and H. Mody, "Introduction to Metallic Nanoparticles," *Journal of Pharmacy & BioAllied Sciences*, vol. 2, no. 4, pp. 282-289, 2010.
- [2] S. Kulkarni, *Nanotechnology: Principles and Practices*, New Delhi: Capital Publishing Company, 2015.
- [3] "Techniques for synthesis of nanomaterials," [Online]. Available: https://www.ttu.ee/public/m/Mehaanikateaduskond/Instituudid/Materjalitehnika_instituut/MTX9100/Lecture11_Synthesis.pdf. [Accessed 26 May 2016].
- [4] E. Hu and D. Shaw, "Synthesis and Assembly," in *Nanostructure Science and Technology: R&D Status and Trends in Nanoparticles, Nanostructured Materials and Nanodevices*, R. Siegel, E. Hu and M. Roco, Eds., Netherlands, Springer-Science+Business Media, pp. 15-33, 1999.
- [5] A. Umer, S. Naveed and N. Ramzan, "Selection of a Suitable Method for the Synthesis of Copper Nanoparticles," *NANO: Brief Reports and Reviews*, vol. 7, no. 5, pp. 1-18, 2012.
- [6] "Physical Vapor Deposition," [Online]. Available: http://research.omicsgroup.org/index.php/Physical_vapor_deposition. [Accessed 26 May 2016].
- [7] S. Iravani, H. Korbekandi, S. Mirmohammadi and B. Zolfaghari, "Synthesis of Silver Nanoparticles: Chemical, Physical and Biological Methods," *Research in Pharmaceutical Sciences*, vol. 9, no. 6, pp. 385-406, 2014.
- [8] N. Rajput, "Methods of Preparation of Nanoparticles," *International Journal of Advances in Engineering & Technology*, vol. 7, no. 4, pp. 1806-1811, 2015.
- [9] W. Cao, "Synthesis of Nanomaterials by High Energy Ball Milling," [Online]. Available: <http://www.understandingnano.com/nanomaterial-synthesis-ball-milling.html>. [Accessed 12 May 2006].

- [10] A. Sengupta and C. Sarker, Eds., Introduction to Nano: Basics to Nanoscience and Nanotechnology, Berlin: Springer, 2015.
- [11] S. Amirkhanlou, M. Ketabchi and N. Parvin, "Nanocrystalline/nanoparticle ZnO synthesized by High Energy Ball," *Materials Letters*, vol. 86, no. 1, pp. 122–124, 2012.
- [12] N. Salah, S. Habib, Z. Khan, A. Memic, A. Azam, E. Alarfaj, N. Zahed and S. Al-Hamedi, "High-energy ball milling technique for ZnO Nanoparticles as Antibacterial Material," *International Journal of Nanomedicine*, vol. 6, no. 1, pp. 863-869, 2011.
- [13] A. Tavakoli, M. Sohrabi and A. Kargari, "A review of Methods for Synthesis of Nanostructured Metals with Emphasis on Iron Compounds," *Chemical Papers*, vol. 61, no. 3, pp. 151-170, 2007.
- [14] N. Rajput, "Methods of preparation of nanoparticles," *International Journal of Advances in Engineering & Technology*, vol. 7, no. 4, pp. 1806-1811, 2015.
- [15] "Physical Vapor Deposition," [Online]. Available: <https://www.sigmaaldrich.com/materials-science/material-science-products.html?TablePage=108832720>. [Accessed 26 May 2016].
- [16] D. Mattox, Handbook of Physical Vapor Deposition (PVD) processing, Toyko: Applied Science Publishers, 2010.
- [17] Z. Cui, Nanofabrication: Principles, Capabilities and Limits, Switzerland: Springer International Publishing, 2017.
- [18] C. Hu and J. Wen, "Iridium/Carbon Films Prepared by MOCVD," *Platinum Metals Rev.*, vol. 49, no. 2, pp. 70-76, 2005.
- [19] X. Wang, "Physical Vapor Deposition Technique for Growing Nanostructures," [Online]. Available: <http://www.nanoscience.gatech.edu/zlwang/research/pvd.html>. [Accessed 21 April 2016].
- [20] Z. Dai, Z. Pan and Z. Wang, "Novel nanostructures of functional oxides synthesized by thermal evaporation," *Advanced Functional Materials*, vol. 13, no. 1, pp. 9-22, 2003.

- [21] V. Pushkariov, A. Nikolaev and E. Kaidashev, "Synthesis and Characterization of ZnO Nanorods Obtained by Catalyst-free Thermal technique," *Journal of Physics*, vol. 541, no. 1, pp. 1-4, 2014.
- [22] Y. Xing, Z. Xi, X. Zhang, J. Song, R. Wang, J. Xu, Z. Xue and D. Yu, "Thermal evaporation synthesis of zinc oxide nanowires," *Applied Physics A*, vol. 80, no. 1, pp. 1527-1530, 2003.
- [23] S. Sakrani, P. Amin and S. Suhaimi, "Zinc oxide nanowires synthesized using a hot tube thermal evaporation under intermediate heating period," *Malaysian Journal of Fundamental and Applied Sciences*, vol. 9, no. 4, pp. 201-205, 2013.
- [24] Z.-G. Chen, F. Li, G. Liu, Y. Tang, H. Cong, G. Lu and H.-M. Cheng, "Preparation of high purity ZnO nanobelts by thermal evaporation of ZnS," *Journal of Nanosciences and Nanotechnology*, vol. 6, no. 1, pp. 704-707, 2006.
- [25] M. Nie, K. Sun and D. Meng, "Formation of metal nanoparticles by short-distance sputter deposition in a reactive ion etching chamber," *Journal of Applied Physics*, vol. 106, no. 1, pp. 1-5, 2009.
- [26] V. Ghafouri, M. Shariati and A. Ebrahimzad, "Photoluminescence investigation of crystalline undoped ZnO nanostructures constructed by RF sputtering," *Scientia Iranica*, vol. 19, no. 3, pp. 934-942, 2012.
- [27] J. Rashid, M. Barakat, N. Salah and S. Habib, "ZnO-nanoparticles thin films synthesized by RF sputtering for photocatalytic degradation of 2-chlorophenol in synthetic wastewater," *Journal of Industrial and Engineering Chemistry*, vol. 23, no. 1, pp. 134-139, 2014.
- [28] "Magnetron Sputtering Technology," [Online]. Available: <http://www.directvacuum.com/sputter.asp>. [Accessed 26 May 2016].
- [29] M. Hughes, "What Is Sputtering? Magnetron Sputtering?," [Online]. Available: <http://www.semicore.com/what-is-sputtering>. [Accessed 23 June 2016].
- [30] D. Pelleymounter, D. Christie and B. Fries, "Pulsed DC Power for Magnetron Sputtering:

Strategies for Maximizing Quality and Flexibility," in *Society of Vacuum Coaters* , Chicago, 2014.

- [31] "Radio Frequency Magnetron Sputtering," [Online]. Available: <http://surface.iphy.ac.cn/sf03/sputtering.htm>. [Accessed 21 September 2016].
- [32] "Sputtering Power Supply," [Online]. Available: <http://www.angstromsciences.com/sputtering-power-supply>. [Accessed 21 September 2016].
- [33] D. Depla, S. Mahieu and J. Greene, "Sputter deposition processes," in *Handbook of Deposition Technologies for Films and Coatings*, Washington, Elsevier, pp. 253-295, 2010.
- [34] M. Waite, S. Shah and D. Glocker, "Sputtering sources," in *50 Years of Vacuum Coating Technology and the growth of the Society of Vacuum Coaters*, D. Mattox and V. Mattox, Eds., Albuquerque, Society of Vacuum Coaters, pp. 42-50, 2007.
- [35] "Materials and Manufacturing: AC Sputtering," [Online]. Available: https://www.arl.psu.edu/mm_mp_ac_sputtering.php. [Accessed 21 September 2016].
- [36] "Sputter Deposition," [Online]. Available: https://en.wikipedia.org/wiki/Sputter_deposition. [Accessed 23 September 2016].
- [37] J. Plummer, M. Deal and P. Griffin, "Thin Film Deposition," in *Silicon VLSI Technology*, New Jersey, Prentice Hall, pp. 530-553, 2000.
- [38] B. Pamplin, Ed., *Molecular Beam Epitaxy*, Britain: Pergamon Press, 1980.
- [39] "Molecular Beam Epitaxy," [Online]. Available: https://en.wikipedia.org/wiki/Molecular_beam_epitaxy. [Accessed 30 June 2016].
- [40] M. Asghar, A. Ali, F. Iqbal, J. Merket, A. Gerges, M.-A. Hasan and M. Raja, "Synthesis and Analysis of ZnO Nanorods using Molecular Beam Epitaxy," in *NSTI-Nanotech*, Saudi Arabia, 2010.
- [41] H. Wang, C. Liao, Y. Chueh, C. Lai, L. Chen and R. Tsiang, "Synthesis and

characterization of Zn/ZnMgO multiple quantum wells by molecular beam epitaxy," *Optical Materials Express*, vol. 3, no. 2, pp. 237-247, 2013.

- [42] C. Woodford, "Molecular Beam Epitaxy," [Online]. Available: <http://www.explainthatstuff.com/molecular-beam-epitaxy-introduction.html>. [Accessed 22 April 2016].
- [43] C. Woodford, "Molecular Beam Epitaxy," [Online]. Available: <http://www.explainthatstuff.com/molecular-beam-epitaxy-introduction.html>. [Accessed 30 June 2016].
- [44] M. Yorulmaz, S. Yorulmaz and I. Yildiz, "Molecular Beam Epitaxy (MBE)," [Online]. Available: <https://www.google.co.za/url?sa=t&rct=j&q=&esrc=s&source=web&cd=1&ved=0ahUK EwjmvJvYiI3SAhXD1hQKHbMwA78QFggfMAA&url=http%3A%2F%2Fportal.ku.edu.tr%2F~myorulmaz%2Fcourse%2520presentations%2FMASE.%2520570%2520Molecular%2520Beam%2520Epitaxy.ppt&usg=AFQjCNFMnfO>. [Accessed 26 May 2016].
- [45] "Molecular Beam Epitaxy (MBE)," [Online]. Available: https://chemistry.osu.edu/~woodward/ch754/syn_mbe.htm. [Accessed 20 September 2016].
- [46] W. Cao, "Synthesis of Nanomaterials by Laser Ablation," [Online]. Available: <http://www.understandingnano.com/nanomaterial-synthesis-laser-ablation.html>. [Accessed 20 June 2016].
- [47] P. Wagener and S. Barcikowski, "Fabrication of nanoparticles and nanomaterials using laser ablation in liquids," *Photonik International*, vol. 1, no. 1, pp. 20-22, 2011.
- [48] "Laser Plume Ablation," [Online]. Available: <http://www.andor.com/learning-academy/laser-plume-ablation-an-overview-of-andor-s-solutions-for-lpa>. [Accessed 4 July 2016].
- [49] Y. Ishikawa, Y. Shimizu, T. Sasaki and N. Koshizaki, "Preparation of zinc oxide nanorods using pulsed laser ablation in water media at high temperature," *Journal of Colloidal and Interface Science*, vol. 300, no. 1, pp. 612-615, 2006.

- [50] H. Usui, Y. Shimizu, T. Sasaki and N. Koshizaki, "Photoluminescence of ZnO nanoparticles prepared by laser ablation in different surfactant solutions," *J. Phys. Chem*, vol. 109, no. 1, pp. 120-124, 2005.
- [51] S. Singh and R. Gopal, "Synthesis of colloidal zinc oxide nanoparticles by pulsed laser ablation in aqueous media," *Physica E*, vol. 40, no. 1, pp. 724-730, 2008.
- [52] "Laser Ablation," [Online]. Available: https://en.wikipedia.org/wiki/Laser_ablation. [Accessed 23 September 2016].
- [53] "Laser Ablation," [Online]. Available: <http://www.laserservicesusa.com/laser-ablation/>. [Accessed 23 September 2016].
- [54] "Laser Ablation Inductively Coupled Plasma Mass Spectrometry," [Online]. Available: <http://www.eag.com/laser-ablation-inductively-coupled-plasma-mass-spectrometry-la-icp-ms/>. [Accessed 23 September 2016].
- [55] "Wet Chemical Methods," [Online]. Available: <http://eng.thesaurus.rusnano.com/wiki/article1209>. [Accessed 25 July 2016].
- [56] S. Iravani, H. Korbekandi, S. Mirmohammadi and B. Zolfaghari, "Synthesis of silver nanoparticles: chemical, physical and biological methods," *Research in Pharmaceutical Sciences*, vol. 9, no. 1, pp. 385-406, 2014.
- [57] "Solgel Part 1," YouTube, [Online]. Available: https://www.youtube.com/watch?v=VIWGIKCV_6k. [Accessed 26 July 2016].
- [58] C. Brinker and G. Scherer, "Sol-Gel Science: The Physics and Chemistry of Sol-Gel Processing," Academic Press, London, 1990.
- [59] A. Mohamad and S. Alias, "ZnO Nanocrystalline Metal Oxide Semiconductor Via Sol Gel Method," in *Synthesis of Zinc Oxide by Sol-Gel Method for Photoelectrochemical Cells*, Tebal, SpringerBriefs in Materials, pp. 4-7, 2014.
- [60] C. Aydın, A. Omar A. Al-Hartomy, A. Al-Ghamdi, F. Al-Hazmi, I. Yahia, F. El-Tantawy and F. Yakuphanoglu, "Controlling of crystal size and optical band gap of CdO nanopowder semiconductors by low and high Fe contents," *Electroceramics*, vol. 29, no.

2, pp. 155-162, 2012.

- [61] K. Foo, U. Hashim, K. Muhammad and C. Voon, "Sol-gel synthesized zinc oxide nanorods and their structural and optical investigation for optoelectronic application," *Nanoscale Research Letters*, vol. 9, no. 1, pp. 1-10, 2014.
- [62] J. Hasnidawani, H. Azlina, H. Norita, N. Bonnia, S. Ratim and E. Ali, "Synthesis of ZnO nanostructures using sol-gel method," *Procedia Chemistry*, vol. 19, no. 1, pp. 211-216, 2016.
- [63] S. Jurablu, M. Farahmandjou and T. Firoozabadi, "Sol-gel synthesis of Zinc oxide (ZnO) nanoparticles: study of structural and optical properties," *Journal of Sciences*, vol. 26, no. 3, pp. 281-285, 2015.
- [64] M. Khan, A. Ansari, M. Hameedullah, E. Ahmas, F. Husain, Q. Zia, U. Baig, M. Zaheer, M. Alam, A. Khan, Z. AlOthman, I. Ahmad, G. Ashraf and G. Aliev, "Sol-gel synthesis of thorn-like ZnO nanoparticles endorsing mechanical stirring effect and their antimicrobial activities: potential role as nano-antibiotics," *Scientific reports*, vol. 6, no. 1, pp. 1-32, 2016.
- [65] "What is sol-gel processing?," [Online]. Available: <http://www.twi-global.com/technical-knowledge/faqs/process-faqs/faq-what-is-sol-gel-processing/>. [Accessed 27 July 2016].
- [66] C. Carter and M. Norton, "Sols, Gels, and Organic Chemistry," in *Ceramic Materials*, New York, Springer, pp. 400-411, 2007.
- [67] H. Hayashi and Y. Hakuta, "Hydrothermal Synthesis of Metal Oxide Nanoparticles in Supercritical Water," *Materials*, vol. 3, no. 1, pp. 3794-3817, 2010.
- [68] M. Yoshimura and K. Byrappa, "Hydrothermal processing of materials: past, present and future," *Journal of Materials Science*, vol. 43, no. 1, pp. 2085-2103, 2008.
- [69] "Hydrothermal synthesis," [Online]. Available: https://en.wikipedia.org/wiki/Hydrothermal_synthesis. [Accessed 17 May 2016].
- [70] P. Aneesh, K. Vanaja and M. Jayaraj, "Synthesis of ZnO nanoparticles by hydrothermal

method," in *Nanophotonic Materials*, California, 2007.

- [71] A. Reddy, A. Mallika, K. Babu and K. Reddy, "Hydrothermal Synthesis and Characterization of ZnO Nano Crystals," *International Journal of Mining, Metallurgy & Mechanical Engineering*, vol. 3, no. 2, p. 2320–4060, 2015.
- [72] K. Sun, W. Wei, Y. Ding, Y. Jing, Z. Wang and D. Wang, "Crystalline ZnO thin film by hydrothermal growth," *Chem. Comm*, vol. 47, no. 1, pp. 7776-7778, 2011.
- [73] "Solvothermal synthesis," [Online]. Available: https://en.wikipedia.org/wiki/Solvothermal_synthesis. [Accessed 18 May 2016].
- [74] "Hydrothermal synthesis," [Online]. Available: <http://eng.thesaurus.rusnano.com/wiki/article729>. [Accessed 26 August 2016].
- [75] N. Asim, S. Ahmadi, M. Alghoul, F. Hammadi, K. Saeedfar and K. Sopian, "Research and Development Aspects on Chemical Preparation Techniques of Photoanodes for Dye Sensitized Solar Cells," *International Journal of Photoenergy*, vol. 2014, no. 1, pp. 1-17, 2014.
- [76] A. Askarinejad, M. Alavi and A. Morsali, "Sonochemically Assisted Synthesis of ZnO Nanoparticles: A Novel Direct Method," *Iran. J. Chem*, vol. 30, no. 3, pp. 75-81, 2011.
- [77] R. Yadav, P. Mishra and A. Pandey, "Growth mechanism and optical property of ZnO nanoparticles synthesized by sonochemical method," *Ultrasonics Sonochemistry*, vol. 15, no. 1, pp. 863-868, 2008.
- [78] "Sonochemical Synthesis of Cobalt Ferrite Nanoparticles," [Online]. Available: <https://www.hindawi.com/journals/ijce/2013/934234/>. [Accessed 20 May 2016].
- [79] S. Kiel, O. Grinberg, N. Perkas, J. Charmet, H. Kepner and A. Gedanken, "Forming nanoparticles of water-soluble ionic molecules and embedding them into polymer and glass substrates," *Beilstein Journal of Nanotechnology*, vol. 3, no. 1, pp. 267–276, 2012.
- [80] Y. Mastai and A. Gedanken, "Sonochemistry and Other Novel Methods Developed for the Synthesis of Nanoparticles," in *The Chemistry of Nanomaterials: Synthesis, Properties*

and Applications, Weinheim, Wiley-VCH, pp. 113-164, 2004.

- [81] J. Dean and N. Saim, "Modern alternatives to supercritical fluid extraction," in *Analytical supercritical fluid extraction techniques*, Pontypridd, Springer, pp. 393, 1998.
- [82] B. Hayes, "Microwave synthesis: Chemistry at the speed of light," CEM publishing, North Carolina, 2002.
- [83] "Microwave synthesis," [Online]. Available: <http://www.organic-chemistry.org/topics/microwave-synthesis.shtm>. [Accessed 26 February 2016].
- [84] "Microwave-assited synthesis," [Online]. Available: <http://wiki.anton-paar.com/microwave-assisted-synthesis/>. [Accessed 16 October 2016].
- [85] M. Hasanpoor, M. Aliofkhazraei and H. Delavari, "Microwave-assisted Synthesis of Zinc Oxide Nanoparticles," *Procedia Materials Science*, vol. 11, no. 1, pp. 320-325, 2015.
- [86] G. Barreto, G. Morales, A. Canizo and N. Eyler, "Microwave assisted synthesis of ZnO tridimensional nanostructures," *Procedia Materials Science*, vol. 8, no. 1, pp. 535-540, 2015.
- [87] N. Shojaee, T. Ebadzadeh and A. Aghaei, "Microwave assisted hydrothermal synthesise of ZnO nanorods and their characterization," in *International Journal of Modern Physics: Conference series*, Moscow, 2012.
- [88] L. Favretto, "Basic Guidelines for Microwave Organic Chemistry Applications," [Online]. Available: <http://research.uni-leipzig.de/giannis/Lehre/OCF/Basic%20Guidelines%20for%20Microwave%20Reactor%20and%20Reactions.pdf>. [Accessed 12 September 2016].
- [89] "Would You Benefit From Microwave-Assisted Organic Synthesis in Your Lab?," [Online]. Available: <http://www.americanlaboratory.com/Lab-Tips/157805-LabTips-Would-You-Benefit-From-Microwave-Assisted-Organic-Synthesis-in-Your-Lab/>. [Accessed 12 September 2016].
- [90] B. Das and D. C. S. Bhowmik, "Microwave System," *The Pharma Innovation*, vol. 1, no.

6, pp. 1-15, 2012.

- [91] "Microwave synthesis," [Online]. Available: <http://www.organic-chemistry.org/topics/microwave-synthesis.shtm>. [Accessed 19 September 2016].
- [92] "Chemical Vapour Deposition - An Introduction," [Online]. Available: <http://www.azom.com/article.aspx?ArticleID=1552>. [Accessed 16 February 2016].
- [93] J. Creighton and P. Ho, "Introduction to Chemical Vapor Deposition (CVD)," ASM International, Albuquerque, 2001.
- [94] [Online]. Available: https://en.wikipedia.org/wiki/Chemical_vapor_deposition. [Accessed 15 September 2016].
- [95] "DLC Coatings in Oil and Gas Production," [Online]. Available: <http://www.slideshare.net/TomaszLiskiewicz/dlc-coatings-in-oil-and-gas-production>. [Accessed 15 February 2016].
- [96] Y. Guan and A. Pedraza, "Synthesis and alignment of Zn and ZnO nanoparticles by laser-assisted chemical vapor deposition," *IOP Publishing*, vol. 19, no. 1, pp. 1-7, 2008.
- [97] S. Polarz, A. Roy, M. Merz, S. Halm, D. Schröder, L. Schneider, G. Bacher, F. Kruis and M. Driess, "Chemical Vapor Synthesis of Size-Selected Zinc Oxide Nanoparticles," *Small*, vol. 5, no. 1, p. 540–552, 2005.
- [98] "Chemical Vapor Deposition vs Physical Vapor Deposition," [Online]. Available: documents.indium.com/qdynamo/download.php?docid=1957. [Accessed 20 September 2016].
- [99] "Chemical Vapor Deposition," [Online]. Available: <http://archive.cnx.org/contents/9bbb39c-a840-4461-882c-e31f8a0125e6@2/chemical-vapor-deposition>. [Accessed 12 August 2016].
- [100] "Basics of Green Chemistry," [Online]. Available: <https://www.epa.gov/greenchemistry/basics-green-chemistry>. [Accessed 03 October 2016].

- [101] "The Twelve Principles of Green Chemistry: What it is, & Why it Matters," [Online]. Available: <http://www.compoundchem.com/2015/09/24/green-chemistry/>. [Accessed 03 October 2016].
- [102] J. Linthorst, "An overview: origins and development of green chemistry," *Foundations of Chemistry*, vol. 12, no. 1, pp. 55-68, 2010.
- [103] M. Ali, M. Arfan and A. Shahverdi, "Role of Natural Products in Green Synthesis of Nanoparticles," in *Green Biosynthesis of Nanoparticles: Mechanisms and Applications*, London, Berforts Information Press Ltd, pp. 31-52, 2013.
- [104] S. Iravani, "Green synthesis of metal nanoparticles using plants," *Green Chemistry*, vol. 13, no. 1, pp. 2638-2650, 2011.
- [105] V. Makarov, A. Love, O. Sinitsyna, S. Makarova, I. Yaminsky, M. Taliany and N. Kalinina, "Green Nanotechnologies: Synthesis of Metal Nanoparticles Using Plants," *Acta Naturae*, vol. 6, no. 1, pp. 35-44, 2014.
- [106] M. Rai and A. Yadav, "Plants as potential synthesiser of precious metal nanoparticles: progress and prospects," *IET Nanobiotechnology*, vol. 7, no. 3, pp. 117-124, 2013.
- [107] I. Siavash, "Bacteria in Nanoparticle Synthesis: Current Status and Future Prospects," *Hindawi Publishing Corporation*, vol. 2014, no. 1, pp. 1-18, 2014.
- [108] A. Chokriwal, M. Mohan Sharma and A. Singh, "Biological Synthesis of Nanoparticles Using Bacteria and Their Applications," *American Journal of Pharmatech Research*, vol. 4, no. 6, pp. 38-61, 2014.
- [109] K. Flint, "Viral Nanoparticles: A cure for cancer?," *Dartmouth Undergraduate Journal of Science*, vol. 9, no. 1, pp. 6-7, 2011.
- [110] N. Steinmetz, "Viral Nanoparticles in Drug Delivery and Imaging," *ACS Publications*, vol. 10, no. 1, pp. 1-2, 2013.
- [111] B. Moghaddam, F. Namvar, M. Moniri, P. Tahir and S. Azizi, "Nanoparticles Biosynthesized by Fungi and Yeast: A Review of Their Preparation, Properties, and

- Medical Applications," *Molecules*, vol. 20, no. 1, pp. 16540-16565, 2015.
- [112] K. Siddiqi and A. Husen, "Fabrication of Metal Nanoparticles from Fungi and Metal Salts: Scope and Application," *Nanoscale Research Letters*, vol. 11, no. 1, pp. 1-15, 2016.
- [113] M. Shah, D. Fawcett, S. Sharma, S. Tripathy and G. Poinern, "Green Synthesis of Metallic Nanoparticles via Biological Entities," *Materials*, vol. 8, no. 1, pp. 7278-7308, 2015.
- [114] A. Mittal, Y. Chisti and U. Banerjee, "Synthesis of metallic nanoparticles using plant extracts," *Biotechnology Advances*, vol. 31, no. 2, pp. 346-356, 2013.
- [115] P. Logeswari, S. Silambarasan and J. Abraham, "Ecofriendly synthesis of silver nanoparticles from commercially available plant powders and their antibacterial properties," *Scientia Iranica F*, vol. 20, no. 3, pp. 1049-1054, 2013.
- [116] R. Haverkamp and A. Marshall, "The mechanism of metal nanoparticle formation in plants: limits on accumulation," *J Nanopart Res*, vol. 11, no. 1, pp. 1453-1463, 2009.
- [117] "Hyperaccumulator," [Online]. Available: <https://en.wikipedia.org/wiki/Hyperaccumulator>. [Accessed 27 September 2016].
- [118] "List of hyperaccumulators," [Online]. Available: http://en.wikipedia.org/wiki/List_of_hyperaccumulators. [Accessed 12 October 2016].
- [119] B. Ankamwar, "Size and Shape Effect on Biomedical Applications of Nanomaterials," in *Biomedical Engineering-Technical Applications in Medicine*, Croatia, Intech, pp. 93-114, 2012.
- [120] P. Malik, R. Shankar, V. Malik, N. Sharma and T. Mukherjee, "Green Chemistry Based Benign Routes for Nanoparticle Synthesis," *Journal of Nanoparticles*, vol. 2014, no. 1, pp. 1-14, 2014.
- [121] P. Kuppusamy, M. Yusoff, G. Maniam and N. Govindan, "Biosynthesis of metallic nanoparticles using plant derivatives and their new avenues in pharmacological applications - An updated report," *Saudi Pharmaceutical Journal*, vol. 24, no. 1, pp. 473-

484, 2016.

- [122] M. Noruzi, "Biosynthesis of gold nanoparticles using plant extracts," *Bioprocess Biosyst Eng*, vol. 38, no. 1, pp. 1-14, 2015.
- [123] "12 Principles of Green Chemistry," [Online]. Available: <http://www.slideshare.net/NoraIsmagilova/green-chemistry-principles>. [Accessed 30 September 2016].
- [124] C. Jayaseelan, A. Abdul Rahuman, A. Vishnu Kirthi, S. Marimuthu, T. Santhoshkumar, A. Bagavan, K. Gaurav, L. Karthik and K. Bhaskara Rao, "Novel microbial route to synthesize ZnO nanoparticles using *Aeromonas hydrophila* and their activity against pathogenic bacteria and fungi," *Spectrochimica Acta Part A: Molecular and Biomolecular Spectroscopy*, vol. 90, no. 1, pp. 78-84, 2012.
- [125] N. Pugazhenthiran, S. Anandan, G. Kathiravan, N. Kannaian, U. Prakash, S. Crawford and M. Ashokkumar, "Microbial synthesis of silver nanoparticles by *Bacillus* sp.," *Journal of Nanoparticle Research*, vol. 11, no. 1, pp. 1811-1815, 2009.
- [126] E. Selvarajan and V. Mohanasrinivasan, "Biosynthesis and characterization of ZnO nanoparticles using *Lactobacillus plantarum* VITES07," *Materials Letters*, vol. 112, no. 1, pp. 180-182, 2013.
- [127] S. He, Z. Guo, Y. Zhang, S. Zhang, J. Wang and N. Gu, "Biosynthesis of gold nanoparticles using the bacteria *Rhodospseudomonas capsulata*," *Materials Letters*, vol. 61, no. 18, p. 3984–3987, 2007.
- [128] G. Li, D. He, Y. Qian, B. Guan, S. Gao, Y. Cui, K. Yokoyama and L. Wang, "Fungus-Mediated Green Synthesis of Silver Nanoparticles Using *Aspergillus terreus*," *International Journal of Molecular Sciences*, vol. 13, no. 1, pp. 466-476, 2012.
- [129] A. Syed, S. Saraswati, A. Ahmad and G. Kundu, "Biological synthesis of silver nanoparticles using the fungus *Humicola* sp. and evaluation of their cytotoxicity using normal and cancer cell lines," *Spectrochimica Acta Part A: Molecular and Biomolecular Spectroscopy*, vol. 114, no. 1, pp. 144-174, 2013.

- [130] T. Pavani, K. Rao, C. Chakra and Y. Prabhu, " Microbial Synthesis of ZnO nanoparticles by Yeast: *Sacchromyces cerevisiae*," *Journal of Nanoscience, Nanoengineering and Applications.*, vol. 5, no. 2, pp. 1-5, 2015.
- [131] K. Narayanan and S. N., "Facile green synthesis of gold nanostructures by NADPH-dependent enzyme from the extract of *Sclerotium rolfsii*," *Colloids and Surfaces A: Physicochemical and Engineering Aspects*, vol. 380, no. 1, p. 156–161, 2011.
- [132] I. Maliszewska, Ł. Aniszkiewicz and Z. Sadowski, "Biological Synthesis of Gold Nanostructures Using the Extract of *Trichoderma koningii*," *ACTA PHYSICA POLONICA A*, vol. 116, no. 1, pp. 163-165, 2009.
- [133] A. Love, V. Makarov, O. Sinitsyna, J. Shaw, I. Yaminsky, N. Kalinina and M. Taliany, "A Genetically Modified Tobacco Mosaic Virus that can Produce Gold Nanoparticles from a Metal Salt Precursor," *Frontiers in Plant Science*, vol. 6, no. 1, pp. 1-10, 2015.
- [134] L. Vera-Robles, L. Escobar-Alarcon, M. Picquart, J. Hernandez-Pozos and E. Haro-Poniatowski, "A Biological Approach for the Synthesis of Bismuth Nanoparticles: Using Thiolated M13 Phage as Scaffold," *Langmuir*, vol. 32, no. 1, pp. 3199–3206, 2016.
- [135] M. Zaman and E. Haberer, "M13 Bacteriophage-Assisted Biomineralization of Copper Sulfide," *Materials Research Society*, vol. 1445, no. 1, pp. 1-3, 2012.
- [136] S. Ahmed, Saifullah, M. Ahmad, B. Swami and S. Ikram, "Green synthesis of silver nanoparticles using *Azadirachta indica* aqueous leaf extract," *Journal of Radiation Research and Applied Sciences* , vol. 9, no. 1, pp. 1-7, 2016.
- [137] F. Thema, P. Beukes, A. Gurib-Fakim and M. Maaza, "Green synthesis of Monteponite CdO nanoparticles by *Agathosma betulina* natural extract," *Journal of Alloys and Compounds*, vol. 646, no. 1, pp. 1043-1048, 2015.
- [138] B. Sone, E. Manikandan, A. Gurib-Fakim and M. Maaza, "Sm₂O₃ nanoparticles green synthesis via *Callistemon viminalis*' extract," *Journal of Alloys and Compounds*, vol. 650, no. 1, pp. 357-362, 2015.
- [139] R. Pasca, A. Mocanu, S. Cobzac, I. Petean, O. Horovitz and M. Tomoaia-Cotisel,

"Biogenic Syntheses of Gold Nanoparticles Using Plant Extracts," *Particulate Science and Technology*, vol. 32, no. 2, pp. 131-137, 2014.

- [140] N. Thovhogi, E. Park, E. Manikandan, M. Maaza and A. Gurib-Fakim, "Physical properties of CdO nanoparticles synthesized by green chemistry via Hibiscus Sabdariffa flower extract," *Journal of Alloys and Compounds*, vol. 655, no. 1, pp. 314-320, 2015.
- [141] B. Bhau, S. Ghosh, S. Puri, B. Borah, D. Sarmah and R. Khan, "Green synthesis of gold nanoparticles from the leaf extract of *Nepenthes khasiana* and antimicrobial assay," *Advanced Materials Letters*, vol. 6, no. 1, pp. 55-58, 2015.
- [142] D. Bose and S. Chatterjee, "Biogenic synthesis of silver nanoparticles using guava (*Psidium guajava*) leaf extract and its antibacterial activity against *Pseudomonas aeruginosa*," *Applied Nanoscience*, vol. 6, no. 6, p. 895-901, 2015.
- [143] M. de Lourdes Reis Giada, "Food Phenolic Compounds: Main Classes, Sources and Their Antioxidant Power," in *Oxidative Stress and Chronic Degenerative Diseases - A role for Antioxidants*, Croatia, Intech, pp. 87-112, 2013.
- [144] K. Vishwakarma, "Green synthesis of ZnO nanoparticles using *Abrus precatorius* seeds extract and their characterization," National Institute of Technology, Rourkela, 2013.
- [145] F. Thema, E. Manikandan, M. Dhlamini and M. Maaza, "Green synthesis of ZnO nanoparticles via *Agathosma betulina* natural extract," *Materials Letters*, vol. 161, no. 1, pp. 124-127, 2015.
- [146] G. Sangeetha, S. Rajeshwari and R. Venckatesh, "Green synthesis of zinc oxide nanoparticles by *aloe barbadensis miller* leaf extract: Structure and optical properties," *Materials Research Bulletin*, vol. 46, no. 1, pp. 2560-2566, 2011.
- [147] A. Diallo, B. Ngom, E. Park and M. Maaza, "Green synthesis of ZnO nanoparticles by *Aspalathus Linearis*: Structural and optical properties," *Journal of Alloys and Compounds*, vol. 646, no. 1, pp. 425-430, 2015.
- [148] A. Oudhia, P. Kulkarni and S. Sharma, "Green synthesis of ZnO nanotubes for bioapplications," *International Journal of Advanced Engineering Research and Studies*,

vol. 6, no. 2, pp. 280-281, 2015.

- [149] T. Bhuyan, K. Mishra, M. Khanuja, R. Prasad and A. Varma, "Biosynthesis of zinc oxide nanoparticles from *Azadirachta indica* for antibacterial and photocatalytic applications," *Materials Science in Semiconductor Processing*, vol. 32, no. 1, pp. 55-61, 2015.
- [150] C. Vidya, S. Hiremath, M. Chandraprabha, M. Antonyraj, I. Gopal, A. Jain and K. Bansal, "Green synthesis of ZnO nanoparticles by *Calotropis Gigantea*," in *International Journal of Current Engineering and Technology*, Dharwad, 2013.
- [151] R. Singh, R. Yadav, P. Sharma, P. Singh, A. Pandey and V. Shukla, "Biological approach of zinc oxide nanoparticles formation and its characterization," *Advanced Materials Letters*, vol. 2, no. 4, pp. 313-317, 2011.
- [152] S. Senthilkumar and T. Sivakumar, "Green tea (*Camellia sinensis*) mediated synthesis of zinc oxide (ZnO) nanoparticles and studies on their antimicrobial activities," *International Journal of Pharmacy and Pharmaceutical Sciences*, vol. 6, no. 6, pp. 461-465, 2014.
- [153] P. Ramesh, A. Rajendran and M. Meenakshisundaram, "Green synthesis of Zinc Oxide Nanoparticles Using Flower Extract *Cassia Auriculata*," *Journal of NanoScience and NanoTechnology*, vol. 2, no. 1, pp. 41-45, 2014.
- [154] P. Ramesh, A. Rajendran and A. Subramanian, "Synthesis of Zinc Oxide Nanoparticles from Fruit of *Citrus Aurantifolia* by Chemical and Green Method," *Asian Journal of Phytomedicine and Clinical Research*, vol. 2, no. 1, pp. 189-195, 2014.
- [155] Y. Zheng, L. Fu, F. Han, A. Wang, W. Cai, J. Yu, J. Yang and F. Peng, "Green biosynthesis and characterization of zinc oxide nanoparticles using *Corymbia citriodora* leaf extract and their photocatalytic activity," *Green Chemistry Letters and Reviews*, vol. 8, no. 2, pp. 59-63, 2015.
- [156] M. Geetha, H. Nagabhushana and H. Shivananjaiah, "Green mediated synthesis and characterization of ZnO nanoparticles using *Euphorbia Jatropa* latex as reducing agent," *Journal of Science: Advanced Materials and Devices*, vol. 1, no. 3, pp. 301-310, 2016.
- [157] M. Geetha, H. Nagabhushana and H. Shivananjaiah, "Green Mediated Synthesis and

- Characterization of ZnO Using Euphorbia Milli Latex as Fuel," *International Journal of Science and Research*, vol. 5, no. 4, pp. 158-163, 2016.
- [158] S. Raut, P. Thorat and R. Thakre, "Green Synthesis of Zinc Oxide (ZnO) Nanoparticles Using Ocimum Tenuiflorum Leaves," *International Journal of Science and Research (IJSR)*, vol. 4, no. 5, pp. 1224-1228, 2013.
- [159] S. Ambika and M. Sundrarajan, "Plant-extract mediated synthesis of ZnO nanoparticles using Pongamia pinnata and their activity against pathogenic bacteria," *Advanced Powder Technology*, vol. 26, no. 5, pp. 1-6, 2015.
- [160] K. Lingaraju, H. Naika, K. Manjunath, R. Basavaraj, H. Nagabhushana, G. Nagaraju and D. Suresh, "Biogenic synthesis of zinc oxide nanoparticles using Ruta graveolens (L.) and their antibacterial and antioxidant activities," *Applied Nanoscience*, vol. 6, no. 1, pp. 703-710, 2016.
- [161] M. Ramesh, M. Anbuvaran and G. Viruthagiri, "Green synthesis of ZnO nanoparticles using Solanum nigrum leaf extract and their antibacterial activity," *Spectrochimia Acta Part A: Molecular and Niomolecular Spectroscopy*, vol. 136, no. 1, pp. 864-870, 2014.
- [162] N. Paul, E. Khole, S. Jagtap, H. Tribhuvan, G. Kakde and P. Kuwar, "Green Synthesis of Zinc Nanowires using Spinlanthes acmella Leaf Extract," *UK Journal of Pharmaceutical and Biosciences*, vol. 4, no. 3, pp. 45-47, 2016.
- [163] C. Ravindran, M. Manokari and M. Shekhawat, "Biogenic production of zinc oxide nanoparticles from aqueous extracts of Duranta erecta L.," *World Scientific News*, vol. 28, no. 1, pp. 30-40, 2016.
- [164] M. Manokari, C. Ravindran and M. Shekhawat, "Biosynthesis of Zinc Oxide Nanoparticles using Melia azedarach L. extracts and their characterization," *International Journal of Pharmaceutical Science and Research*, vol. 1, no. 1, pp. 31-36, 2016.
- [165] "Ostwald ripening," [Online]. Available: https://en.wikipedia.org/wiki/Ostwald_ripening. [Accessed 12 October 2016].
- [166] A. Umer, S. Naveed and N. Ramzan, "Selection of a Suitable Method for the Synthesis of

Copper Nanoparticles," *World Scientific*, vol. 7, no. 1, pp. 1-18, 2012.

- [167] S. Iravani, H. Korbekandi, S. Mirmohammadi and B. Zolfaghari, "Synthesis of Silver Nanoparticles: Chemical, Physical and Biological Methods," *Research in Pharmaceutical Sciences*, vol. 9, no. 1, pp. 385-406, 2014.



Chapter 4: Material and characterization techniques

The study of ZnO in its nanoscale requires accurate and well understood techniques. This chapter gives a detailed description on the synthesis of ZnO nanoparticles and also, a brief description of the techniques that have been utilized in this study as well as their respective sample preparations.

4.1 Material preparation

Twenty grams (20 g) of high quality dried *Aspalathus linearis*' needle-like leaves (shown in Figure 4.1) were weighed and cleaned thoroughly with cold deionised water. Following a drying phase under sunny conditions at ambient temperature, the sample was ground into a fine powder. The powder was then immersed in 400 ml of de-ionised water for 12 hours to ensure the maximum extraction of the brown dye. The dye extract solution (pH 6) was then filtered twice using Whatman filters to eliminate any residual solids. Zinc acetate dihydrate $\text{Zn}(\text{C}_4\text{H}_6\text{O}_4) \cdot 2\text{H}_2\text{O}$ from Sigma-Aldrich was used as Zinc precursor. The $\text{Zn}(\text{C}_4\text{H}_6\text{O}_4) \cdot \text{H}_2\text{O}$ was of analytical grade, hence used without any further purification. 20 g of zinc acetate was dissolved in 45 ml of de-ionised water. The salt solution was then homogeneously mixed with 200 ml of *Aspalathus Linearis* extract solution.



Figure 4.1: The *Aspalathus Linearis* needle-like leaves that were used in the green synthesis of ZnO nanoparticles.

An immediate colour change from reddish-brown to muddy brown was observed. This visible observation is shown in Figure 4.2. The mixture was heated in a capped bottle for 4 hours at ~80 °C. Following such a phase, dark precipitate were observed. The precipitate was separated from the aqueous extract by centrifuging using a Lasec Sigma unit at 1000 rpm for

10 minutes over successive additions of deionized water to wash the precipitate of any residual aqueous extract.

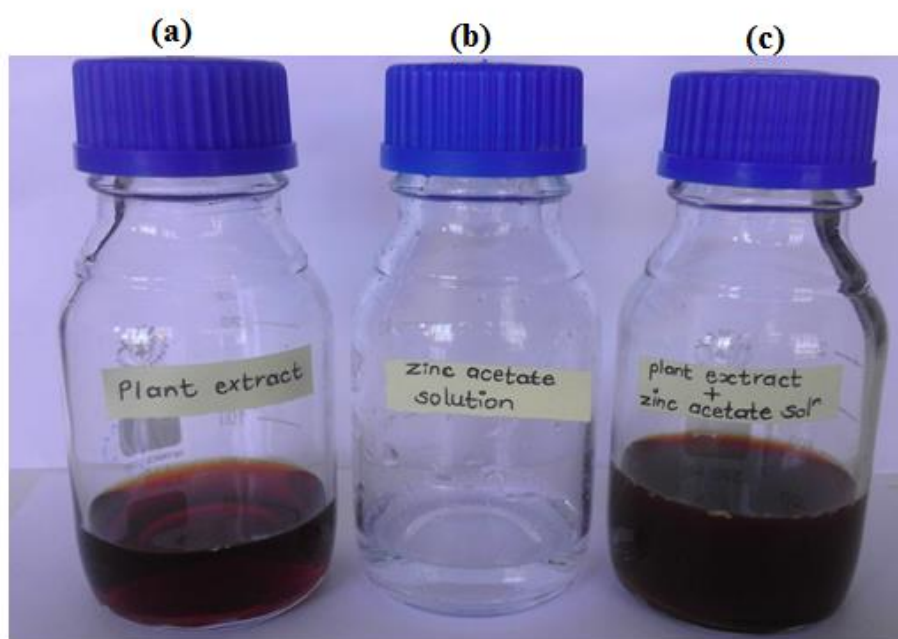


Figure 4.2: The (a) dye extracted from the *Aspalathus Linearis*'s leaves, (b) zinc acetate solution, and (c) mixture of the *Aspalathus Linearis* leaves and the zinc acetate solution.

The resultant precipitate obtained was dried in an oven at 100 °C. After drying, the precipitate samples were then annealed in an open furnace from 300 °C to 600 °C in 100 °C increments for 2 hours. The heat treatment of 300 °C was necessary in order to induce the formation of high crystalline ZnO nanoparticles. Figure 4.3 shows the powders obtained before and after the annealing treatment.

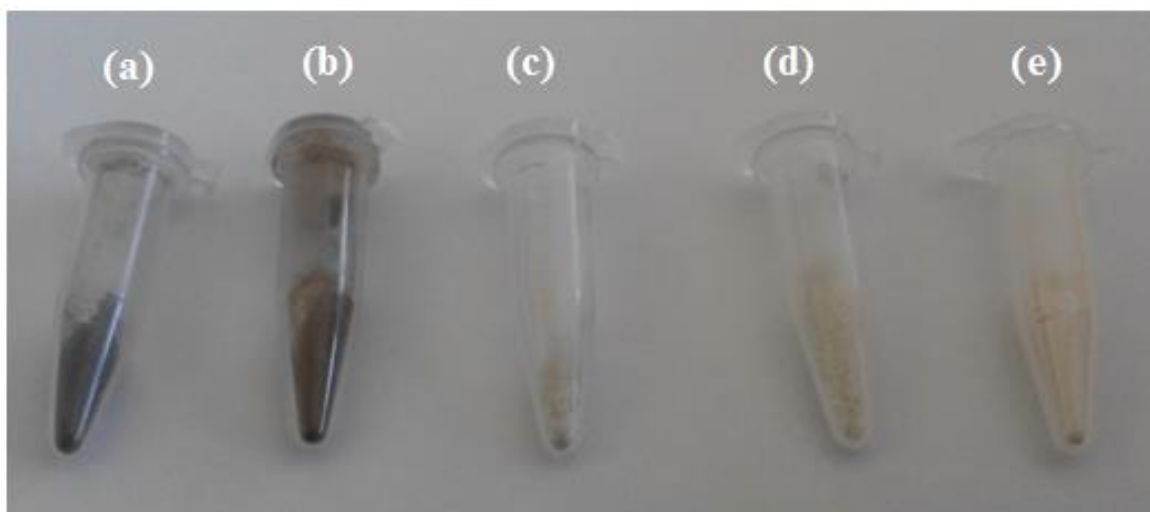


Figure 4.3: ZnO powder (a) as-prepared and annealed at (b) 300 °C, (c) 400 °C, (d) 500 °C & (e) 600 °C.

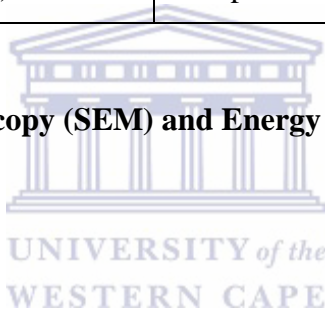
4.2 Material characterization

The physical properties of the obtained ZnO powders were investigated by the different characterization techniques summarized in Table 4.1. For size and structure determination, a Carl Zeiss Auriga Field Emission Scanning Electron Microscope (FEG SEM) operated at beam energy of 20 keV was used. An Oxford instruments X-Max solid state Silicon drift detector operating at 20 keV was used to study the elemental composition of the powder samples. The internal structure of the nano-powders was investigated by a FEI Tecnai F20 Field Emission Gun operating at 200 kV. The Bruker AXS D8 Advance X-ray diffractometer with Cu-K α radiation and wavelength, $\lambda(K\alpha1) = 1.5406 \text{ \AA}$ was used to obtain the phase and structural identification of the nano-powders. Their thermal properties were studied using a Perkin Elmer STA 6000 instrument. And, a Thermo Scientific Nicolet Is10 FTIR spectrophotometer was used to evaluate the composition and structural quality of the ZnO nanoparticles.

Table 4.1: An overview of the experimental techniques needed for the study of ZnO nanoparticles' morphology, structure and properties [1, 2].

Technique	Information gathered
Scanning Electron Microscopy (SEM)	Surface morphology
Energy Dispersive Spectroscopy (EDS)	Elemental composition
Transmission Electron Microscopy (TEM)	Internal structure, Grain size
X-ray Diffraction (XRD)	Degree of crystallinity , Orientation, Crystal structure determination, Phase identification,
Differential Scanning Calorimetry (DSC)	Thermal properties in relation to the heat flow
Thermogravimetric Analysis (TGA)	Thermal properties in relation to changes in weight
Fourier Transform Infrared (FTIR)	Composition quality, Structural analysis

4.2.1 Scanning Electron Microscopy (SEM) and Energy Dispersive X-ray Spectroscopy (EDS)



4.2.1.1. Introduction

The Scanning Electron Microscope (SEM) is a widely used technique in a number of industries and laboratories to investigate the microstructural morphology and chemical composition of specimens up to a nanometer scale. SEM uses a focussed beam of high energy electrons to generate a variety of signals at the surface of solid specimens. These various signals that arise from the electron-sample interactions contain information about the sample including external morphology, chemical composition, crystalline structure and orientation of the materials making up the sample [3, 4].

4.2.1.2 Theory

When the incident electron strikes the specimen surface, instead of being bounced off immediately, the energetic electrons penetrate into the sample for some distance before they encounter and collide with a specimen atom. Thus, producing what is known as the region of primary excitation where a variety of signals are produced. This region is dependent upon the beam energy, atomic number and the density of the specimen. Figure 4.4 illustrates the

regions from which the various signals can be detected. The most widely used signal, the secondary electrons, gives the specimen's topographic information. The backscattered electrons are most valuable for illustrating contrasts in composition in multiphase specimens. The signals from the characteristic x-rays and Auger electrons provide chemical information of the specimen. SEM analysis is considered to be "non-destructive", that is, x-rays generated by electron interactions do not lead to volume loss of the sample, so it is possible to analyze the same materials repeatedly [4, 5].

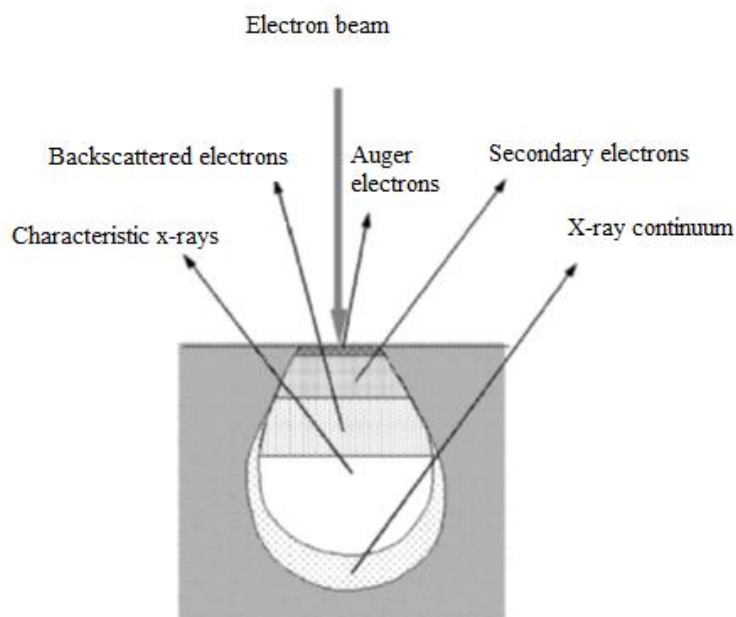


Figure 4.4: Illustration of the different signals produced during the electron beam-specimen interaction in the SEM microscope and the regions from which the signals can be detected [4].

4.2.1.3 Characteristic x-ray emission by an atom and Energy Dispersive Spectroscopy

Consider the schematic representation of an atom in Figure 4.5. When the incident beam bounces through the specimen creating secondary electrons, it leaves thousands of the specimen atoms with holes in the electron shells where the secondary electrons used to be. The resulting electron vacancies (holes) are filled by electrons from the outer shells. However, because the outer shells are at a higher energy state, energy in the form of x-rays is

emitted to balance the energy difference between the two electrons' state. To do this, the atom must lose some energy.

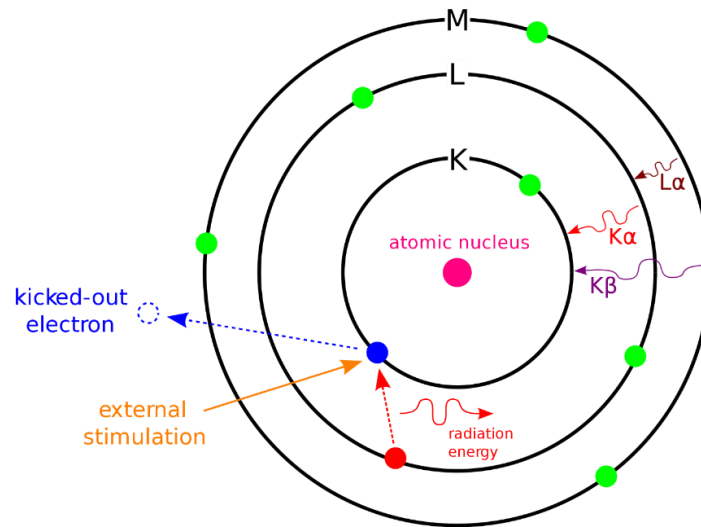


Figure 4.5: Characteristic x-ray emission by an atom [6].

The x-ray energy is characteristic of the element from which it was emitted. Once the incident x-ray strikes the semiconductor detector, it creates a charge pulse that is proportional to the energy of the x-ray. The charge pulse is converted to a voltage pulse (which remains proportional to the x-ray energy) by a charge-sensitive preamplifier. The signal is then sent to a multi-channel analyzer. The multi-channel analyzer counts the number of x-rays at each energy level that strikes the crystal. The energy for each incident x-ray is therefore sent to a computer for display and further data evaluation. The spectrum of x-ray energy versus counts is evaluated to determine the elemental composition of the sampled volume. EDS can also quantify the elements by calculating the area under the peak of each identified element and then converting the area under the peak into weight or atomic percent [1, 7].

4.2.1.4 Description of technique

The main components of SEM include:

- The source of electrons,
- Column down where electrons travel with electromagnetic lenses,
- Electron detector,
- Sample chamber and a computer to display the images.

Figure 4.6 shows a schematic diagram of the main components in the SEM column. Electrons produced at the top of the column are accelerated down and passed through a combination of lenses and apertures to produce a focused beam of electrons which hits the surface of the specimen which is mounted on a stage in the chamber area. The position of the electron beam on the sample is controlled by scan coils situated above the objective lens. These coils allow the beam to be scanned over the surface of the sample. This beam scanning enables information about a defined area on the specimen to be collected. As a result of the electron-sample interaction, a number of signals are produced. These signals are then detected by appropriate detectors [1, 3].

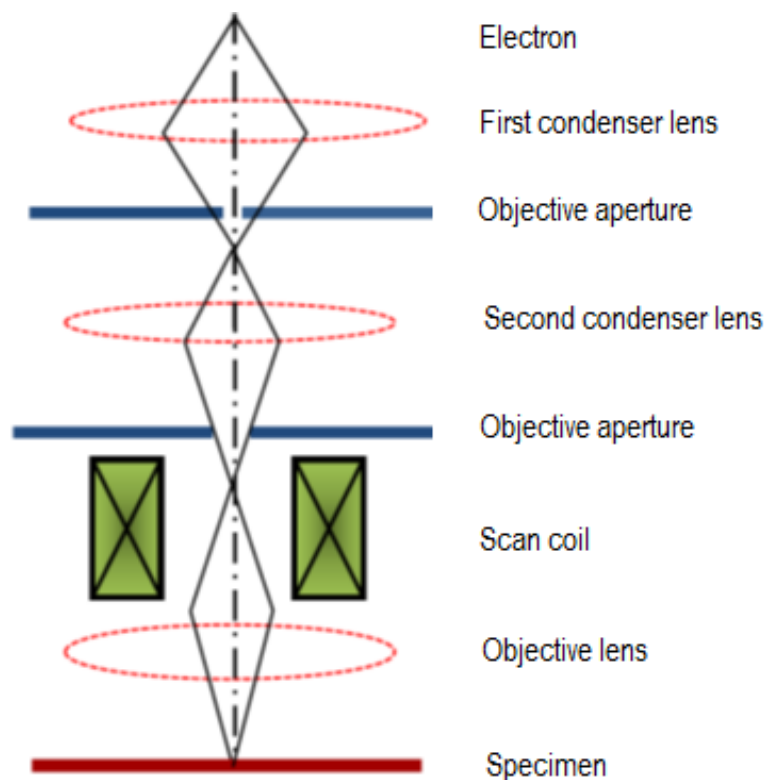


Figure 4.6: Schematic representation of the components comprising the SEM column [3].

4.2.1.5 Specimen preparation

Nonconductive specimens tend to charge when scanned by the electron beam causing scanning faults and other image artifacts. To prevent the accumulation of electrostatic charge at the surface, specimens are to be electrically conductive and electrically grounded. They are

therefore usually coated with an ultrathin coating of electrically conducting material including gold, gold/palladium alloy, platinum, which is deposited on the sample either by low-vacuum sputter coating or by high-vacuum evaporation [7, 8].

4.2.2 Transmission Electron Microscopy (TEM)

4.2.2.1 Introduction

Transmission Electron Microscopy (TEM) is one of the most important microscopic tools in nanotechnology for characterizing materials at a length scale from atoms to hundreds of nanometers. In this technique, a beam of electrons is transmitted through an ultrathin specimen (usually less than 100 nm), interacting with the specimen as it passes through it. Modern TEMs have the capacity to directly image atoms in crystalline specimens at resolutions close to 0.1 nm. High resolution TEM (HRTEM) is used to analyze the quality, shape, size and crystal structure features including grain boundaries and dislocations [9].

4.2.2.2. Description of technique

Consider the schematic layout of a TEM shown in Figure 4.7. In order to create a space where electrons are able to move, air is firstly pumped out of the vacuum chamber. The beam of electrons from the electron gun is focused into a small, thin, coherent beam by the use of the condenser lens. This beam is restricted by the condenser aperture, which excludes high angle electrons. The beam then strikes the specimen and parts of it are transmitted depending upon the thickness and electron transparency of the specimen. An image formed from the interaction of the electrons transmitted through the specimen is magnified and focused by the objective lens, passed down the column through the intermediate and projector lenses to be detected by a charge coupled device (CCD) camera. The darker areas of the image represent those areas of the sample that fewer electrons are transmitted through while the lighter areas of the image represent those areas of the sample that more electrons were transmitted through. This phenomenon is illustrated in Figure 4.8 where a TEM image of ZnO nanoparticles has been taken [2, 8].

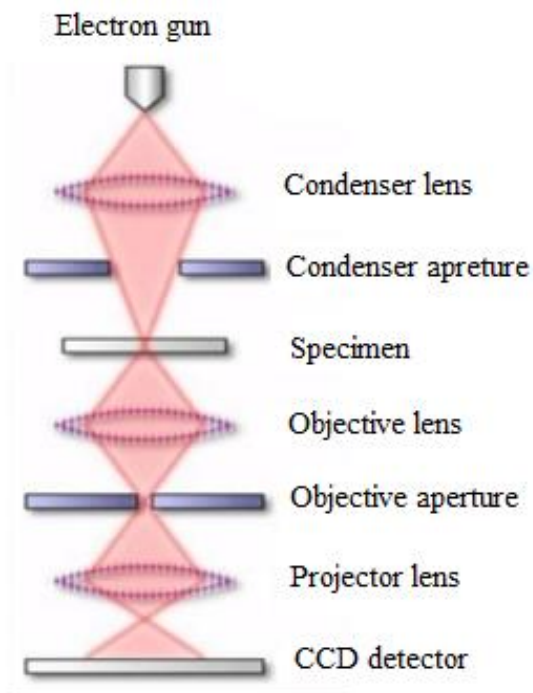


Figure 4.7: General layout of a TEM describing the path of electron beam in a TEM [10].

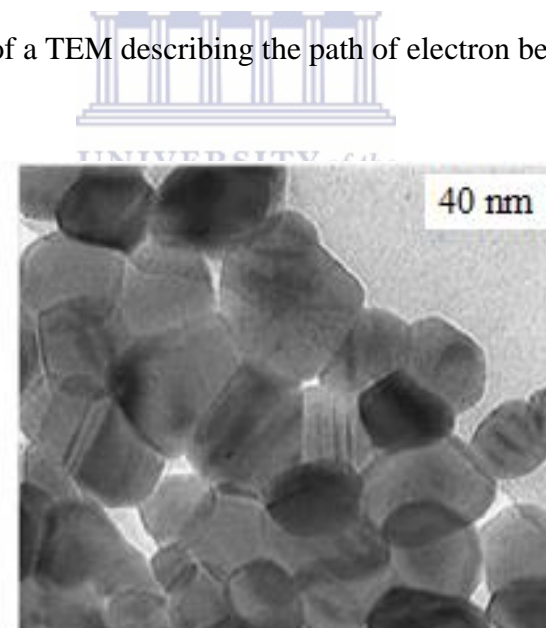


Figure 4.8: A typical TEM image of spherical ZnO nanoparticles calcined at 700 °C [11].

4.2.2.3 Sample preparation

A TEM specimen must be thin (i.e. electron transparent) enough to transmit sufficient electrons to form an image with minimum energy loss. Materials such as powders are quickly

prepared by the deposition of a dilute sample containing the specimen onto support grids or films. The specimens are then fixated by plastic embedding in order to withstand the instrument vacuum [12, 13].

4.2.3 X-ray diffraction (XRD)

4.2.3.1 Introduction

X-rays are electromagnetic radiation of exactly the same nature as light but of very much shorter wavelength. The unit of measurement in the x-ray region is the angstrom (\AA). X-rays used in diffraction have wavelengths lying approximately in the ranges 0.5 - 2.5 \AA , whereas the wavelength of visible light is of the order 6000 \AA . X-rays are produced when any electrically charged particle of sufficient kinetic energy rapidly decelerates [14]. Diffraction is essentially a scattering phenomenon (the absorption and re-emission of the incident radiation in different directions). Scattering occurs when the waves collide with a regular structure in which the repeating distance is approximately the same as the wavelength of the wave. The scattered waves interfere with each other. If the waves are in phase, then constructive interference occurs, on the other hand, destructive interference occurs if the waves are 180° out of phase. This means that if x-rays have a wavelength similar to the spacing of the atomic planes in a crystal, x-rays can easily be diffracted by a crystal and, hence, information about the arrangement of atoms in crystals can be obtained [15]. This phenomenon is known as x-ray diffraction (XRD) and can be used as a tool for the investigation of the fine, crystalline structure of matter [1]. In this study, XRD was used to identify the crystalline components of the ZnO nanoparticles [16].

4.2.3.2 Geometry of crystals

The atoms found in solid materials can be classified into crystals and amorphous. A crystal is defined as a solid composed of atoms arranged in a regular pattern in 3 dimensions. The periodic arrangement of atoms within a crystal material is known as a crystal structure and may be thought of as a set of imaginary points which has a fixed relation in space to the atoms of the crystal i.e. a skeleton on which the actual crystal is built up [14, 17]. This set of imaginary points is known as a point lattice and is so arranged that each point has identical surroundings, as shown in Figure 4.9 [1, 17].

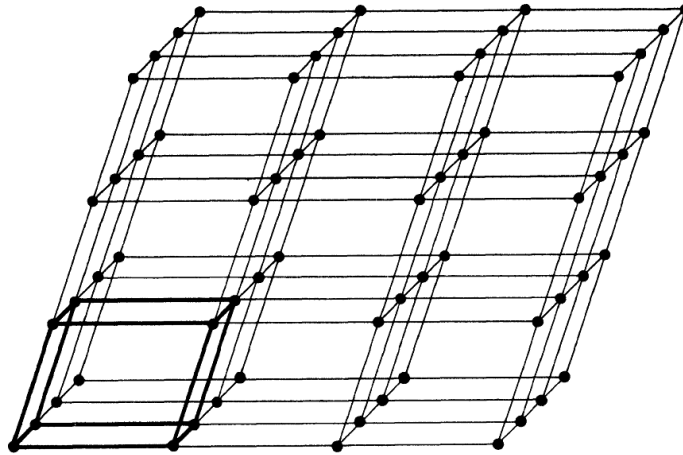


Figure 4.9: Illustration of a point lattice [14].

The repeating unit shown in Figure 4.10 is known as the unit cell of the lattice and is described by the three vectors **a**, **b** and **c** drawn from one corner of the cell. These vectors define the cell and are called the crystallographic axes of the unit cell. When described in terms of their lengths (*a*, *b* and *c*) and angles (α , β and γ) they are known as the lattice parameters or lattice constants of the cell. Depending on the relationship between the lattice parameters, one can distinguish between fourteen different point or Bravais lattices described in Table 4.2 [1].

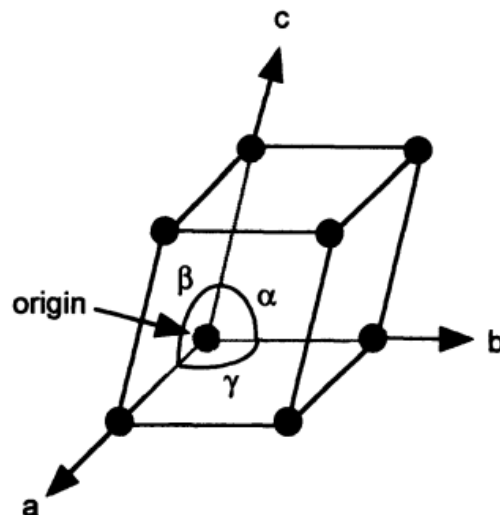


Figure 4.10: A primitive cell and the angles between the translational vectors [15].

Table 4.2: Description of the Bravais lattices and crystal systems [1].

System	Axial lengths and angles	Bravais lattice	Lattice symbol
Cubic	Three equal axis at right angles $a = b = c, \alpha = \beta = \gamma = 90^\circ$	Simple Body-centered Face-centered	P I F
Tetragonal	Three angles at right angles, two equal $a = b \neq c, \alpha = \beta = \gamma = 90^\circ$	Simple Body-centered	P I
Orthorhombic	Three unequal axes at right angles $a \neq b \neq c, \alpha = \beta = \gamma = 90^\circ$	Simple Body-centered Base-centered Face-centered	P I C F
Rhombohedral	Three equal axes, equally inclined $a = b = c, \alpha = \beta = \gamma \neq 90^\circ$	Simple	R
Hexagonal	Two equal co-planar axes at 120° , third axis at right angles $a = b \neq c, \alpha = \beta = 90^\circ, \gamma = 120^\circ$	Simple	P
Monoclinic	Three unequal axes, one pair not at right angles $a \neq b \neq c, \alpha = \gamma = 90^\circ \neq \beta$	Simple Base-centered	P C
Triclinic	Three unequal axes, unequally inclined and none at right angles $a \neq b \neq c, \alpha \neq \beta \neq \gamma \neq 90^\circ$	Simple	P

4.2.3.2.1 Miller indices

A notation system in crystallography that provide a way of uniquely describing different crystal planes in a lattice. Miller indices are determined by first identifying the points at which the plane intersects **a**, **b**, and **c** axes, measured in terms of fractions/multiples of the lattice parameters. The reciprocal of the intercepts is then taken and the Miller indices of any crystal system can be obtained and the resulting numbers are enclosed in parenthesis, (). The distance, *d*, between adjacent planes in the set (hkl) for a crystal in the hexagonal is

$$\frac{1}{d^2} = \frac{4}{3} \left(\frac{h^2+hk+k^2}{a^2} \right) + \frac{l^2}{c^2} \quad (4.1)$$

where *a*, *b*, *c*, α , β , and γ represent the parameters of the unit cell. Similar equations formulated for the other crystal system are shown in Table 4.2. The hexagonal unit cell is described by 3 vectors: **a**₁, **a**₂, and **c**. Vectors **a**₁, **a**₂ lie at 120° to one another in the same plane called basal plane, and **c** is perpendicular to the basal plane [15].

4.2.3.3 Bragg's law for diffraction

X-rays scattered from a crystalline solid interfere constructively producing diffracted beams in specific directions governed by the wavelength (λ) of the incident radiation and the nature of the crystalline sample. Bragg's law, formulated in 1912 by W.L Bragg, is a simple predictable explanation which relates the wavelength of the x-rays of the diffracted beam to the spacing of the atomic planes of a crystal [15 - 17].

Consider a monochromatic beam of parallel x-rays A and A', striking a set of parallel planes, a distance *d* apart, that specularly reflect the incident x-rays elastically. Suppose two waves that are in phase are incident at an angle θ to the parallel plane as shown in Figure 4.11. The scattered rays B and B', resulting from the interaction of the incident beam with the atoms of the parallel planes will recombine to form a diffracted beam if and only if their path difference is a whole multiple of wavelengths, i.e.

$$DE + EC = d\sin\theta + d\sin\theta = n\lambda \quad (4.2)$$

where *n* is the integral number (order of diffraction), λ is the wavelengths of the radiation, *d* is the interplanar spacing and θ is the x-ray's incident angle (Bragg's angle)

Equation (4.2) can be simplified to give

$$2d\sin\theta = n\lambda \quad (4.3)$$

The relation (4.3) is known as Bragg's equation and gives the angle θ , at which a set of planes of spacing d constructively reflects x-ray radiation of wavelength λ in the n^{th} order [18].

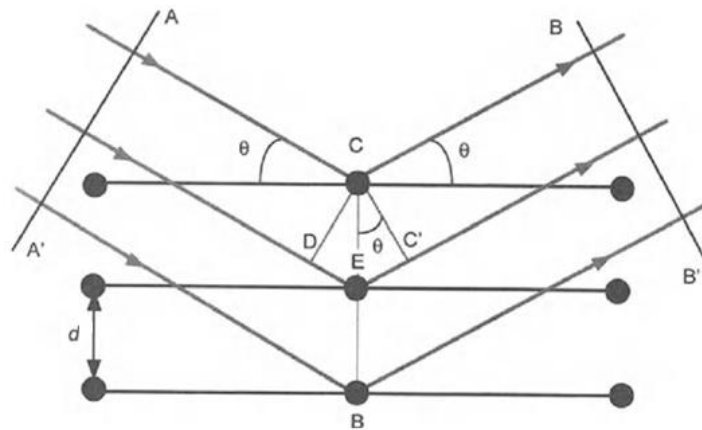


Figure 4.11: Schematic representation of diffraction of x-rays by a crystal [15].

4.2.3.4 Practical aspect of x-ray diffraction

The x-ray diffractometer is a measuring instrument used for analysing the structure of a material from the scattering pattern by measuring the intensity of the diffracted beam of x-rays with an electronic counter. Figure 4.12 (a) shows the three basic components of a diffractometer, namely: the x-ray source (B), specimen (E) and the x-ray detector (D), all lie on the circumference of the focusing circle (A). Most x-ray diffractometers are configured according to the Bragg-Brentano geometry where the x-ray source is fixed, and the detector moves through a range of angles (known as the θ - 2θ geometry), and the θ - θ geometry, where both the x-ray source and the detector move in the vertical plane in opposite directions above the centre of the specimen. The diffractometer circle, also referred to as goniometer circle (C), is the central component of an x-ray diffractometer and contains the specimen holder, and has arms to which the x-ray source and the detector are mounted (as shown in Figure 4.12 (a)). X-rays are generated by directing an electron beam of high voltage at a metal target anode inside an evacuated x-ray tube as shown in Figure 4.12 (b). These line source of x-rays passes through a series of slits called Soller slits, to the divergence slit which define the divergence (or width) of the incident beam. The specimen (E) which is positioned

such that its reflecting planes make some particular angle θ with the incident beam then diffracts the beam at the corresponding angle 2θ . After the beam has been diffracted by the specimen, it passes through another set of slits (antiscatter) which reduces the background radiation, thus improving the peak-to-background ratio, by making sure that the detector can receive x-rays only from the specimen area. The intensity of the diffracted beam is then measured in the ionization chamber (D) and its wavelength calculated from the Bragg law, this procedure being repeated for various angles θ [14, 15, 19].

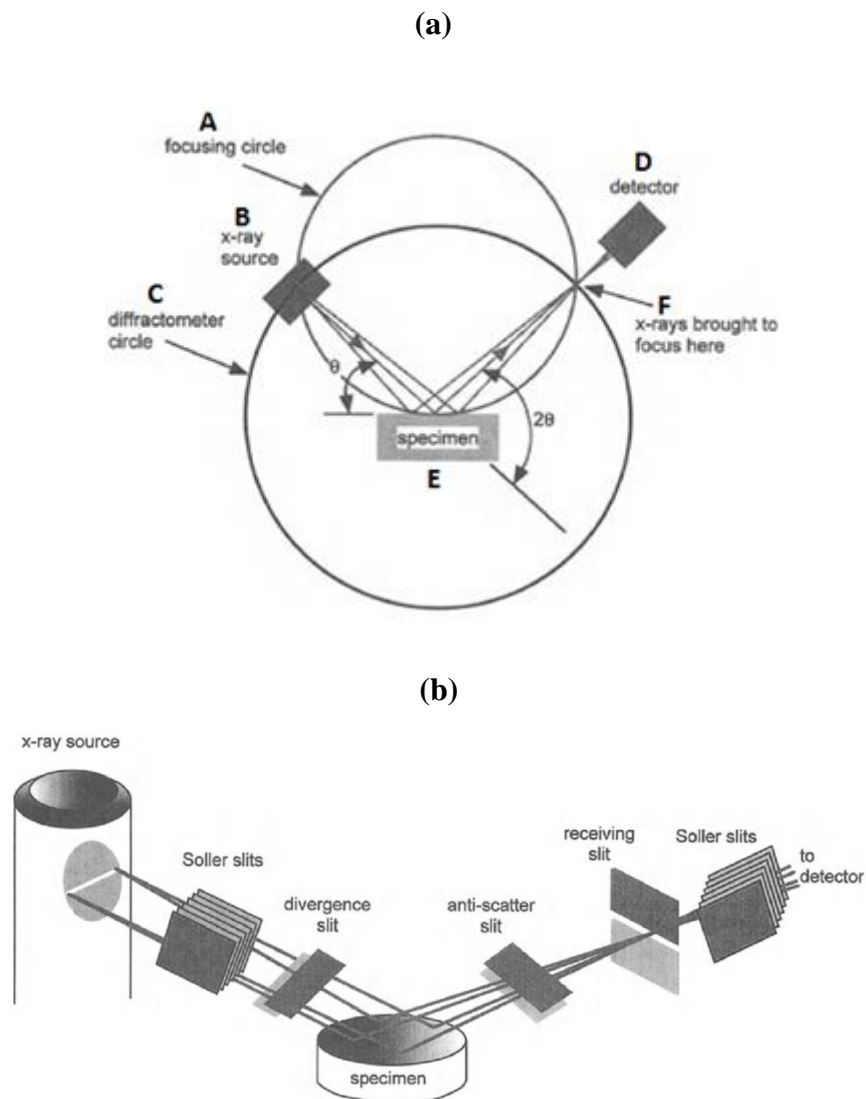


Figure 4.12: Schematic illustration of (a) an x-ray diffractometer, (b) the arrangement of slits in a diffractometer [15].

4.2.3.5 Data analysis

A typical XRD spectrum like the one shown in Figure 4.13 shows several peaks at fixed θ angles. The peak positions make it possible to identify the kind of crystals present on the sample. The sharp and clear diffraction peaks are obtained from the crystals having precise periodicities over long distances. The broadened, distorted, and weakened diffraction peaks are obtained from crystals having defects, as their periodicity in their atomic arrangements are less precise. Appropriate software packages are used to analyse the peaks and then the International Centre for Diffraction Data (ICDD) database is used to identify the candidate materials. In the case whereby the sample contains a mixture of unknown crystalline phases, computerized searches for pattern matches are mostly valuable. The atomic pair distribution function (PDF) technique which is a specialized approach, has been developed to analyse diffuse (i.e. non-Bragg type) XRD patterns and obtain important structural information for bulk non-crystalline materials such as near atomic neighbour separations and coordination numbers. [2]

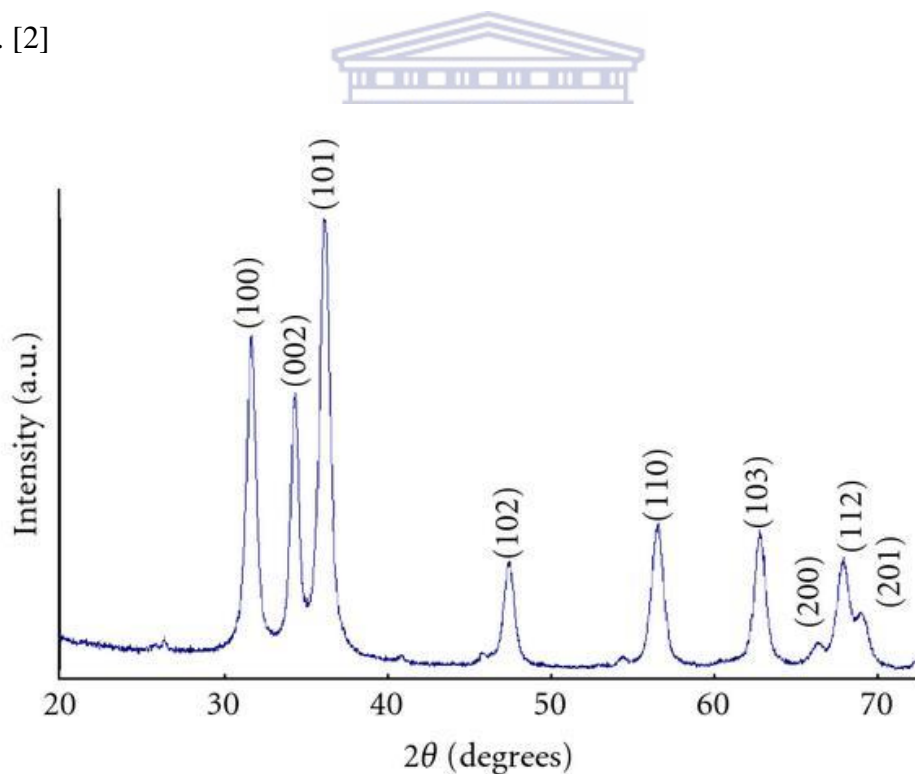


Figure 4.13: X-ray diffraction spectrum of ZnO [20].

4.2.4 Differential Scanning Calorimetry (DSC)

4.2.4.1 Introduction

Calorimetry is a technique for determining the quantity of heat that is either absorbed or released by a substance undergoing a physical or a chemical change. A DSC is a specific type of calorimetry which measures the heat effects associated with phase transitions or chemical reactions that occur as a sample is heated, cooled or held isothermally, as a function of temperature [21]. The DSC is used to obtain the thermal critical points such as melting point, crystallization, enthalpy, specific heat as well as glass transition temperatures of the sample. The ability to determine such transition temperatures and enthalpies makes DSC a valuable tool in producing the phase diagrams of the ZnO nanoparticles [22].

4.2.4.2 Description of technique

In a DSC analysis, the sample and an empty reference crucible - an inert material such as alumina, are placed on small separate platforms within the DSC chamber. The schematic principle of the DSC is described in Figure 4.14. The thermocouples lying below the pans heat each chamber in a way that their temperatures are always equal. The temperature of each chamber is constantly monitored. The basic principle is that when the sample undergoes a physical transformation such as phase transitions, more (or less) heat will need to flow to it than to the reference in order to maintain the two at the same temperature. The nitrogen atmosphere is maintained within the DSC system in order to create a reproducible and dry atmosphere and also to eliminate air oxidation of the samples at high temperatures [22 - 24].

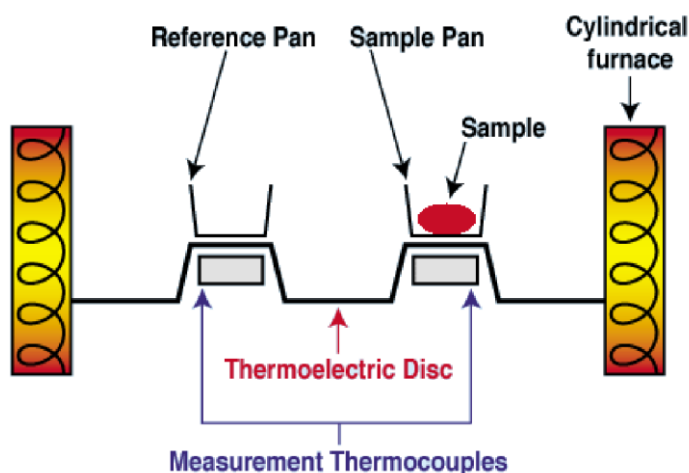


Figure 4.14: Schematic principle of DSC measurement [25].

4.2.4.3 Data analysis

The physical or a chemical change the sample undergoes alters its internal energy. At constant pressure, this internal energy is known as enthalpy, H. Expressed mathematically as

$$\left(\frac{dq}{dt}\right)_p = \frac{dH}{dt} \quad (4.4)$$

where $\frac{dH}{dt}$ is the heat flow measured in $\text{mcal}\cdot\text{s}^{-1}$. During the heating of a sample peaks with positive and negative heat flow signal are recorded. Figure 4.15 shows the DSC curve demonstrating the appearance of several common features. A transient is a slight period of instability at the start (and also at the end) of a run before a stable heating or cooling rate is established. The glass transition temperature, T_g , is the temperature at which amorphous (non-crystalline) polymers are converted from a brittle, glasslike form to a rubbery, flexible form. The point whereby the molecules within the sample obtain enough freedom of motion and arrange themselves into a crystalline solid is known as the crystallization temperature (T_c) and this transition from amorphous solid to crystalline form results in an exothermic peak in the DSC curve. As the temperature increases the sample eventually reaches its melting temperature, T_m . The melting process results in an endothermic peak. The integral under the DSC peak, just above the baseline, gives the total enthalpy change for the process [22, 23].

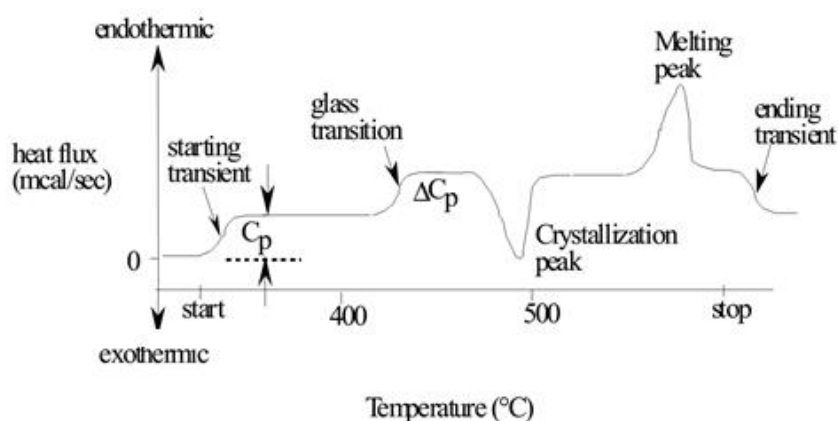


Figure 4.15: Typical DSC thermogram labelling four critical points; the glass transition temperature (T_g), the crystallization temperature (T_c), the melting temperature (T_m), and the curing temperature [23].

4.2.5 Thermal Gravimetric Analysis (TGA)

4.2.5.1 Introduction

Thermal gravimetric analysis is an experimental technique that measures the amount and the rate of change in the mass of a sample as a function of sample temperature or time. The measurements are mainly used to determine the material's thermal stabilities as well as their compositional properties. The difference in weight observed occurs due to the separation or the formation of different chemical and physical bonds at higher temperatures. The ability of a TGA instrument to quantify loss of water, loss of solvent, loss of plasticizer, decarboxylation, pyrolysis, oxidation and decomposition which are all usually observed upon heating (although there are some experiments where information may be obtained upon cooling), makes it a significant technique in analysing the ZnO nanoparticles [22, 26].

4.2.5.2 Description of technique

The sample is placed in a small, electrically heated furnace equipped with a thermocouple to monitor accurate measurements of the temperature by comparing its voltage output with that of the voltage-versus-temperature table stored in the computer's memory. Figure 4.16 shows a schematic diagram of such a setup. A reference sample may be placed on another balance in a separate chamber. The atmosphere in the sample chamber may be purged with an inert gas to prevent oxidation or other undesired reactions. As the furnace temperature is raised slowly, the temperature of the sample and the corresponding weight are recorded [27, 28].

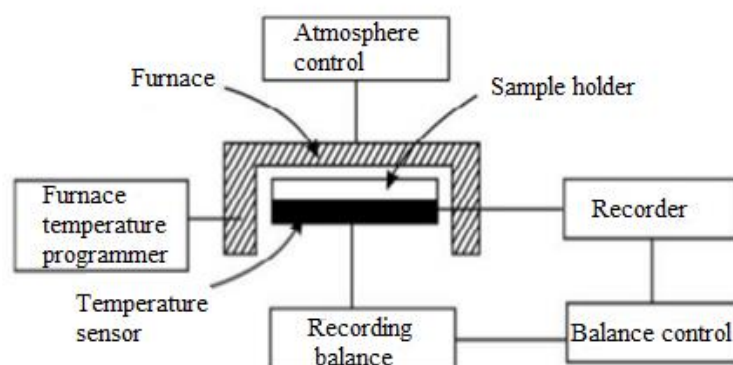


Figure 4.16: Schematic diagram of TGA [29].

4.2.5.3 Data analysis

As the temperature increases, various components of the sample are decomposed and the weight percentage of each resulting mass change can be measured. TG curves are normally plotted with the mass change in percentage on the y-axis and temperature on the x-axis. The mass changes a sample undergoes are displayed as steps in the TGA curve. These steps are classified according to their shapes as illustrated in Figure 4.17 [22, 30].

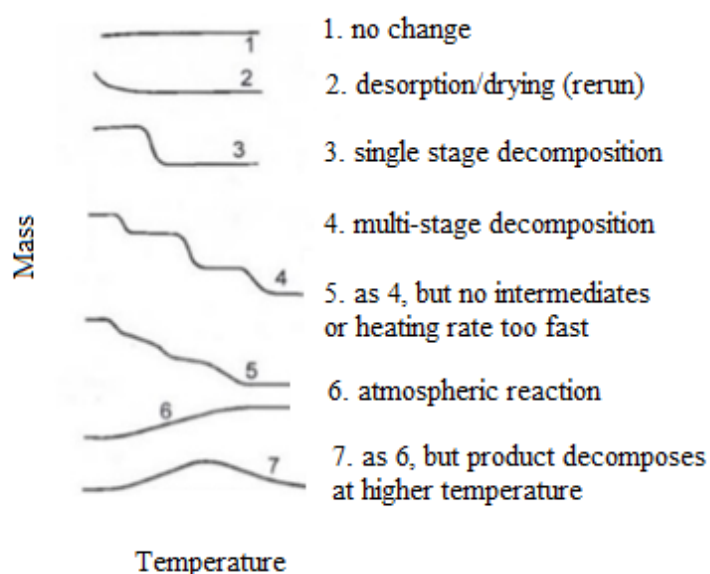


Figure 4.17: Classification of TG curves [31].

4.2.6 Fourier Transform Infrared Spectroscopy (FT-IR)

4.2.6.1 Introduction

Infrared spectroscopy is the study of the interaction of light with matter. Infrared, just like visible light, is a form of electromagnetic radiation with longer wavenumber than the visible light extending from the nominal red edge of the visible spectrum at 14286 cm^{-1} to 200 cm^{-1} . Upon irradiation with infrared radiation, certain molecular bonds respond to specific frequencies by vibrating faster in several modes including stretching, rocking and scissoring. This response can be detected and translated into a visual representation called an IR spectrum. The technique which is used to obtain an infrared spectrum is known as FTIR and it gives information on the type of bonding within the sample. The advantage of FTIR from

other infrared spectral analytical methods is that all phases of matter may be studied, making it the most preferred technique in determining the quality of the ZnO nanoparticles [32, 33].

4.2.6.2 Description of technique

An IR spectrometer is used to measure the FTIR spectrum and it consists of a source, interferometer, sample compartment, detector amplifier, A/D convertor, and a computer.

Figure 4.18 shows the basic components of the IR spectrometer.

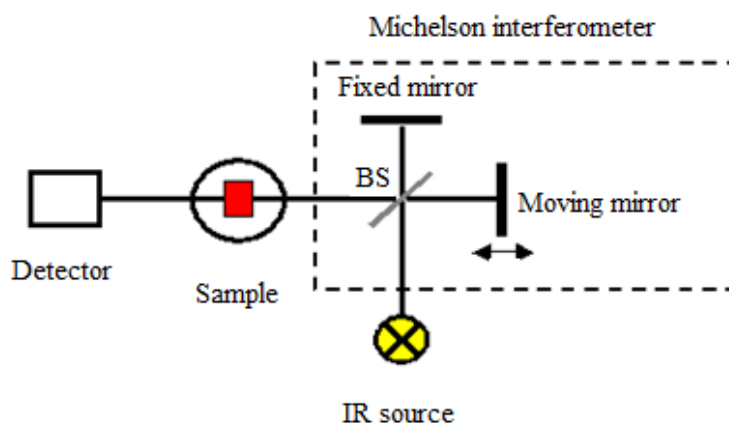


Figure 4.18: Schematic representation of an FTIR spectrometer [34].

Radiation emitted from the source is split into two (so that the paths of the two beams are different) with a beam splitter in the interferometer. The role of the interferometer, shown in Figure 4.19 is to measure the interference pattern between the two waves.

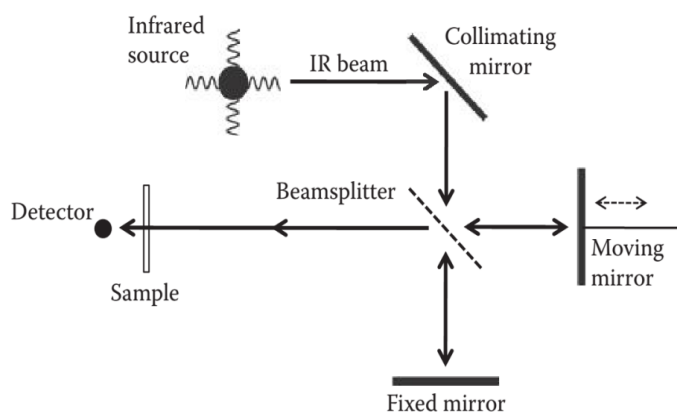


Figure 4.19: An optical diagram of a Michelson interferometer [36].

The fixed and moving mirrors reflect each of the beam back to the beamsplitter, where the two beams recombine into one and falls on the detector. The two beams combine constructively or destructively varying as the optical path difference, when the moving mirror is moved. When the combined beam is transmitted through the sample, it is detected as a signal produced as function of the change of the pathlength called an interferogram, and it contains all infrared information on the sample. The signal is then amplified and converted to digital signal by the amplifier and analog-to-digital converter, respectively. The spectrum is obtained from the interferogram by the mathematical process of Fourier transformation [2, 35]. The mathematical expression of the Fourier transform $F(\omega)$ is given by:

$$F(\omega) = \frac{1}{2} \int_{-\infty}^{+\infty} f(r) e^{i\omega r} dr \quad (4.5)$$

where ω is the angular frequency, r is the optical path difference, $F(\omega)$ is the spectrum, and $f(r)$ is the interferogram. The interferogram is determined experimentally in FTIR and the corresponding spectrum is computed automatically from using Fourier transform. To measure an interferogram using a Michelson interferometer the mirror is moved back and forth once. This is called a scan. The interferograms measured while scanning are Fourier transformed to yield a spectrum, hence the term Fourier Transform Infrared (FTIR) spectroscopy [36].

4.2.6.3 Data analysis

The frequency of vibrational modes is characteristic of the specific functional group in which the motion is centred. Thus, the observation of spectral features in a certain region of the infrared spectrum is often an indicative of a specific chemical functional group in the molecule as shown in Figure 4.20. Because each different material is a unique combination of atoms, no two compounds produce the exact same infrared spectrum. Thus, infrared spectroscopy can result in a positive identification (qualitative analysis) of every kind of material utilized in the ZnO synthesis. In addition, the amount of material is obtainable from the size of the peaks in the spectrum. The vibrational modes that vary from one molecule to another are useful in distinguishing one molecular from another that contains similar functional groups, hence known as the fingerprint region [32, 36, 37].

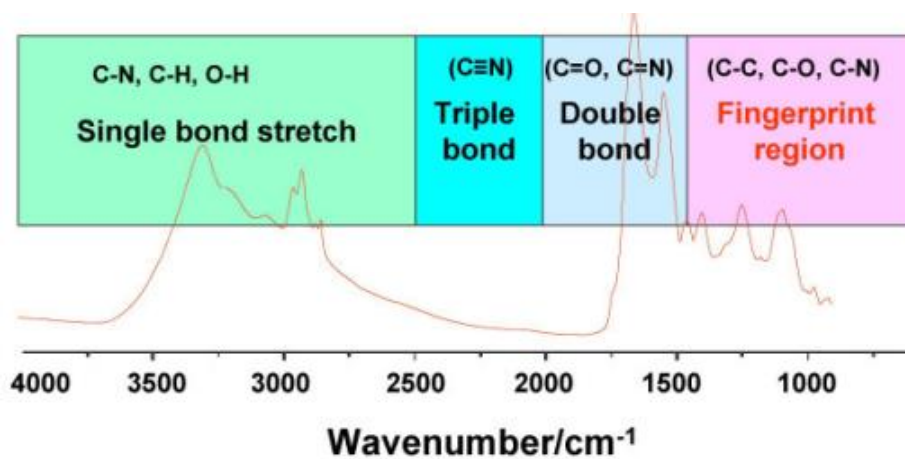


Figure 4.20: Representative spectrum in the mid-IR region. The region below 1500 cm⁻¹ is defined as the fingerprint region. The region above 1500 cm⁻¹ is the functional group region [38].



4.3 References

- [1] F. Cummings, "Hot-wire Chemical Vapour Deposition of Carbon Nanotubes," University of the Western Cape, Bellville, 2006.
- [2] A. Mboniyirivuze, "Indigenous Natural Dyes for Gratzel Solar Cells: Sepia Melanin," University of South Africa, Pretoria, 2014.
- [3] "How an SEM works," [Online]. Available: <http://www.nanoscience.com/products/sem/technology-overview/how-sem-works/>. [Accessed 20 April 2016].
- [4] W. Zhou and Z. Wang, Scanning Microscopy for Nanotechnology: Techniques and Applications, New York: Springer, 2006.
- [5] "Scanning Electron Microscopy," [Online]. Available: http://serc.carleton.edu/research_education/geochemsheets/techniques/SEM.html. [Accessed 20 April 2016].
- [6] J. Russ, Fundamentals of Energy Dispersive X-ray Analysis, London: Butterworths&Co, 1984.
- [7] "Energy Dispersive X-ray Spectroscopy," [Online]. Available: https://en.wikipedia.org/wiki/Energy-dispersive_X-ray_spectroscopy. [Accessed 20 April 2016].
- [8] P. Goodhew, J. Humphreys and R. Beanland, Electron Microscopy and Analysis, London and New York: Taylor and Francis, 2001.
- [9] "Transmission Electron Microscopy," [Online]. Available: <http://www.microscopemaster.com/transmission-electron-microscope.html>. [Accessed 20 April 2016].
- [10] M. Humphry, B. Kraus, A. Hurst, M. Maiden and J. Rodenburg, "Ptychographic electron microscopy using high-angle dark-field scattering for sub-nanometre resolution imaging," *Nature Communications*, vol. 3, no. 730, pp. 1-12, 2012.
- [11] M. Javidi, M. Mortazavi, N. Naghavi, A. Nejat and M. Zarei, "Zinc oxide nanoparticles as sealer in endodontics and its sealing ability," *Contemporary Clinical Dentistry*, vol. 5, no. 1, pp. 20-24, 2014.
- [12] "Transmission Electron Microscopy," [Online]. Available: https://en.wikipedia.org/wiki/Transmission_electron_microscopy. [Accessed 20 April 2016].
- [13] "Transmission Electron Microscopy (TEM)," [Online]. Available: <https://www2.warwick.ac.uk/fac/sci/physics/current/postgraduate/regs/mpags/ex5/techniques/structural/tem/>. [Accessed 20 April 2016].

- [14] B. Cullity and S. Stock, Elements of X-Ray Diffraction, New Jersey: Pearson Education, 2013.
- [15] C. Suryanarayana and M. Grant-Norton, X-Ray Diffraction: A Practical Approach, New York: Springer, 1998.
- [16] S. Thabethe, "Growth and characterization of FeSi Nanowires by Chemical Vapor Deposition for Gas Sensing Applications," University of the Western Cape, Bellville, 2014.
- [17] R. Adam, "Synthesis and Characterization of Silver nanoparticles for Photovoltaic Applications," University of the Western Cape, Bellville, 2013.
- [18] "Introduction to X-ray Diffraction," MediaWiki, [Online]. Available: http://202.141.40.218/wiki/index.php/Unit-2:_Introduction_to_X-ray_diffraction. [Accessed 22 March 2016].
- [19] R. Panwar, "Preparation of modified ZnO nanoparticles by sol-gel and their characterization," Thapar University, Punjab, 2009.
- [20] S. Talam, S. Karumuri and N. Gunnam, "Synthesis, Characterization, and Spectroscopic Properties of ZnO Nanoparticles," *ISRN Nanotechnology*, vol. 2012, no. 1, pp. 1-6, 2012.
- [21] "Differential Scanning Calorimetry (DSC) theory," [Online]. Available: <http://particle.dk/methods-analytical-laboratory/dsc-differential-scanning-calorimetry/dsc-theory/>. [Accessed 12 April 2016].
- [22] P. Gabbott, Ed., Principles and Applications of Thermal Analysis, New Delhi: Blackwell Publishing, 2008.
- [23] "Differential Scanning Calorimetry; First and Second Order Transitions in Polymers," [Online]. Available: <http://www.colby.edu/chemistry/PChem/lab/DiffScanningCal.pdf>. [Accessed 20 April 2016].
- [24] [Online]. Available: <http://www.flemingptc.co.uk/our-services/dsc-tga/>. [Accessed 20 April 2016].
- [25] M. Gauthier, "Thermal analysis," [Online]. Available: <http://www.slideshare.net/shivadheeraj/dta-raj-bpharm>. [Accessed 15 February 2016].
- [26] "Thermogravimetric Analysis (TGA)," [Online]. Available: https://www.perkinelmer.com/CMSResources/Images/44-74556GDE_TGABeginnersGuide.pdf. [Accessed 20 April 2016].
- [27] "Thermogravimetric analysis," [Online]. Available: https://en.wikipedia.org/wiki/Thermogravimetric_analysis. [Accessed 20 April 2016].
- [28] "Thermogravimetry (TG) or Thermogravimetric Analysis (TGA) or Thermal Gravimetric Analysis," [Online]. Available:

- <http://www.andersonmaterials.com/tga.html>. [Accessed 17 February 2016].
- [29] S. Selvaraj, "Thermogravimetric Analysis," LinkedIn SlideShare, Madras, 2015.
- [30] B. Stanton, L. Zhu and C. Atwood, "Determination of the percent by mass of the components in a mixture by Thermal Gravimetric Analysis," in *Experiments in General Chemistry*, Belmont, Brooks/Cole, pp. 43-56, 2010.
- [31] "Thermogravimetry Analysis," [Online]. Available: <http://www.slideshare.net/KalsoomMohammed/thermogravimetry-analysis-tga>. [Accessed 18 February 2016].
- [32] "Introduction to Fourier Transform Infrared Spectrometry," [Online]. Available: http://www.niu.edu/analyticallab/_pdf/ftir/FTIRintro.pdf. [Accessed 18 February 2016].
- [33] "Infrared," MediaWiki, [Online]. Available: <https://en.wikipedia.org/wiki/Infrared>. [Accessed 06 April 2016].
- [34] "Michelson Interferometer," [Online]. Available: https://www.researchgate.net/profile/Francisco_Rodriguez-Fortuno/publication/224096173/figure/fig11/AS:324349404958740@1454342332714/Sketch-of-the-measurement-setup-The-Michelson-interferometer-and-the-Globar-source.png. [Accessed 20 April 2016].
- [35] "Principles of FTIR," [Online]. Available: <http://www.slideshare.net/muttaqinpapasafira/principles-of-ftir>. [Accessed 07 April 2016].
- [36] B. Smith, *Fundamentals of Fourier Transform Infrared Spectroscopy*, New York: CRC Press, 2011.
- [37] P. Griffiths and J. de Haseth, *Fourier Transform Infrared Spectroscopy*, New Jersey: Wiley, 2007.
- [38] A. Hynes, D. Scott, A. Man, D. Singer, M. Sowa and K. Liu, "Molecular mapping of periodontal tissues using infrared microspectroscopy," *BioMed Central*, vol. 5, no. 2, pp. 1-10, 2005.

Chapter 5: Results and discussion

The leaf extract of *Aspalathus Linearis* was used as a reducing agent to reduce the $\text{Zn}(\text{C}_4\text{H}_6\text{O}_4) \cdot 2\text{H}_2\text{O}$ precursor into ZnO. Following a drying process at 100 °C, the obtained ZnO powder (as-prepared) was divided into 5 samples and annealed at different temperatures for 2 hours. The physical properties of the powders were investigated using SEM, EDS, TEM, XRD, DSC/TGA and FTIR.

In this chapter, the results obtained from SEM, EDS, TEM, XRD, DSC/TGA and FTIR for the powdered samples (as described in Table 5.1 below) will be discussed. In addition to this, the effect of the annealing temperature on the samples will also be discussed.

Table 5.1. Description of the powdered samples at different temperature conditions.

Sample #	Description
1	As-prepared (not annealed)
2	Annealed at 300 °C
3	Annealed at 400 °C
4	Annealed at 500 °C
5	Annealed at 600 °C

5.1. Scanning Electron Microscopy

The SEM image of the as-prepared powder is shown in Figure 5.1(a). The image shows few large clusters as well as many quasi-spherical shaped ZnO nanoparticles agglomerated together. The cause of the agglomeration could be due to the polarity and electrostatic attraction of ZnO nanoparticles rising from the biological material. The particle size distribution of the nanoparticles was estimated from the ImageJ software by treating the nanoparticles as spheres and thus calculating the particle size distribution from the deduced area. Figure 5.1 (b) shows the average diameter of the as prepared nanoparticles to be ranging from ~10 to 40 nm. By fitting the corresponding histogram data with a Gaussian distribution, the average particle size of the as-prepared nanoparticles was found to be about 18.4 ± 0.4 nm.

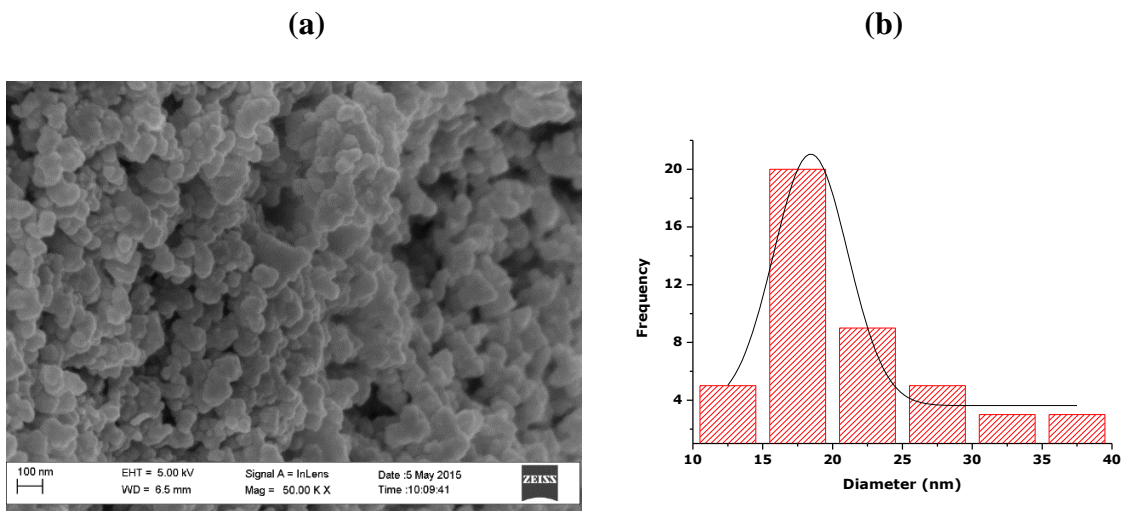


Figure 5.1: (a) SEM image and (b) the size distribution of the ‘as-prepared’ powder.

The SEM image of the powder that was annealed at 300 °C (Figure 5.2(a)) shows some short rod-like particles, with the majority of the nanoparticles appearing to be quasi-spherical and clustered together. This variety in morphology might be due to the combining of smaller nanoparticles into larger nanoparticles that are more stable [1]. From the Image J software, the size distribution of the nanoparticles was found to be ranging from ~15 to 45 nm (Figure 5.2(b)) with the average diameter of about 24.6 ± 0.8 nm.

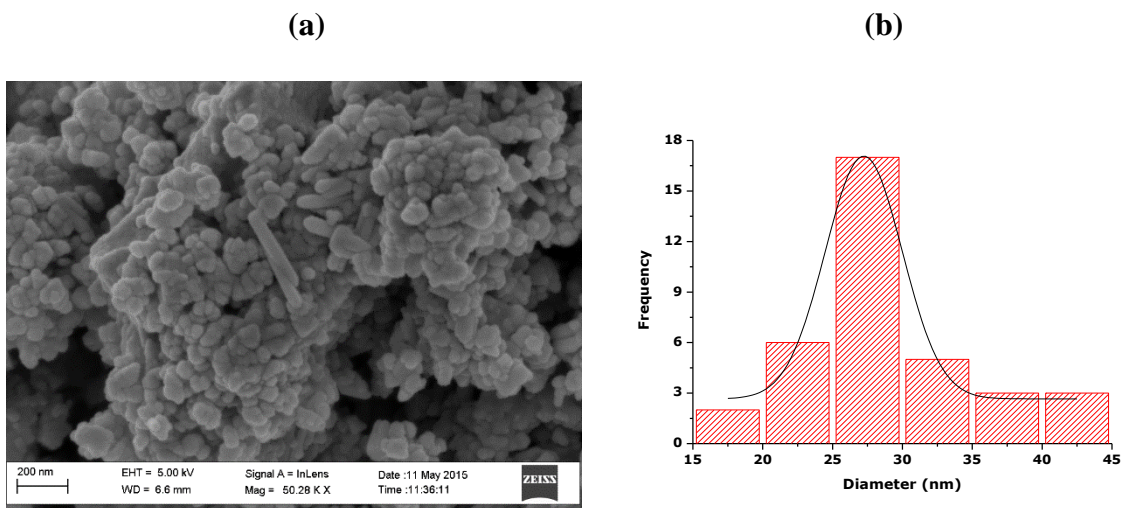


Figure 5.2: (a) SEM image and (b) the size distribution of the powder annealed at 300 °C.

When the temperature was increased to 400 °C (depicted in Figure 5.3(a)), the large clusters and rod-like structures which were seen before at lower temperatures seem to change into finer quasi-spherical ZnO nanoparticles with a particle size distribution ranging from ~10 to 45 nm as shown in Figure 5.3(b). Their average particle size is centred at about 27.2 ± 0.7 nm.

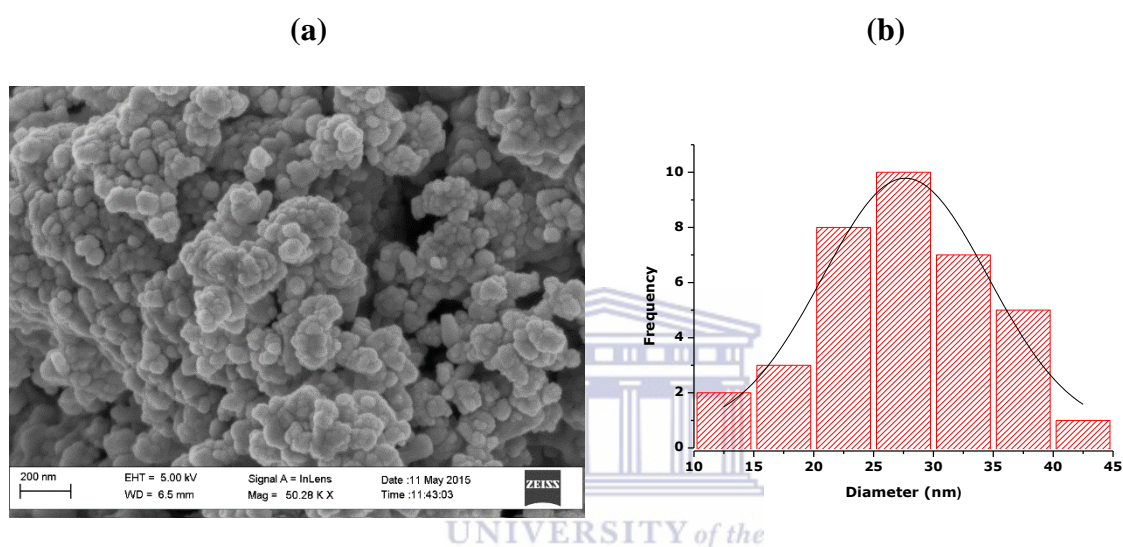


Figure 5.3: (a) SEM image and (b) the size distribution of the powder annealed at 400 °C.

The morphology of ZnO quasi-spheres is seen throughout higher annealing temperatures of 500 °C and 600 °C shown in Figure 5.4(a) and Figure 5.5(a), respectively. The particle size distribution of the powder that was annealed at 500 °C is shown in Figure 5.4(b). The average particle size was found to be about 27.6 ± 0.6 nm. Figure 5.5(b) shows that particle distribution of the powder annealed at 600 °C is between ~10 and 60 nm with an average particle size of about 28.5 ± 0.2 nm. As shown in Figure 5.6, the average size of the nanoparticles increases with increase in the annealing temperature.

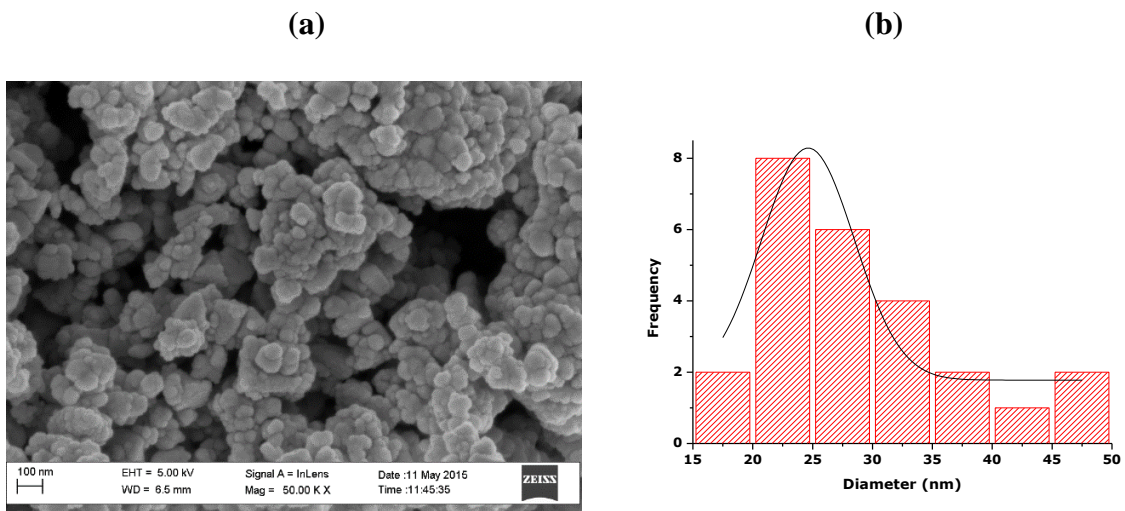


Figure 5.4: (a) SEM image and (b) the size distribution of the powder annealed at 500 °C.

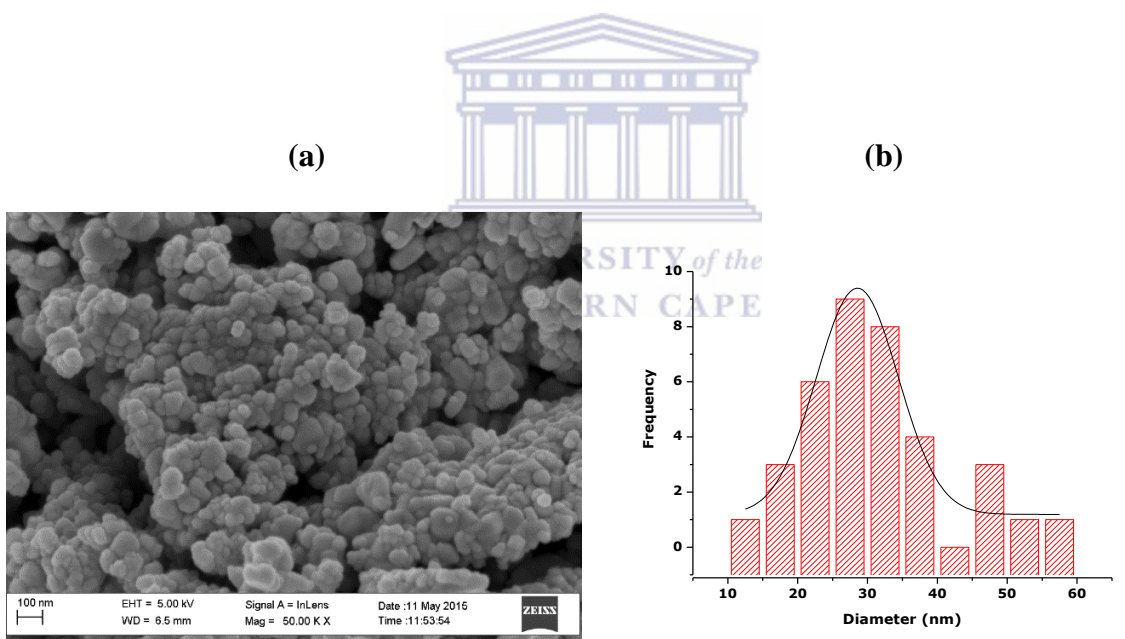


Figure 5.5: (a) SEM image and (b) the size distribution of the powder annealed at 600 °C.

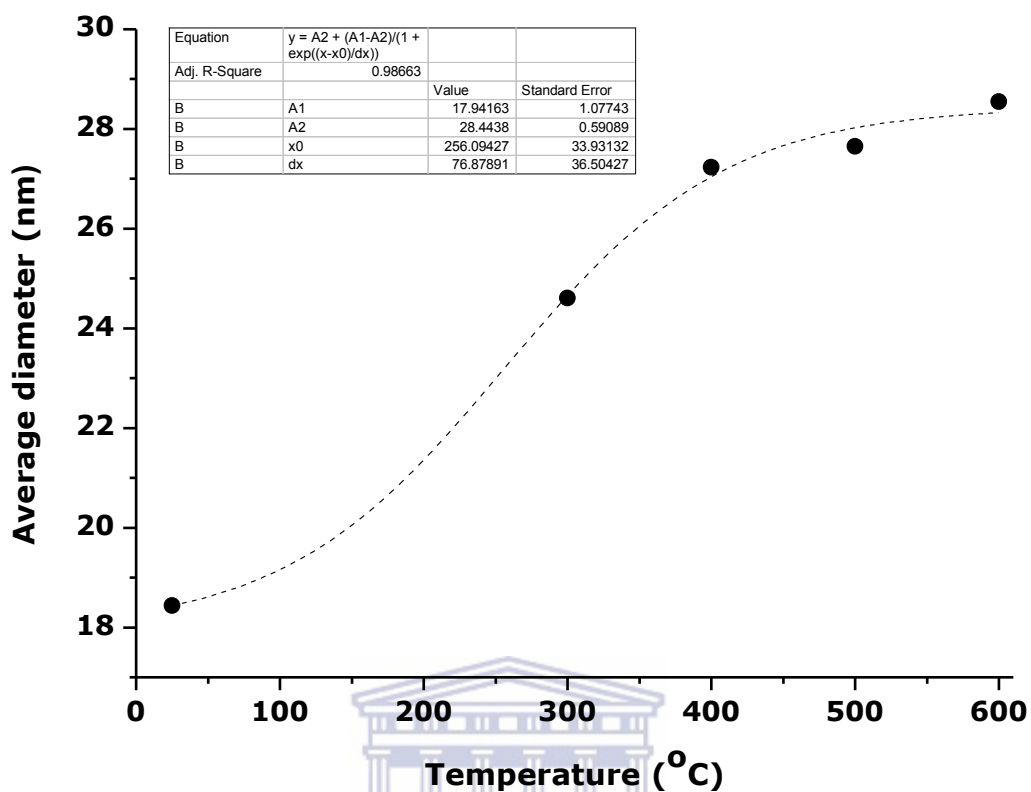


Figure 5.6: Variation of the average size of the ZnO nanoparticles with annealing temperature. The line is the corresponding simulation curve.

5.2 Energy Dispersive Spectroscopy (EDS)

The EDS spectra of the ZnO powder samples is shown in Figure 5.7. The EDS spectra of the powder samples confirm the presence of zinc and oxygen whose intensity peaks increase with an increase in annealing temperature. In Figure 5.8, the appearance of the K peak (which is attributed to the natural extract's organic matter) is shown to decrease as the annealing temperature increases. It can hence be deduced that higher annealing temperatures gradually decomposes the K based compound/s. No other elements were observed except for the C peak from the carbon coated grid as well as the Au and Pd used as coating for conductivity purposes. The deposition of Au and Pd is thickness dependent, hence the degradation of the Au peak at the temperature of 300 °C is an experimental artefact and has no impact on the other elements. Consequently, it can deduce that a pure chemical form of ZnO has been achieved. And this trend is also seen in higher annealing temperatures of 400 °C, 500 °C and 600 °C.

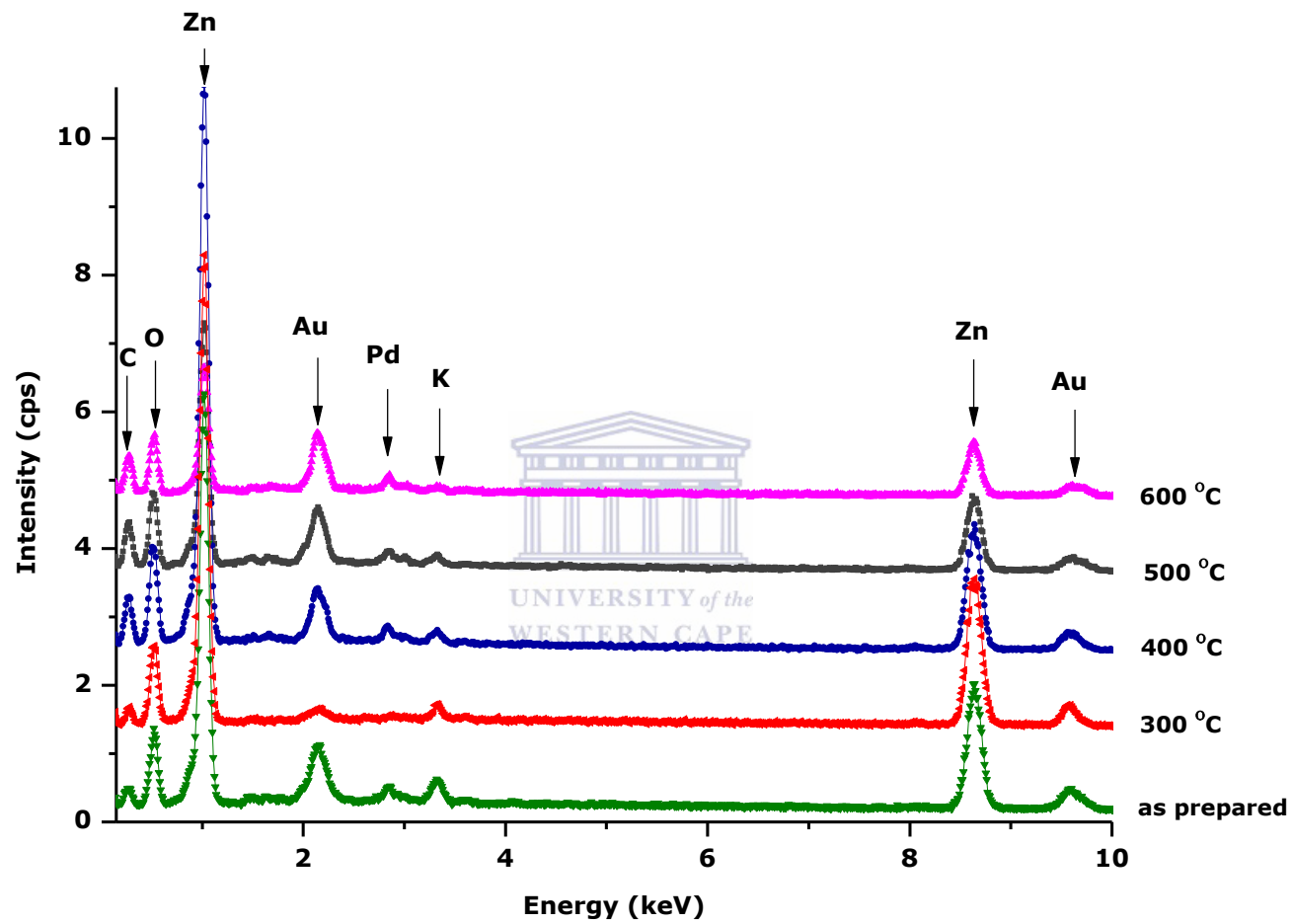


Figure 5.7: EDX spectra of the ZnO nanoparticles at different temperatures.

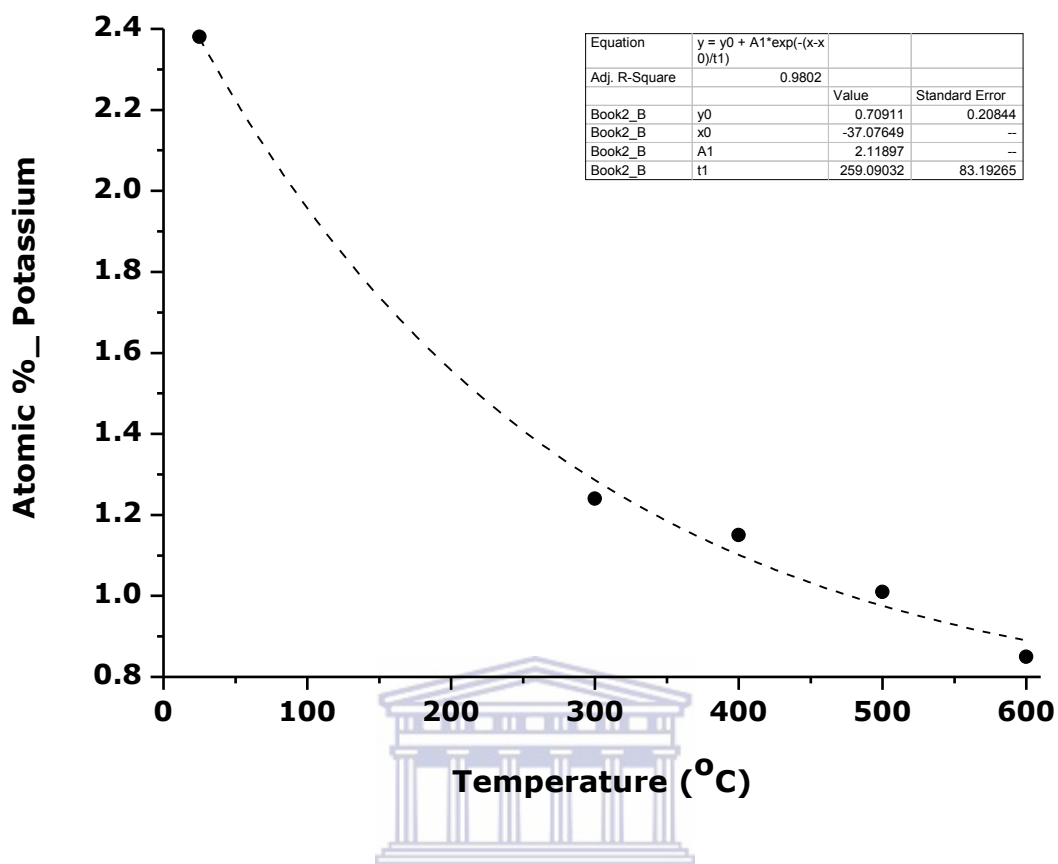


Figure 5.8: Variation of the atomic percent of Potassium (K) versus the annealing temperature. The line is the corresponding simulation curve.

5.3 Transmission Electron Microscopy (TEM)

The TEM image of the as-prepared powder sample is shown in Figure 5.9(a). The image clearly shows the presence of some uniform secondary material which is acting as a capping ligand. This material may be assigned to the organic molecules found in the plant extract [2]. Furthermore, the image shows that the powder consists of quasi-spherical nanoparticles. This is in agreement with the obtained results from SEM. The selected area electron diffraction (SAED) pattern shown in Figure 5.9(b) indicate that the majority of the nanoparticles exhibited a low range atomic ordering and is henceforth amorphous [3]. The TEM and SAED of the powder sample annealed at 300 °C is shown in Figure 5.10. The diffraction rings of the synthesized ZnO nanoparticles are assigned to the (100), (002), (101), (102) and (110) planes, respectively. A similar trend is observed for the sample powder that was annealed at 400 °C, 500 °C and 600 °C which are shown in Figure 5.11, 5.12 and 5.13, respectively.

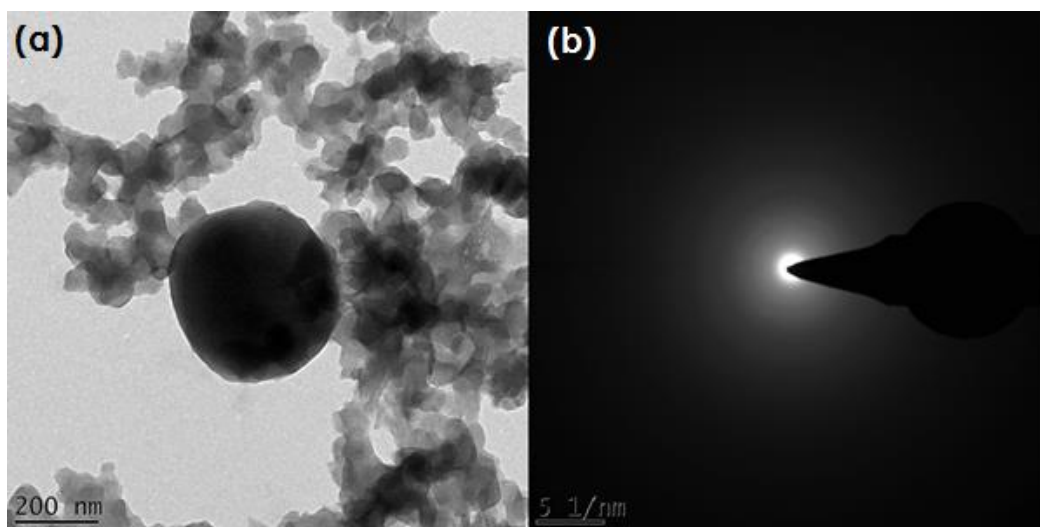


Figure 5.9: (a) TEM and (b) SAED of the as-prepared powder.

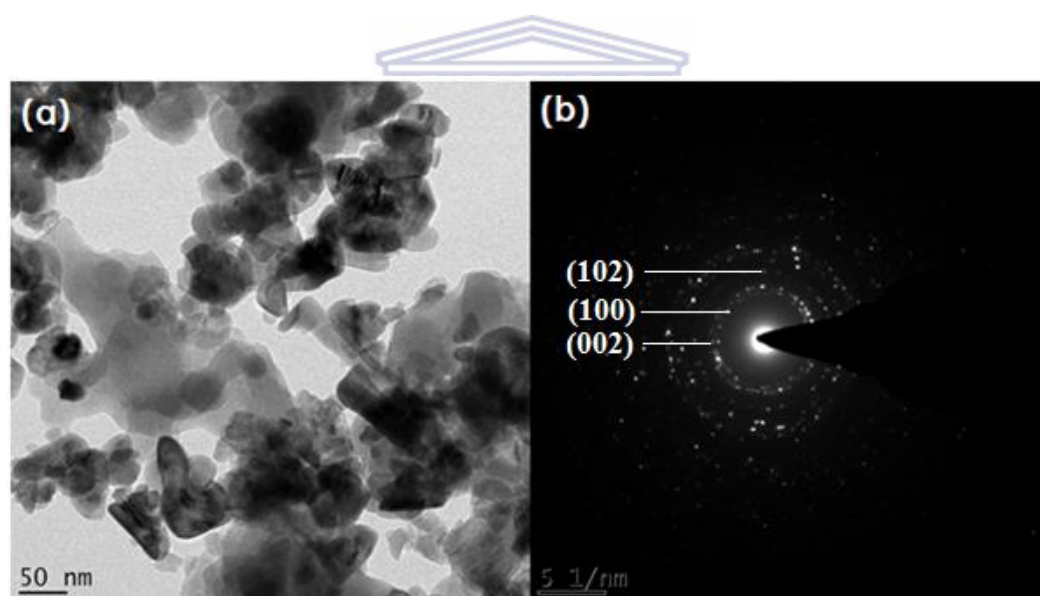


Figure 5.10: (a) TEM and (b) SAED of the powder annealed at 300°C.

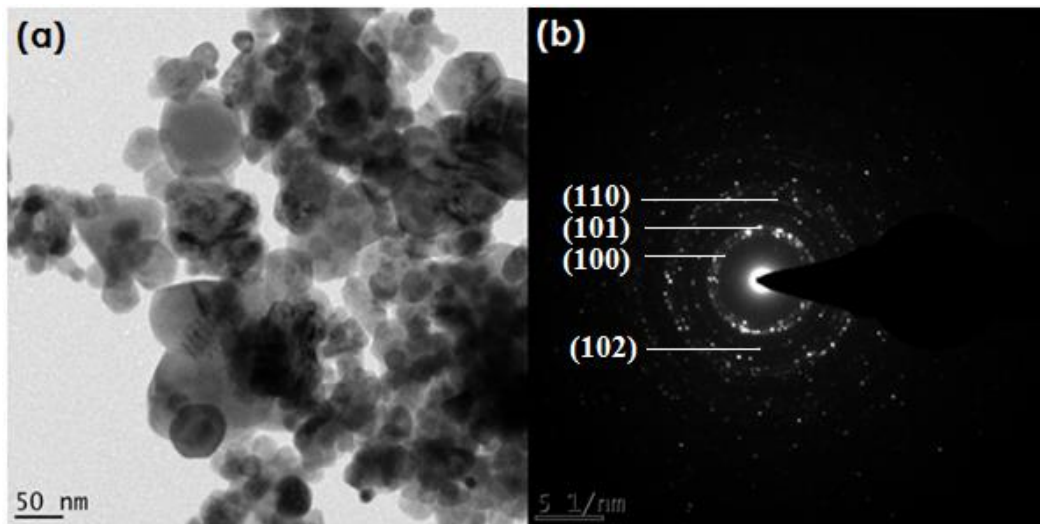


Figure 5.11: (a) TEM and (b) SAED of the powder annealed at 400°C.

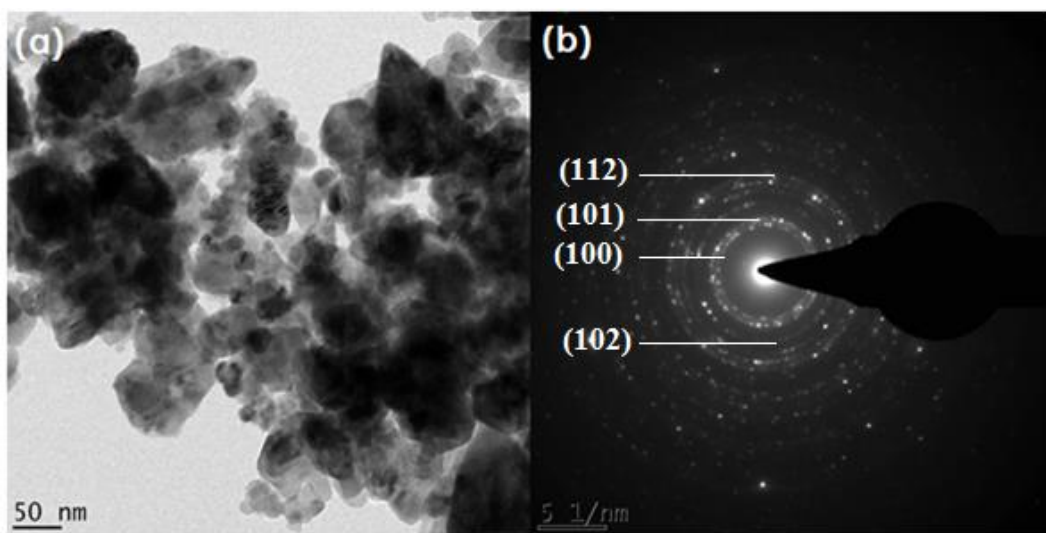


Figure 5.12: (a) TEM and (b) SAED of the powder annealed at 500°C.

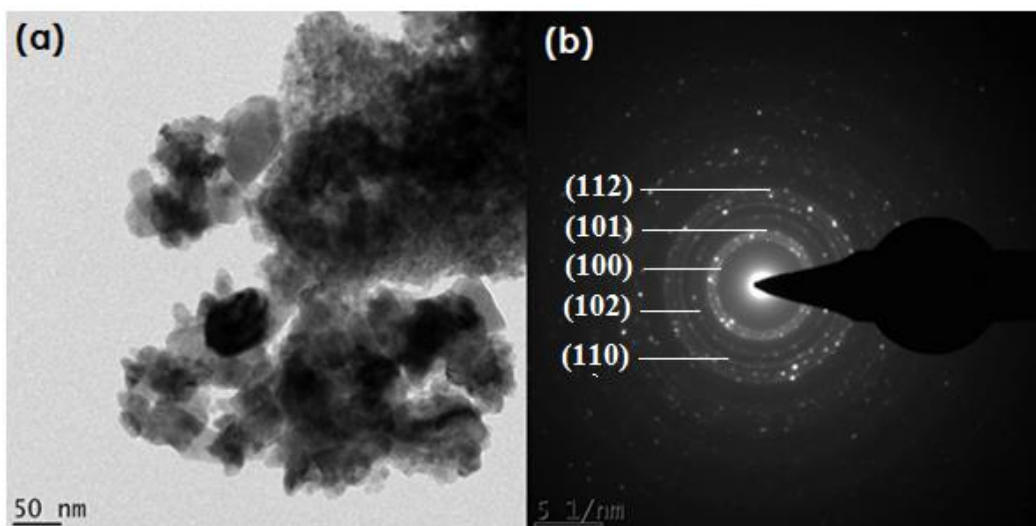


Figure 5.13: (a) TEM and (b) SAED of the powder annealed at 600°C.

5.4 X-ray diffraction (XRD)

The XRD pattern of the as-prepared and annealed powder samples is shown in Figure 5.14. The XRD pattern of the as-prepared sample shows that the crystalline phase of ZnO had not been induced. On the other hand, the annealed powdered samples exhibit a long range order of sharp Bragg peaks. The miller indices for each peak have been indexed to the standard hexagonal wurtzite structure of ZnO. The deduced lattice constants obtained from using equations 4.1 and 4.3 as stated in Section 4.2.3 are recorded in Table 5.2. The deviation of the experimental lattice parameters from the ideal wurtzite crystal is probably due to the presence of various point defects such as the zinc antisites, the oxygen vacancies and threading dislocations [4]. The ZnO nanoparticles annealed from 300 to 600°C displayed similar Bragg peak patterns. The XRD peaks appearing at 2θ of $\sim 31^\circ$, $\sim 34^\circ$, $\sim 36^\circ$, $\sim 47^\circ$, $\sim 56^\circ$, $\sim 62^\circ$, $\sim 66^\circ$, $\sim 67^\circ$, $\sim 69^\circ$ corresponding to the (100), (002), (101), (102), (110), (103), (200), (112) and (201) planes, respectively, are in agreement with the Joint Committee on Powder Diffraction Standard, JCPDS (Card Number 36-1451). The absence of diffraction peaks from other species indicates the complete decomposition of the precursor and thus pure formation of ZnO nanoparticles. This is in agreement with EDS shown in Section 5.2. The experimental d-spacing values of the synthesized nanoparticles are slightly smaller than the theoretical (bulk) values. The full width at half maximum is seen to decrease as the annealing temperature is increased. It is a clear indication that the size and the crystallinity of the ZnO nanoparticles increases with increase in the annealing temperature, confirming the results found in TEM

and SAED. This is also in agreement with other reports found in literature [5, 6]. The average crystallite size of the annealed ZnO nanoparticles was estimated using the Scherrer's equation [7]: $\langle \Phi_{\text{particles}} \rangle = 0.9\lambda / \Delta\theta_{1/2} \cos\theta$, where λ is the X-ray wavelength, $\Delta\theta_{1/2}$ is the full width at half maximum (FWHM), and θ is the diffraction angle. The average crystallite sizes found from this relation are reported on Table 5.2. The average diameters of the ZnO nanoparticles were found to be ~18.2 nm (at 300°C), ~20.6 (at 400°C), ~21.2 (500°C) and ~22.6 nm (at 600°C). The crystallite sizes estimated using the Scherrer equation are in close agreement with those obtained from the SEM results. This confirms that the average size of the ZnO nanoparticles increases with increase in annealing temperature, as previously shown in Figure 5.6.



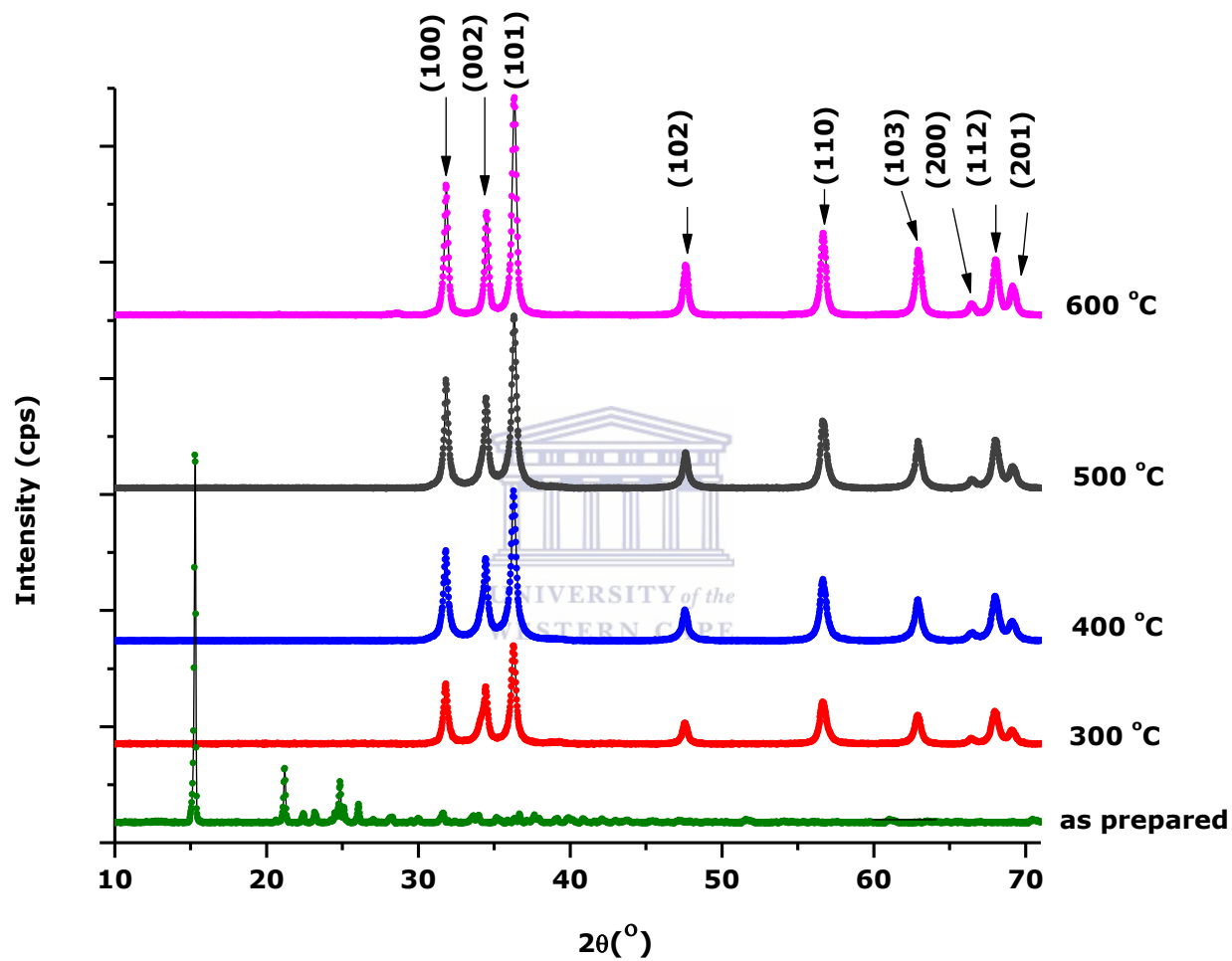


Figure 5.14: X-ray diffraction spectra of ZnO nanoparticles for different temperatures.

Table 5.2: Major parameters of the ZnO nanoparticles derived from the XRD analysis.

(hkl)	$2\theta_{\text{exp}}$ (deg)	$d_{\text{hkl}}^{\text{exp}}$ (Å)	$d_{\text{hkl}}^{\text{bulk}}$ (Å)	$\frac{\Delta dhkl}{d_{\text{hkl}}^{\text{bulk}}}$ (%)	$\Delta\theta_{1/2}$ (degree)	$\langle \Phi_{\text{particles}} \rangle$ (nm)	$\Delta \langle \Phi_{\text{particles}} \rangle$ (nm)	$\langle a_{\text{exp}}(\text{Å}) \rangle$	$\langle c_{\text{exp}}(\text{Å}) \rangle$	$\langle \frac{c}{a} \rangle$
Annealed at 300 °C										
(100)	31.81	2.81	2.814	-0.13	0.40	20.17	17.53	3.2447	5.2102	1.6057
(002)	34.40	2.60	2.603	0.00	0.48	17.89				
(101)	36.27	2.47	2.476	-0.07	0.41	19.82				
(102)	47.58	1.91	1.911	-0.08	0.48	18.68				
(110)	56.68	1.62	1.625	-0.12	0.57	16.37				
(103)	62.91	1.48	1.407	-0.07	0.53	17.80				
(200)	66.46	1.40	1.407	-0.23	0.61	10.90				
(112)	68.01	1.38	1.378	-0.08	0.53	17.42				
(201)	69.12	1.36	1.358	-0.01	0.66	18.69				
Annealed at 400 °C										
(100)	31.81	2.81	2.814	0.07	0.38	22.55	19.44	3.2453	5.2067	1.6043
(002)	34.42	2.61	2.603	-0.06	0.45	16.81				
(101)	36.28	2.47	2.476	-0.07	0.40	20.48				
(102)	47.58	1.91	1.911	-0.12	0.45	20.13				
(110)	56.68	1.62	1.625	-0.06	0.55	16.49				
(103)	62.92	1.48	1.407	-0.11	0.53	18.81				
(200)	66.56	1.41	1.407	-0.06	0.61	22.96				
(112)	68.03	1.38	1.378	-0.02	0.52	19.00				
(201)	69.13	1.36	1.358	-0.21	0.66	17.69				
Annealed at 500 °C										
(100)	31.84	2.81	2.814	-0.16	0.35	26.42				
(002)	34.47	2.60	2.603	-0.15	0.38	23.87				

Table 5.2. - - Continued

(hkl)	$2\theta_{\text{exp}}$ (deg)	$d_{\text{hkl}}^{\text{exp}}$ (Å)	$d_{\text{hkl}}^{\text{bulk}}$ (Å)	$\frac{\Delta dhkl}{d_{\text{hkl}}^{\text{bulk}}}$ (%)	$\Delta\theta_{1/2}$ (degree)	$\langle \Phi_{\text{particles}} \rangle$ (nm)	$\Delta \langle \Phi_{\text{particles}} \rangle$ (nm)	$\langle a_{\text{exp}}(\text{Å}) \rangle$	$\langle c_{\text{exp}}(\text{Å}) \rangle$	$\langle \frac{c}{a} \rangle$
(101)	36.31	2.47	2.476	-0.16	0.39	22.89	21.29	3.2426	5.199	5.1932
(102)	47.62	1.91	1.911	-0.12	0.44	22.18				
(110)	56.70	1.62	1.625	-0.17	0.50	18.44				
(103)	62.95	1.48	1.407	-0.11	0.52	19.50				
(200)	66.51	1.40	1.407	-0.06	0.61	21.66				
(112)	68.05	1.38	1.378	-0.20	0.51	20.82				
(201)	69.15	1.36	1.358	-0.23	0.63	15.82				
Annealed at 600 °C										
(100)	31.83	2.81	2.814	-0.17	0.31	25.60	22.62	3.2433	5.1932	1.6012
(002)	34.50	2.60	2.603	-0.12	0.29	26.54				
(101)	36.32	2.47	2.476	-0.14	0.33	24.45				
(102)	47.63	1.91	1.911	-0.13	0.39	21.03				
(110)	56.68	1.62	1.625	-0.11	0.42	20.96				
(103)	62.96	1.48	1.407	-0.08	0.48	19.60				
(200)	66.48	1.41	1.407	-0.13	0.42	24.34				
(112)	68.05	1.38	1.378	0.00	0.46	20.64				
(201)	69.17	1.36	1.358	-0.07	0.52	20.42				

5.5 Differential Scanning Calorimetry and Thermogravimetric Analysis (DSC-TGA)

The thermogram of the as-prepared sample is shown in Figure 5.15. The first thermal event is observed between 56 and 173°C with a ~8.51 % weight loss. This weight loss was due to the removal of the chemically adsorbed water. The main weight loss of ~49.3 % was observed starting from 195 - 435 °C. This second weight loss is attributed to the decomposition of the organic species. The two endothermic peaks found at 88 °C and 230 °C are attributed to evaporation of the adsorbed water and decomposition of residual organic molecules, respectively. The exothermic peak observed at ~341°C is due to the decomposition of ZnAc into stable ZnO nanoparticles. Beyond this temperature, no further weight loss is observed. This implies that the ZnO nanoparticles become stable above this temperature. The enthalpy of change was obtained through the integration of the area under the peak and is recorded on Table 5.3.

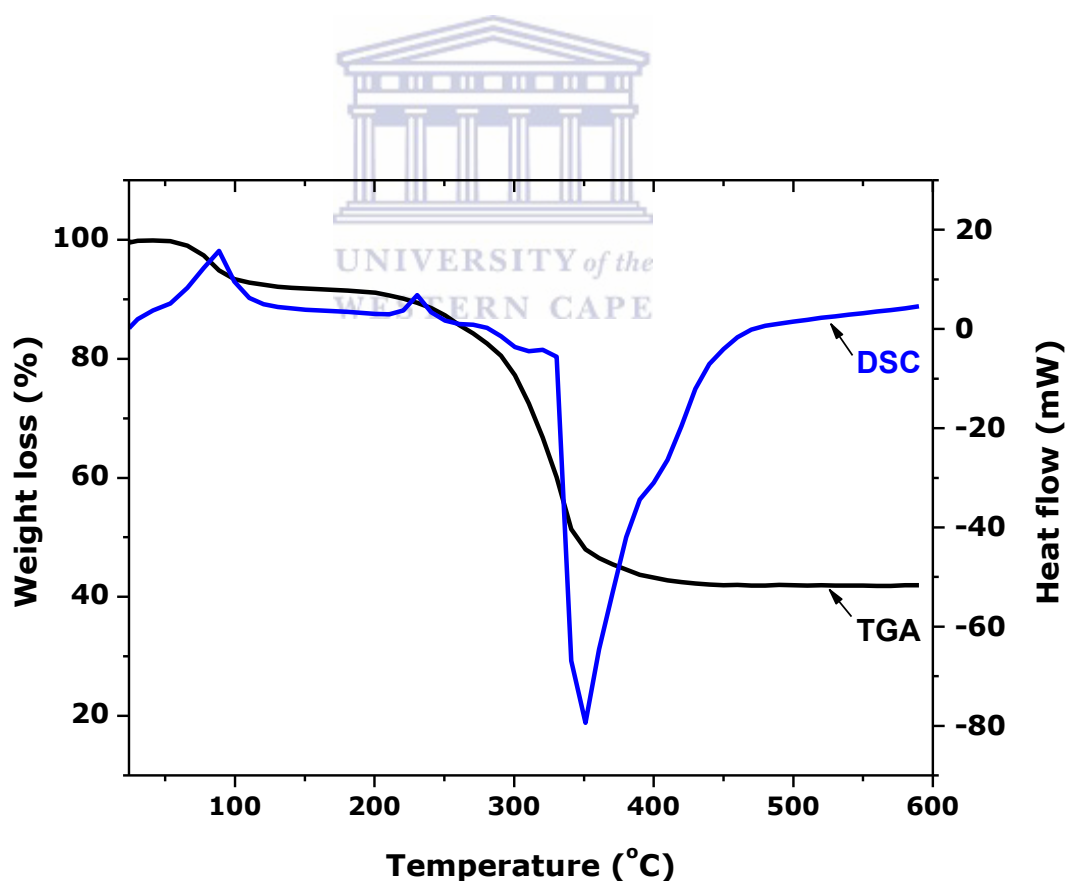


Figure 5.15: TGA-DSC plot of the as-prepared powder sample

Figure 5.16 shows the thermogram of the powder that was annealed at 300 °C. TGA shows a slight gradual weight loss of ~5.56 % probably due to the loss of the moisture in the instrumentation [8]. A similar trend is also observed for the powders annealed at 400, 500 and 600 °C, which are shown in Figures 5.17, 5.18 and 5.19, respectively. By differentiating heat flow curve in Figure 5.16, 5.17, 5.18 and 5.19, the decomposition temperature of ZnAc into stable, crystalline ZnO nanoparticles was found to occur at 498 °C, 362 °C, 214 °C and 161 °C, respectively.

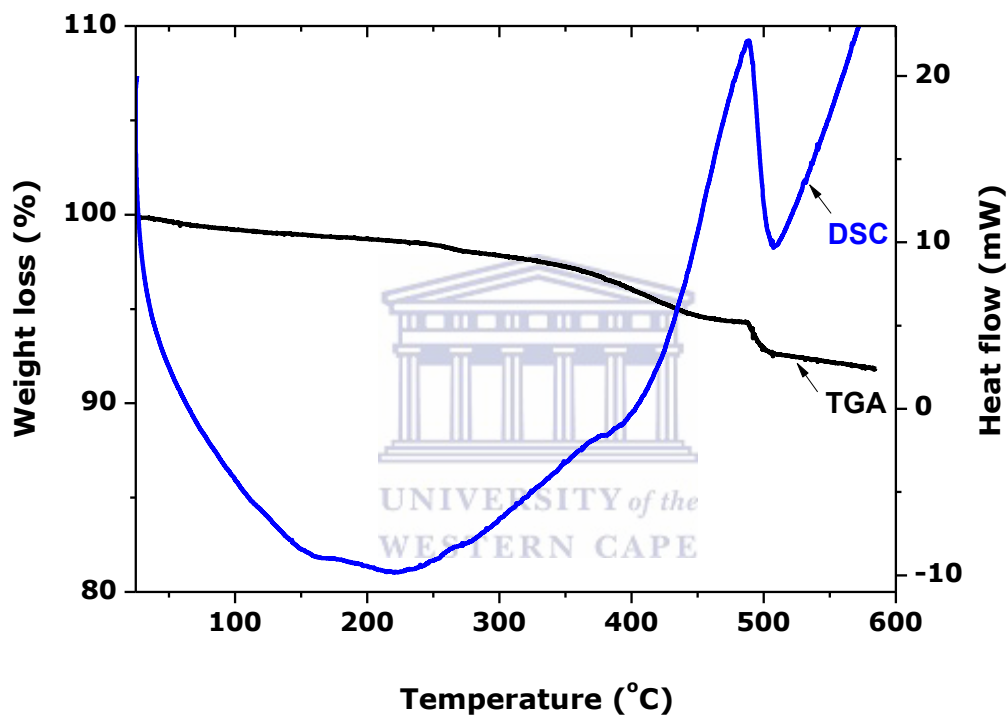


Figure 5.16: TGA/DSC plot of the ZnO nanoparticles annealed at 300 °C.

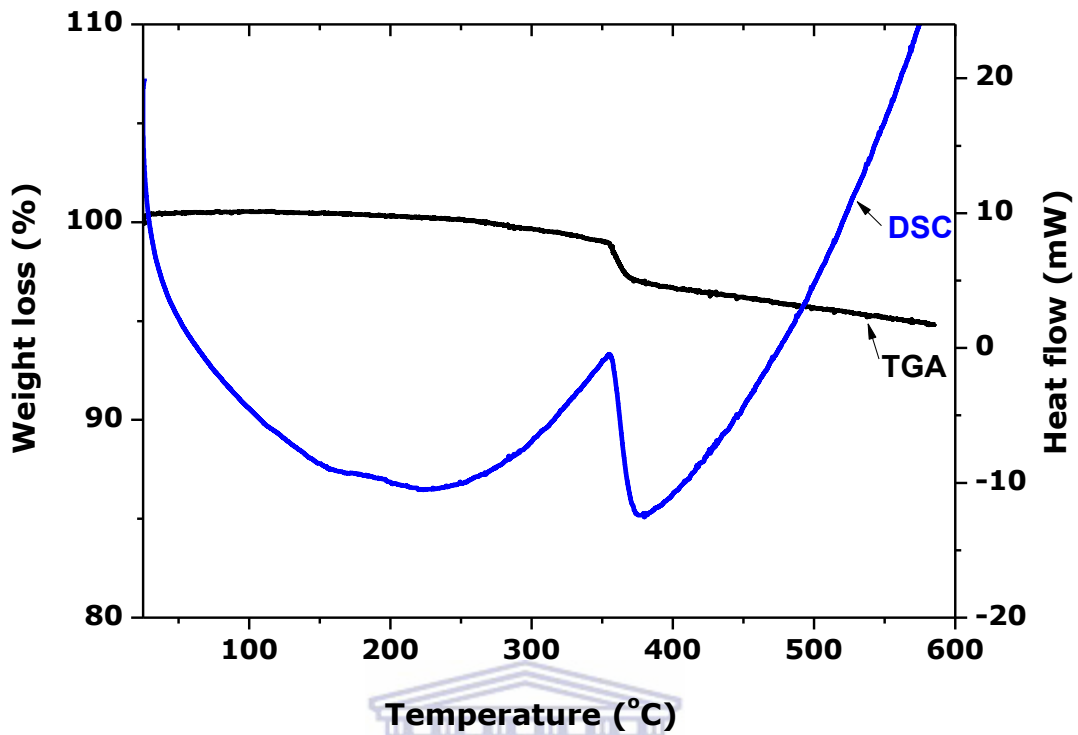


Figure 5.17: TGA/DSC of the ZnO nanoparticles annealed at 400 °C.

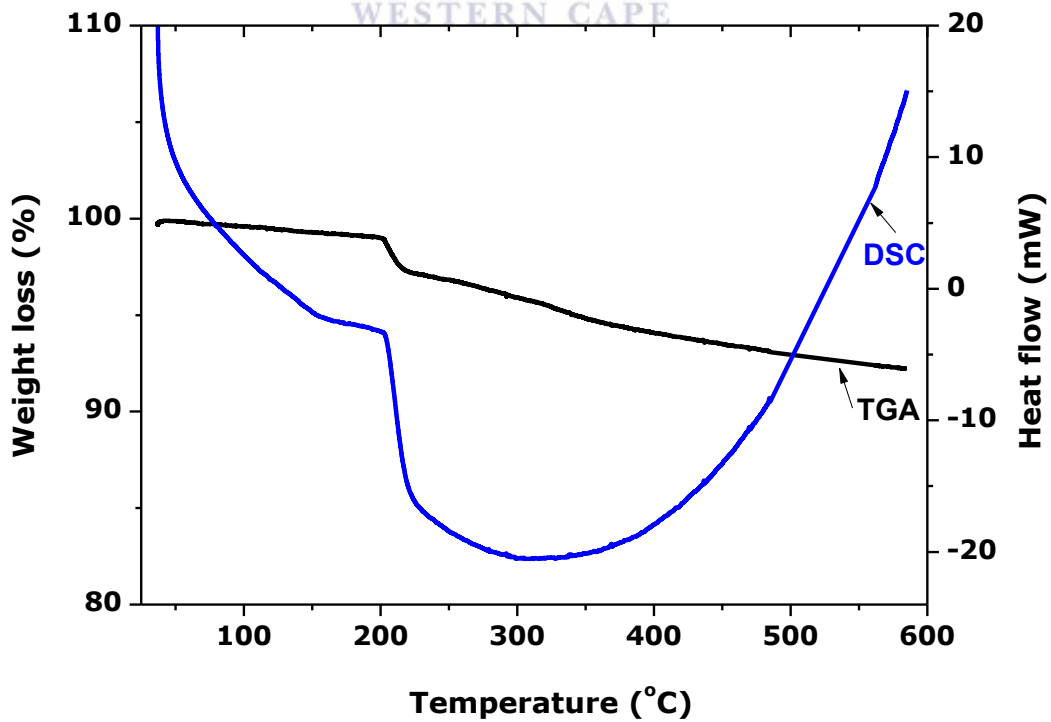


Figure 5.18: TGA/DSC plot of the ZnO nanoparticles annealed at 500 °C.

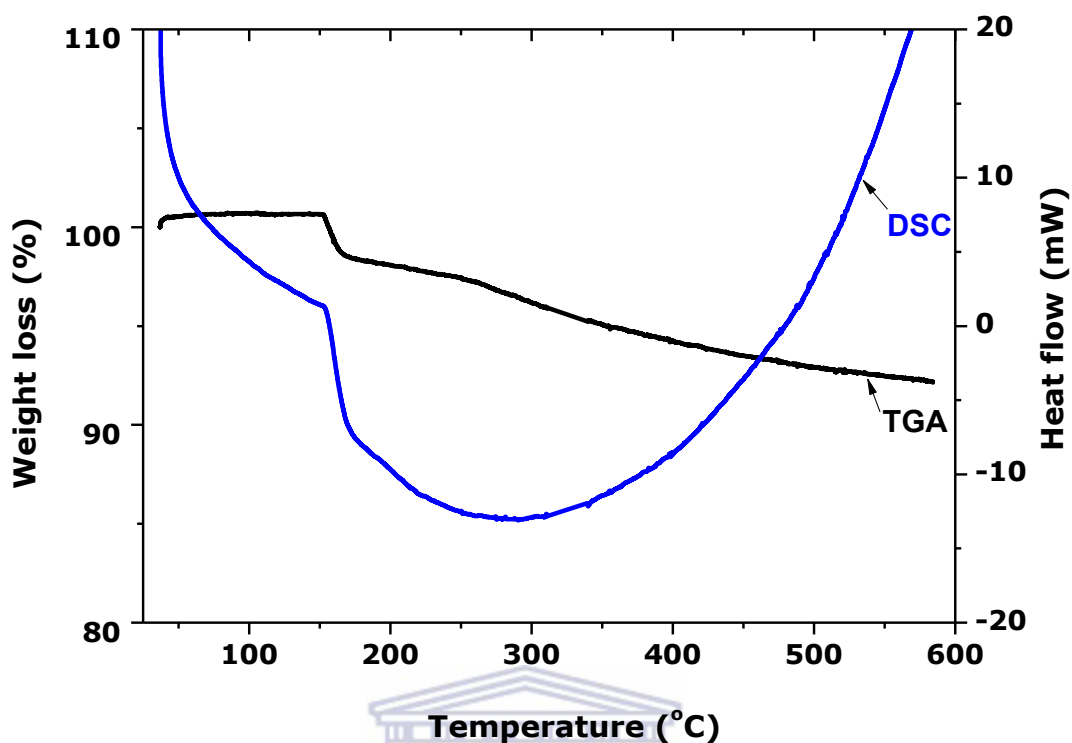
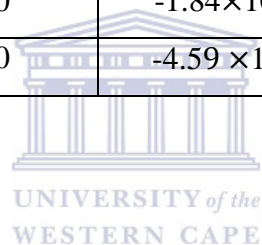


Figure 5.19: TGA/DSC of the ZnO nanoparticles annealed at 600 °C.

Since this powder was confirmed to be crystalline before the beginning of the TGA/DSC measurements, no thermal transitions are observed prior to the one observed at ~488 °C. As the temperature increases, the peaks tend to become broader, generate large heat flow (as depicted in Table 5.3) and shift to lower temperature values. This shows that as the nanoparticles are annealed at higher temperatures, they become more crystalline, as shown by the XRD and TEM measurements. In SEM, this is confirmed by the change in the morphology and structure of the ZnO nanoparticles when the rod-like structures changed into a quasi-spherical morphology.

Table 5.3: Enthalpy change calculated for the ZnO powdered samples.

Sample type	Peak type	Temperature (°C)	Area (mJ)	Initial mass (mg)	Enthalpy (J/g)
As-prepared	Endothermic	51 – 115	58.01	4.400	13.18
	Endothermic	271 – 255	17.60		4.00
	Exothermic	321 – 449	-458.74		-104.25
Annealed @ 300 °C	Exothermic	489 – 600	-478.93	4.480	-106.90
Annealed @ 400 °C	Exothermic	356 – 600	-1.61×10^3	4.192	-386.33
Annealed @ 500 °C	Exothermic	199 – 600	-1.84×10^3	4.781	-386.21
Annealed @ 600 °C	Exothermic	157 – 600	-4.59×10^3	4.744	-967.64



5.6 Fourier Transform Infrared (FTIR)

The FTIR spectra of the powder samples are displayed in Figure 5.20. A series of absorption peaks in the range from 4000 – 400 cm^{-1} have been found. The broad absorption peak at 3673 cm^{-1} is attributed to the O-H stretching vibration. The weak peak observed at 3459 cm^{-1} corresponds to the O-H stretching vibration of the intramolecular hydrogen bond. As the temperature was increased, the intensity of the peaks attributed to the O-H bond decreased. This might be due to the removal of certain organic material. The peaks observed at 1578 and 1565 cm^{-1} are doublets and they correspond to the zinc carboxylate C=O symmetric stretching vibration. They are still observed at higher temperatures. At the annealing temperature of 400 °C, the doublets merge into a broad peak which is observed at 1501 cm^{-1} . The broadening and shifting to lower wavenumber is caused by the stress acting on the ZnO nanoparticles and the variation in the morphology of the nanoparticles. Annealing at 600 °C significantly reduces the peak, indicating that the organic material is completely removed at this temperature. It is clear that this specific peak is not eliminated at this temperature. The peak centred at 1068 cm^{-1} is attributed to the C-O bond stretching. The increase in temperature deteriorates this peak and at the annealing temperature of 600 °C it almost disappears. The sharp peak at ~493 cm^{-1} is attributed to the Zn-O stretching mode. This findings are supported by some previous reports [2,9].

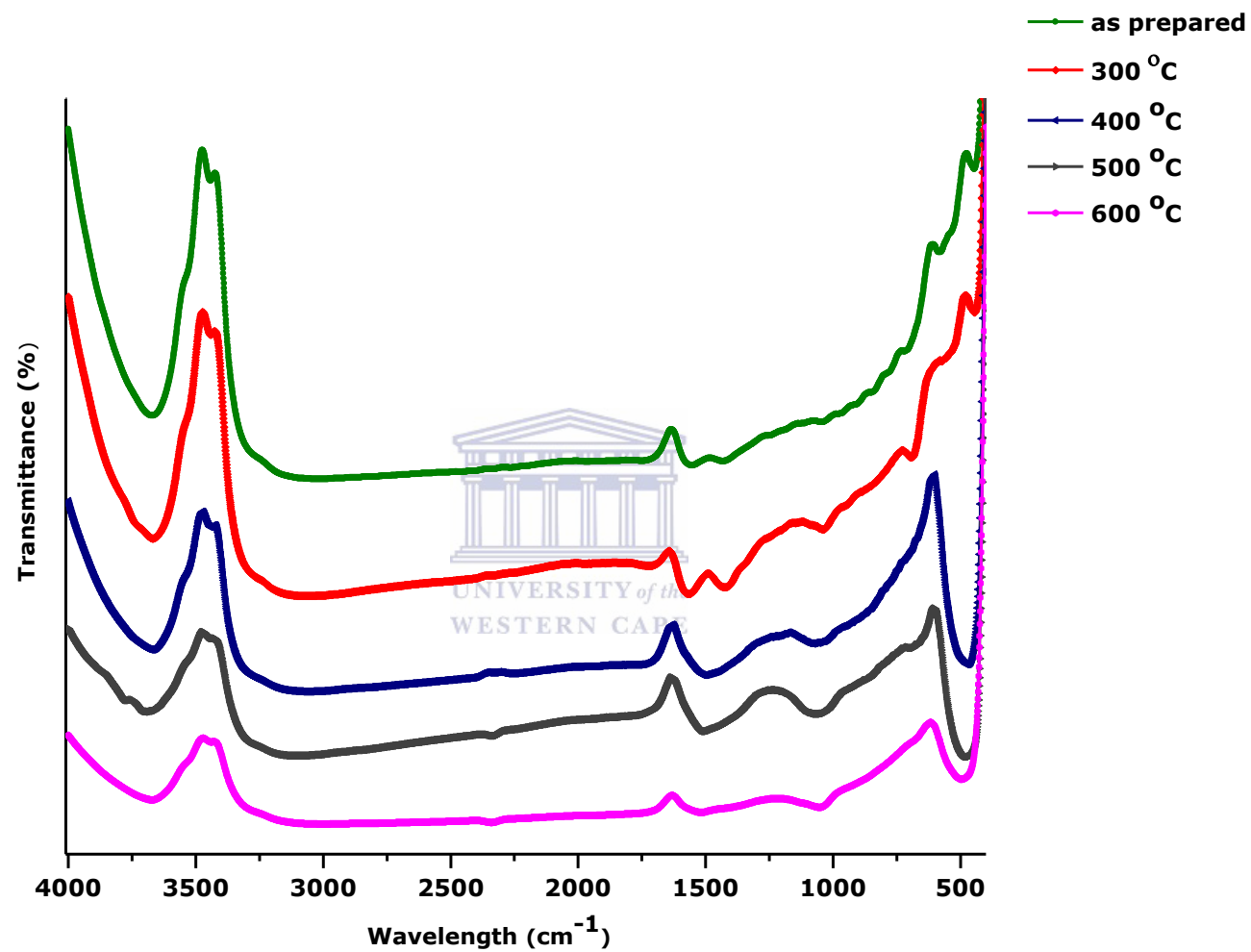


Figure 5.20: FTIR spectra of ZnO nanoparticles.

Summary

The SEM measurements revealed that most of the nanoparticles are quasi-spherical grains agglomerated together. The nanoparticles' quasi spherical morphology was observed in both the as-prepared and annealed samples. This morphology of the nanoparticles was in agreement with the images obtained from TEM. Furthermore, TEM also showed that the nanoparticles are amalgamated by some sort of a capping agent assigned to the organic molecules found in the plant extract. Following the digitization on the SEM images by using the Image J software, the average particle sizes of the powdered sample that was annealed at 300 °C, 400 °C, 500 °C and 600 °C was found to be 24.6 nm, 27.2 nm, 27.6 nm and 28.5 nm, respectively. EDX showed the presence of Zn and O elements within the powders whilst FTIR confirmed the existence of the Zn-O vibrational bonds in all the sample nano-powders. Both EDX and FTIR both confirm the presence of only Zn and O elements. The XRD measurements showed that the as-prepared sample was amorphous whereas those that underwent the annealing process exhibited highly crystalline phases. This observation is in agreement with the SAED images obtained during the TEM measurements. From the Scherrer calculations, it was found out that the average particle sizes of the ZnO nanoparticles annealed at 300 °C, 400 °C, 500 °C and 600 °C are 18.2 nm, 20.6 nm 21.2 nm and 22.6 nm, respectively. Although the values of the particle size deduced from SEM appear to be slightly greater than the ones obtained from the Scherrer approximation, they are still in close agreement. Lastly, the DSC/TGA measurements revealed that the decomposition temperature of ZnAc into stable ZnO nanoparticles occurs at 341 °C, 498 °C, 362 °C, 214 °C and 161 °C for the as-prepared powder and the powders annealed at 300 °C, 400 °C, 500 °C and 600 °C, respectively. It was observed that the effect of the annealing temperature on the samples was to induce and improve the crystallinity of that sample. And hence, the particle size of the nanoparticles increased as a result. The DSC measurements are in agreement with the XRD measurements.

5.7 References

- [1] V. Makarov, A. Love, O. Sinitsyna, S. Makarova, I. Yaminsky, M. Taliansky and N. Kalinina, "Green Nanotechnologies: Synthesis of Metal Nanoparticles Using Plants," *Acta Naturae*, vol. 6, no. 1, pp. 35-44, 2014.
- [2] G. Sangeetha, S. Rajeshwari and R. Venckatesh, "Green synthesis of zinc oxide nanoparticles by aloe barbadensis miller leaf extract: structure and optical properties," *Materials Research Bulletin*, vol. 46, no. 12, pp. 2560-2566, 2011.
- [3] N. Shibata, G. Painter, P. Becher and S. Pennycook, "Atomic ordering at an amorphous/crystal interface," *Applied Physics Letters*, vol. 89, no. 1, pp. 89-91, 2006.
- [4] H. Markoq and U. Ozgur, *Zinc Oxide: Fundamentals, Materials and Device Technology*, Virginia: Wiley-VCH, 2009.
- [5] S. Azizi, R. Mohamad, A. Bahadoran, S. Bayat, R. Rahim, A. Ariff and W. Saad, "Effect of annealing temperature on antimicrobial and structural properties of bio-synthesized zinc oxide nanoparticles using flower extract of *Anchusa italica*," *Journal of Photochemistry and Photobiology*, vol. 161, no. 1, pp. 441-449, 2016.
- [6] S. Ghosh, "Synthesis and characterization of ZnO nanoparticles by sol-gel process," National Institute of Technology, Rourkela, 2012.
- [7] "Scherrer equation," [Online]. Available: https://en.wikipedia.org/wiki/Scherrer_equation. [Accessed 15 February 2017].
- [8] L. Thomas, "Interpreting unexpected events and transitions in DSC results," *TA Instruments*, vol. 1, no. 1, pp. 1-5, 2015.
- [9] S. Raut, P. Thorat and R. Thakre, "Green synthesis of Zinc Oxide (ZnO) nanoparticles using *Ocimum Tenuiflorum*," *International Journal of Science and Research*, vol. 4, no. 5, pp. 1225-1228, 2013.

Chapter 6: Conclusions and recommendations

6.1 Conclusion

The aim of this work was to construct a literature review on the properties of nano-sized ZnO obtained by using the green chemistry synthesis approach. The main objective of the study was to synthesize ZnO nanoparticles by this method, using *Aspalathus Linearis*' natural extract as an effective reducing agent. The effect of the annealing temperature on the physical properties of the synthesized ZnO nanoparticles were investigated using SEM, EDS, TEM, XRD, DSC, TGA and FTIR characterizing techniques.

High quality ZnO nanoparticles were successfully obtained by an entirely green chemistry process using the natural extract of *Aspalathus Linearis* as an effective reducing agent with $\text{Zn}(\text{C}_4\text{H}_6\text{O}_4) \cdot 2\text{H}_2\text{O}$ precursor. The obtained ZnO nanopowdered sample was annealed at different annealing temperature of 300 °C, 400 °C, 500 °C and 600 °C for a period of 2 hours under air. The effect of the annealing temperature on the physical properties (morphology, structure and composition quality) of the ZnO nanoparticles was obtained by characterizing the ZnO powder samples using SEM, EDS, TEM, XRD, DSC, TGA and FTIR.

Both the SEM and TEM measurements showed that the ZnO nanoparticles were quasi-spherical with an average size of 24.6 nm, 27.2 nm, 27.6 nm and 28.5 nm at annealing temperatures of 300 °C, 400 °C, 500 °C and 600 °C, respectively. From this it is observed that the average particle sizes of the ZnO nanoparticles increased as the annealing temperature was increased. EDS and FTIR confirmed that the powder samples were pure ZnO nanoparticles without any defects or impurities. In fact, as the annealing temperature was increased, the ZnO nanoparticles adapt an even higher state of purity. XRD measurements revealed that the ZnO nanoparticles were crystalline with a wurtzite hexagonal structure, confirming what was found in the literature review. From the Scherrer approximation, the average particle size of the nanoparticles was calculated to be 18.2 nm, 20.6 nm, 21.2 nm and 22.6 nm, at temperature of 300 °C, 400 °C, 500 °C and 600 °C, respectively, which are in close agreement with the average particle size estimated from SEM. The DSC/TGA thermogram of the as-prepared sample revealed that the decomposition of ZnAc into stable ZnO nanoparticles takes place at 341 °C. The samples that were annealed at 300 °C, 400 °C, 500 °C and 600 °C, decomposed into stable ZnO at temperatures of 498 °C, 362 °C, 214 °C and 161 °C, respectively. Moreover, as the annealing temperature was increased, the peaks

tend to become broader and shift to lower temperature values. This behaviour showed that as the ZnO nanoparticles are annealed at higher temperatures, their crystallinity improves significantly, which is in agreement with the XRD measurements. All the results were in full agreement with what was discussed in the literature review.

6.2 Future work and recommendations

The properties ZnO nanoparticles displayed make them a promising material for pharmaceutical, medicinal and optoelectronic applications. Hence, the future work is to test the antimicrobial activity of the ZnO nanoparticles against bacteria and fungi, with an aim of using them as water purifiers for waterborne bacteria found in most of our untreated drinking water. Further work on its potential as a solar absorber could also be studied.

